


# Structural fatigue assessment and optimisation of offshore wind turbine jacket foundations

Thesis for the Degree of Engineering Doctorate in Renewable Energy Marine Structures (REMS)

By

**Ali Marjan**

Supervisor: Dr Luofeng Huang
Associate Supervisor: Dr Phil Hart
August 2023

School of Water Energy and Environment

© Cranfield University 2023. All rights reserved. No part of this publication may be reproduced without the written permission of the copyright owner.

# ABSTRACT

Offshore Wind Turbine (OWT) is an expensive type of renewable energy system, and there is a continuous effort to lower the capital and operational costs. Jacket foundations are increasingly used in offshore wind due to their relatively light weight and adaptability in deep waters. However, the contemporary jacket designs are based on conservative practices from the oil and gas industry. There is still substantial room to optimise the jacket designs for offshore wind usage. This research aims to generate innovative jacket designs by applying a topology optimisation algorithm. The research demonstrates the use of advanced computational techniques to improve existing designs by enhancing structural integrity and fatigue life whilst reducing the mass.

The research presents a comprehensive investigation of different parameters and design modifications that impact the design life of an existing jacket. An OC4 jacket foundation is employed, modelled in industrial software from DNV, and transformed into a superelement model. The time-series loads obtained from Bladed are used to assess fatigue damages experienced during the foundation's service life.

Furthermore, the research presents a topology optimisation method to retrofit an existing jacket foundation design by finding the optimum load path on the structure to enhance fatigue life and lower costs. The jacket's structural optimisation is performed by considering its dynamic response while adhering to the relevant international design standards. In particular, time-domain fatigue simulations were performed to assess the structural integrity of the topology-optimised jacket for the first time. As a result, a range of optimised models with various thickness and diameter options are presented, which are shown to be rational and verify the optimisation procedure. The research contributes a unique integrated topology optimisation framework, dynamic analysis, and time-domain fatigue simulations using industry-standard software tools, and achieved a mass reduction of 35.2% and simultaneously realized a 37.2% better fatigue life compared to the baseline model. The overall environmental load calculation, optimisation procedure and results provide useful practicalities for designing

offshore wind turbine foundations and potentially facilitate the relevant industry's structural integrity and cost reduction.

**Keywords:**

Offshore wind turbine, Jacket foundations, Environmental loads, Dynamic response, Topology optimisation, Mass reduction, Fatigue

# ACKNOWLEDGEMENTS

I would like to express my heartfelt gratitude to my supervisors, Dr. Luofeng Huang and Professor Phil Hart. Their extensive expertise, supervision and constant encouragement have been invaluable throughout my research. They have pushed me to think more critically and inspired me to grow into an independent researcher.

I consider myself extremely fortunate to have been part of the Centre for Doctoral Training (CDT) in Renewable Energy Marine Structures (REMS). The environment with people from different backgrounds provided the perfect setting to improve my skills. I appreciate everyone who helped make the CDT a supportive yet challenging place for research. In particular, I would like to thank the Centre Director, Professor Feargal Brennan, and the REMS Manager, Dr. Ali Mehmanparast, for giving me the opportunity to be part of REMS and supporting my research. I would also like to thank my colleague Dr. Kuen-Wei Wu for his encouragement and support.

I could not have made it through this journey without the love and support of my family and friends. I am incredibly grateful to my wonderful wife and children, who were understanding during this long journey and gave me strength when I needed it most. Most importantly, I am forever thankful to my parents for their support not just when I was pursuing my EngD but also for the rest of my life. Their unconditional love and guidance have shaped the person I am today. I also want to acknowledge the Chief Minister Merit Scholarship for generously funding my doctorate degree and making this achievement possible.

# LIST OF PUBLICATIONS

## Journal articles as part of this work

Marjan A, Shafiee M. Evaluation of Wind Resources and the Effect of Market Price Components on Wind-Farm Income: A Case Study of Ørland in Norway. Energies. 2018; 11(11):2955

Marjan A, Hart P. Impact of Design Parameters on the Dynamic Response and Fatigue of Offshore Jacket Foundations. Journal of Marine Science and Engineering. 2022; 10(9):1320.

Marjan A, Huang L. Topology optimisation of offshore wind turbine jacket foundation for fatigue life and mass reduction: Ocean Engineering (Accepted).

# ACADEMIC INTEGRITY DECLARATION

I declare that:

- The thesis submitted has been written by me alone.
- That all content, including primary and/or secondary data, is true to the best of my knowledge.
- That all quotations and references have been duly acknowledged according to the requirements of academic research.

# TABLE OF CONTENTS

ABSTRACT ..... i
ACKNOWLEDGEMENTS ..... iii
LIST OF PUBLICATIONS ..... iv
ACADEMIC INTEGRITY DECLARATION ..... v
LIST OF FIGURES ..... ix
LIST OF TABLES ..... xii
NOMENCLATURE ..... xiii
1 Introduction ..... 1
1.1 Problem definition ..... 2
1.2 Research gap ..... 3
1.3 Aim and objectives ..... 3
1.4 Structure of the thesis ..... 4
2 Literature Review ..... 6
2.1 Offshore wind energy ..... 6
2.1.1 Global growth trends ..... 6
2.1.2 Drivers and challenges ..... 7
2.1.3 Support structure innovation needs ..... 8
2.2 Offshore wind turbine support structures ..... 9
2.2.1 Monopile ..... 10
2.2.2 Jacket ..... 10
2.2.3 Tripod ..... 10
2.2.4 Gravity based foundations ..... 10
2.2.5 Floating foundations ..... 11
2.3 Sources of loads ..... 11
2.3.1 Inertia ..... 12
2.3.2 Wind ..... 12
2.3.3 Wave ..... 13
2.4 Design standards and code of practices ..... 22
2.4.1 Design codes ..... 23
2.4.2 Design load cases ..... 24
2.5 Fatigue design methodologies ..... 25
2.5.1 S-N curve method ..... 27
2.5.2 Linear Elastic Fracture Mechanics Method ..... 29
2.6 Finite element analysis methods ..... 32
2.6.1 Standard analysis method (p-y method) ..... 32
2.6.2 3D design method ..... 33
2.6.3 Beam element model ..... 33
2.7 Structure optimisation ..... 34
2.7.1 Structural optimisation of the offshore foundations ..... 36
2.7.2 Topology optimisation algorithm ..... 37

3 Evaluation of Wind Resources and Windfarm Income ..... 40
3.1 Introduction ..... 42
3.2 Site description ..... 42
3.3 Wind resource analysis ..... 45
3.3.1 Theory ..... 45
3.3.2 Results ..... 46
3.4 Power performance ..... 57
3.4.1 Theory ..... 57
3.4.2 Methodology ..... 57
3.4.3 Results ..... 58
3.5 Revenue estimation ..... 61
3.6 Conclusions ..... 66
4 Dynamic Response and Fatigue of Offshore Jacket Foundation ..... 68
4.1 Introduction ..... 69
4.1.1 Reference model ..... 69
4.1.2 Site specifications ..... 69
4.1.3 Wind turbine model ..... 70
4.2 FEA model ..... 71
4.2.1 Jacket support structure model ..... 72
4.2.2 Grouted connection ..... 73
4.2.3 Transition piece ..... 74
4.2.4 Soil-structure interaction modelling ..... 75
4.3 Model validation ..... 76
4.3.1 Modal analysis ..... 76
4.3.2 Static analysis ..... 78
4.4 Fatigue limit state (FLS) analysis ..... 79
4.4.1 Methodological approach for FLS ..... 79
4.5 Results and discussion ..... 88
4.5.1 Soil ..... 89
4.5.2 Marine growth ..... 90
4.5.3 Transition piece ..... 91
4.5.4 Scour ..... 93
4.5.5 Grouted connection ..... 94
4.6 Conclusions ..... 97
5 Fatigue Design of Offshore Jacket Foundation: Topology Optimisation Approach ..... 100
5.1.1 Topology optimisation workflow ..... 101
5.2 Methodology ..... 104
5.2.1 Base model ..... 105
5.2.2 Load calculation ..... 106
5.2.3 Topology optimisation process ..... 109
5.2.4 Superelement convergence ..... 113

5.2.5 Fatigue damage calculation ..... 117
5.3 Results and discussion ..... 120
5.3.1 Parametric models ..... 120
5.3.2 Dynamic behaviour ..... 122
5.3.3 Fatigue damages ..... 124
5.4 Conclusions ..... 129
6 Concluding remarks ..... 130
REFERENCES ..... 136
Appendix A Electricity prices and TGC prices ..... 153
Appendix B S-N curves ..... 154

# LIST OF FIGURES

Figure 1-1: Interconnection of chapters ..... 5

Figure 2-1: Growth in size of wind turbines (Adapted from [19]) ..... 7

Figure 2-2: Types of offshore wind foundations (Adapted from [25]) ..... 9

Figure 2-3: Sources of loads on jacket foundation (Adapted from [34]) ..... 12

Figure 2-4: Selection of wave theory (Adapted from [43]) ..... 17

Figure 2-5: Comparison of JONSWAP and Pierson-Moskowitz spectrum for Hs = 5m and Tz = 8s (Adapted from [41]) ..... 19

Figure 2-6: Scatter diagram normalized in parts per 1000 (Adapted from [47]) 21

Figure 2-7: S-N curve for steel in the air [31] ..... 27

Figure 2-8: Fracture modes (Adapted from [72]) ..... 30

Figure 2-9: Relation between crack propagation rate and stress intensity factor (Adapted from [74] ) ..... 32

Figure 3-1: Wind farm's location ..... 43

Figure 3-2: Wind farm's view ..... 44

Figure 3-3: Location of LIDAR and middle wind turbine ..... 45

Figure 3-4: Hub-height wind speed frequency for 12 months. ..... 47

Figure 3-5: Frequency wind rose of 12 months ..... 48

Figure 3-6: Wind rose with the method of bins ..... 48

Figure 3-7: Mean monthly wind speed ..... 49

Figure 3-8: Mean of monthly means of WPD vs. height ..... 51

Figure 3-9: Correlation between the target and reference wind speeds ..... 54

Figure 3-10: Comparison of the wind farm's monthly mean wind speeds and the long-term predicted wind speeds ..... 54

Figure 3-11: Long-term predicted wind direction ..... 56

Figure 3-12: Multi-annual predicted wind speed of the wind farm: (a) Annual mean wind speed of 38 years; (b) Histogram of annual means ..... 56

Figure 3-13: The monthly mean power output of the wind farm ..... 58

Figure 3-14: The monthly capacity factor of the wind farm ..... 59

Figure 3-15: Power curve with the scatter plot ..... 60

Figure 3-16: Monthly income stream of the wind farm ..... 62
Figure 3-17: Actual and simulated income of the wind farm ..... 64
Figure 3-18: Changes in mean output with respect to electricity price and TGC price for January ..... 65
Figure 3-19: Contribution of electricity price and TGC price to variance of income for January ..... 65
Figure 4-1: Genie model of the jacket foundation ..... 73
Figure 4-2: A grouted connection between pile and leg ..... 74
Figure 4-3: Complete 3D model of the jacket and soil profile ..... 76
Figure 4-4: Power density of NREL 5MW wind turbine [Adapted from [26]] ..... 77
Figure 4-5: Deflection with the fixed base ..... 78
Figure 4-6: Flowchart of software modules ..... 81
Figure 4-7: Superelement method [142] ..... 82
Figure 4-8: Comparison of nodal displacements for spatial convergence ..... 84
Figure 4-9: Error in blade's pitch angle with built-in controller ..... 86
Figure 4-10: Uniform blade pitch angle with designed controller ..... 86
Figure 4-11: Hotspot of K-joint [55] ..... 88
Figure 4-12: Location of the worst-performing joint ..... 89
Figure 4-13: Dynamic response with and without soil ..... 90
Figure 4-14: Fatigue damage showing the effect of soil and marine growth ..... 90
Figure 4-15: Dynamic response with/without marine growth ..... 91
Figure 4-16: Effect of transition piece on the dynamic response ..... 92
Figure 4-17: Effect of transition piece on the fatigue damage ..... 93
Figure 4-18: Effect of scour size on the dynamic response ..... 94
Figure 4-19: Visualization of scour and its effect on fatigue damage ..... 94
Figure 4-20: Types of grouted connections. (a) Pile in leg. (b) Leg in pile ..... 95
Figure 4-21: Effect of grouted connection on the dynamic response ..... 96
Figure 4-22: Effect of grouted connection on fatigue damage ..... 97
Figure 5-1: Topology optimisation workflow (Adapted from [151]) ..... 101
Figure 5-2: Design and Non-design space of an aircraft's lever (Adapted from [152]) ..... 102

Figure 5-3: Flowchart of computational approach ..... 105
Figure 5-4: Comparison of integrated and superelement models in Bladed ... 107
Figure 5-5: Extreme hydrodynamic loading curve in a 50-year return period . 108
Figure 5-6: 3D display of the meshed model ..... 110
Figure 5-7: Representation of OC4 jacket model and TO design space ..... 110
Figure 5-8: Reconstructed model in Genie ..... 111
Figure 5-9: Topology optimisation iterative process ..... 113
Figure 5-10: Spectral convergence of Mode 10 and Mode 25 ..... 116
Figure 5-11: Spatial convergence of the optimised model ..... 117
Figure 5-12: Visual representation of joints and locations of cans/stubs ..... 118
Figure 5-13: Visual representation of the location of sections ..... 121
Figure 5-14: Contour of fatigue damages of the TD-7 model ..... 128
Figure 5-15: Fatigue damage of the most critically damaged brace ..... 128

# LIST OF TABLES

Table 2-1: Preliminary design approaches [41] ..... 14
Table 2-2: Summary of design load cases ..... 24
Table 3-1: Wind power class [117] ..... 49
Table 3-2: Monthly wind power class ..... 51
Table 3-3: Properties of (a) target data and (b) reference data. ..... 52
Table 3-4: Comparison of the target and long-term predicted data ..... 55
Table 3-5: Parameters for Monte Carlo Simulation ..... 63
Table 4-1: K-13 site environmental data ..... 70
Table 4-2: NREL 5MW specifications ..... 71
Table 4-3: OC4 jacket support structure parameters ..... 72
Table 4-4: Soil profile of k-13 deep-water site ..... 75
Table 4-5: Comparison of natural frequencies with the reference values ..... 77
Table 4-6: Static deformation of the baseline wind turbine model ..... 78
Table 4-7: Design load cases ..... 80
Table 4-8: Scatter diagram ..... 80
Table 4-9: Comparison of modal frequencies of original and superelement model ..... 83
Table 5-1: Aerodynamic loads (50 years return period) ..... 108
Table 5-2: Location of braces in OC4 and optimised model ..... 112
Table 5-3: Superelement convergence of the optimised model ..... 114
Table 5-4: Section with thickness variation ..... 121
Table 5-5: Sections with thickness and diameter variation ..... 122
Table 5-6: Effect of thickness on the dynamic response ..... 123
Table 5-7: Effect of thickness and diameter on the dynamic response ..... 124
Table 5-8: Effect of thickness variation on the fatigue damages ..... 125
Table 5-9: Effect of diameter and thickness variation on the fatigue damages ..... 127

# NOMENCLATURE

| | |
|---|---|
| $a$ | Crack depth |
| $\alpha$ | Roughness coefficient |
| $C$ | Intercept of the S-N curve with the log of the number of cycles N |
| $C_d$ | Drag coefficient |
| $C_{D,T}$ | Drag coefficient of the tower at any height |
| $c$ | Celerity |
| $C_m$ | Intertia coefficient |
| $D(z)$ | Tapered diameter of the tower |
| $d$ | Water depth |
| $e$ | Wave amplitude |
| $F_h$ | Hydrostatic load |
| $f_p$ | Peak frequency |
| $G_o$ | Design area volume |
| $G_y$ | Overall material volume |
| $H_{1/3}$ | Significant wave height |
| $J$ | Displacement matrix |
| $K$ | Stress intensity factor |
| $K_w$ | Wave number |
| $K_c$ | Fracture toughness |
| $K_{lc}$ | Plain strain fracture toughness |
| $\lambda$ | Wavelength |
| $M$ | Stiffness matrix |
| $o$ | Shape factor |
| $P$ | Penalty factor |
| $R$ | Volume ratio |
| $\sigma$ | Stress |
| $\sigma_d$ | Design stress |
| $T_z$ | Average zero-crossing wave period |
| $u$ | Horizontal fluid velocity |
| $V_c$ | Current velocity |

| | |
|---|---|
| $\bar{V}_r$ | Hub height wind speed |
| $\bar{V}$ | Variation of wind speed with height |
| w | Vertical fluid velocity |
| Y | Geometry factor |
| $Z_{min}$ | Minimum relative density factor |
| ω | wave frequency |
| Φ | Velocity potential |
| API | American Petroleum Institute |
| BESO | Bi-directional evolutionary structural optimisation |
| CBO | Colliding bodies optimisation |
| DLC | Design load case |
| DNV | Det Norske Veritas |
| ETM | Extreme turbulence model |
| FLS | Fatigue limit state |
| GA | Genetic algorithm |
| IEC | International Electrotechnical Commission |
| LCOE | Levelized cost of energy |
| MCP | Measure correlate predict |
| NTM | Normal turbulence model |
| NSS | Normal sea state |
| OWT | Offshore wind turbine |
| OD | Outer diameter |
| PDF | Probability density function |
| PSO | Particle swarm algorithm |
| RNA | Rotor nacelle assembly |
| SCF | Stress concentration factor |
| SWM | Sesam wind manager |
| TO | Topology optimisation |
| TP | Transition piece |
| WPD | Wind power density |
| WPC | Wind power class |

# 1 Introduction

Offshore wind energy is fast expanding as a viable and environmentally friendly renewable energy source. Many countries, including the UK, China, Germany, Denmark, Netherlands, and Norway, have established large offshore wind farms to achieve their renewable energy targets and reduce carbon emissions. From 2010 to 2018, the total installed wind energy capacity in Europe generated by Offshore Wind Turbines (OWT) witnessed a substantial rise, growing from 84 GW to 189 GW [1]. The capital cost accounts for 33-50% of the entire cost of an offshore wind project, with the foundation accounting for up to 30% [2]. In order to speed up the adoption and reduce the cost, there is a need to constantly improve the design of OWT foundations.

An OWT faces a combination of complex loads throughout its service life of around 20-25 years. The design life of offshore support structures is mainly governed by fatigue damage accumulation [3]. These loads include inertia loads from the Rotor-Nacelle Assembly (RNA) mass, aerodynamic loads from the rotor rotation and airflow over the tower, hydrodynamic loads from waves/currents, and foundation loads transferred through the soil [4]. The amplitude and frequency of these loads vary depending on the stochastic wind/wave climate. Factors like turbine control operation, marine growth, and scour around the foundation also affect the loads.

The complexity and computationally expensive nature of time-series fatigue analysis force the researchers to make simplified assumptions, which impacts the accuracy of modern-day research. For instance, designers often generate the loads analytically instead of through integrated tools. The dynamic coupling between the RNA, tower, and foundation is ignored or simplified. Some researchers ignore the effect of pile-soil interaction. Fatigue calculations are conducted in the frequency domain instead of the more accurate time domain. There is limited literature performing integrated dynamic analysis and stochastic

fatigue calculations to evaluate novel foundation designs based on optimisation algorithms.

Due to the above reasons, this research employs a multidisciplinary approach combining structural optimisation, integrated aero-hydro-servo-elastic simulations, and fatigue assessment. The primary objective is to design an innovative jacket substructure that meets design standards while achieving substantial mass and cost reduction. The research will contribute significant new knowledge regarding jacket foundation design that can benefit the offshore wind industry. The integrated computational framework and detailed findings can aid designers in developing improved support structures.

## 1.1 Problem definition

Conventional offshore jacket foundations are conservative and over-designed because their design was inspired by the oil and gas industry [5], [6]. However, this over-engineering results in excess, redundant materials that drive up the cost of offshore wind energy. New design optimisation techniques offer potential pathways to develop novel support structures with substantial mass and cost reductions.

This research aims to address the limited utilisation of modern computational techniques to improve the fatigue design life and cost-competitiveness of jacket foundations for offshore wind turbines. The thesis will develop a comprehensive computational workflow integrating optimisation, multi-physics simulations, and fatigue life estimation. The framework will incorporate various software tools to facilitate obtaining and evaluating mass-reduced, cost-effective offshore wind turbine jacket support structures while ensuring structural reliability over 20-year life cycles. The designs, analysis approach, and specific framework implementation will provide critical insights and guidelines to promote the application of optimisation methods in offshore wind farm support structures.

## 1.2 Research gap

Based on the literature review (in Section 2), the application of Topology Optimisation (TO) in the design of offshore jacket foundations has not been extensively explored, making it an area with untapped potential. The published research is relatively recent and suggests fatigue life calculation in the future. This research is the first to propose a framework that integrates TO with fatigue life analysis and provides computed results for the fatigue life of the innovative design. The research also provides a high-fidelity integrated simulation approach for comprehensive fatigue evaluation during jacket foundation design. Moreover, this research has incorporated the impact of optimised joint design, which represents a novel aspect not previously explored in the existing research. The comprehensive approach suggested by the research can help address the design challenges of cost-effective offshore jackets and tripod foundations.

## 1.3 Aim and objectives

This research aims to develop an optimised offshore wind turbine jacket foundation design through advanced computational methods and assess its structural integrity. To achieve this goal, the specific objectives of the thesis are as follows:

- To provide a methodology to estimate the long-term environmental loads acting on the offshore wind turbines.
- To provide an integrated dynamic analysis framework and obtain realistic fatigue loading through coupled aero-hydro-servo-elastic simulations in the time domain.
- To quantify the impact of key design parameters on offshore wind turbine foundations' dynamic response and fatigue life.
- To develop a comprehensive framework that integrates topology optimisation with fatigue life analysis to obtain innovative offshore jacket designs.
- To compare and assess the performance of the topology-optimised jacket designs in terms of mass reduction, dynamic response, and fatigue life enhancement against the reference model.

## 1.4 Structure of the thesis

Following this introduction chapter, Chapter 2 critically reviews the relevant literature on offshore wind energy and wind turbine support structures. The chapter discusses various types of offshore foundations and sources of loads. Additionally, it explores design standards and code of practices for offshore wind turbine support structures. The chapter also reviews fatigue design methodologies and finite element analysis methods, emphasising the significance of structural optimisation in offshore foundations. Chapter 3 discusses the wind resource evaluation and estimates the wind farm revenue for a case study site using real-time LIDAR data. This provides the methodology to calculate the environmental loads used for fatigue life estimation for the later chapters. Chapter 4 focuses on the dynamic response and fatigue analysis of the reference offshore jacket foundation model using coupled aero-hydro-servo-elastic simulations. Moreover, the methodology to generate the base model and fatigue life calculation is also presented, which is used in the following chapter to obtain novel designs. Chapter 5 applies topology optimisation techniques to redesign the jacket foundation for reduced mass and improved fatigue life. The process of topology optimisation, model reconstruction, and fatigue evaluation using the hot-spot stress method is also explained. Moreover, the parametric models are generated, and their dynamic behaviour and fatigue damages will be compared. Chapter 6 provides the research conclusion and discusses the limitations and recommendations for future work. Figure 1-1 shows the research methodology for the thesis and describes how different chapters are connected in the research process.

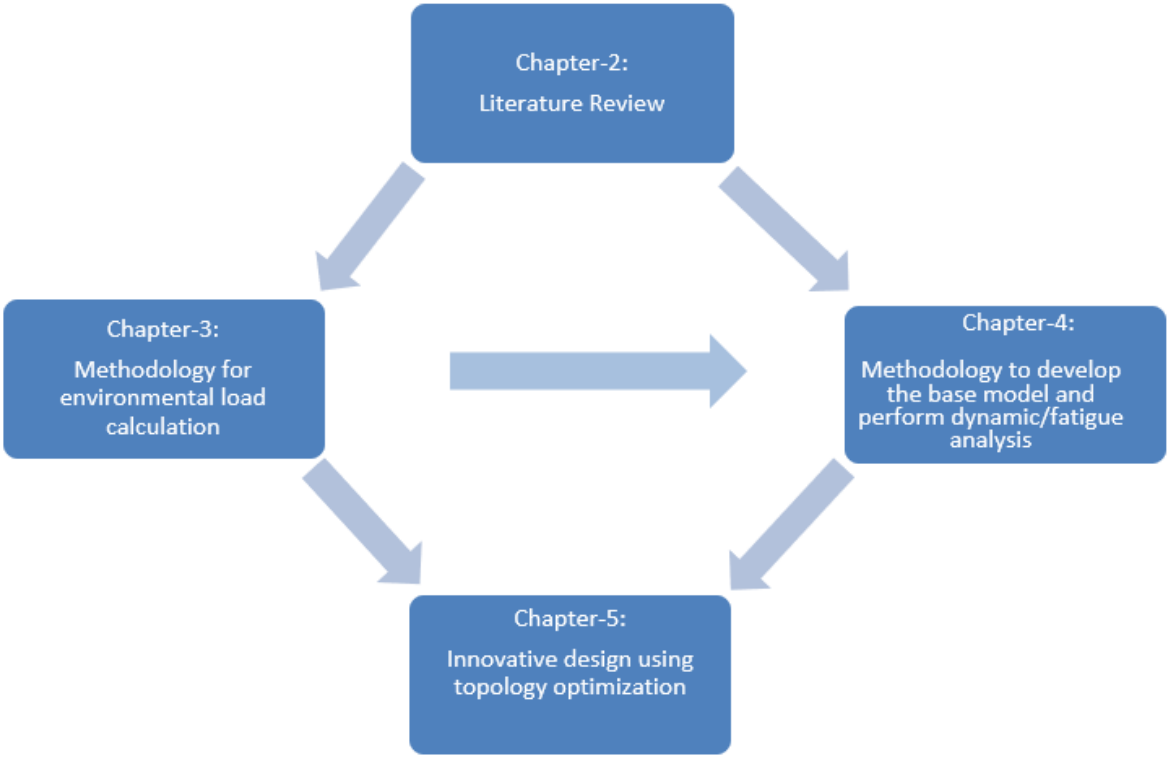



**Figure 1-1: Interconnection of chapters**

# 2 Literature Review

Offshore wind energy is rapidly growing as a vital renewable energy source worldwide. However, high costs remain a significant barrier to the widespread adoption of offshore wind technology. The support structure accounts for 10-25% of the total capital cost of an offshore wind turbine (OWT) system [7]. Therefore, design optimisation of support structures can substantially reduce overall costs.

This chapter reviews research on the design and optimisation of jacket foundations for OWTs. Subsection 2.1 provides an overview of offshore wind energy around the globe. Subsections 2.2 and 2.3 discuss offshore wind turbine support structures and the loads acting on the OWTs. Subsections 2.4, 2.5, and 2.6 provide reviews of design standards for offshore foundations, fatigue design methodologies, and FE analysis methods. Subsection 2.7 examines the use of various optimisation algorithms to improve jacket designs and reviews the use of these algorithms in the literature.

## 2.1 Offshore wind energy

### 2.1.1 Global growth trends

Global offshore wind projects are expected to grow more than tenfold by 2035, reaching a capacity of 519 GW [8]. The global offshore wind industry experienced its most successful year in 2021, adding 21.1 GW of new capacity worldwide [9]. The wind energy capacity of Europe has reached 255 GW, and 30 GW comes from offshore wind [10]. Under net zero commitments, European countries aim to scale offshore wind capacity to 300-450 GW by 2050 [11].

China is the leader in offshore wind in the Asia-Pacific area with more than 16 GW installed capacity and plans to achieve a 50 GW target by 2025[12]. Japan, South Korea, and Taiwan have plans for 7 GW, 12 GW, and 5.7 GW of offshore wind, respectively [13]. Although, the offshore wind market in the United States is still in its early stages. The New York, New Jersey, Massachusetts, and Virginia states have set goals of exceeding 25 GW by 2035 [14]. Industry predictions

predict global offshore wind capacity to reach 330 GW by 2030 and more than 2 TW by 2050 [15].

Despite its huge potential, offshore wind energy is often criticized for its increased costs. The UK is facing criticism about the cost reduction track record due to supply chain pressures, cost increases due to inflation, higher interest rates, and the growing cost of project finance [16]. However, the levelized cost of energy (LCOE) for offshore wind has decreased from historic highs of 200$/MWh to a range of 61-116$/MWh in 2021 [17]. According to cost models, it may further decrease to $53/MWh by 2035 for the fixed-bottom offshore wind turbines [18]. The cost of offshore wind technology is being reduced with the combination of innovative technology and the use of bigger wind turbines. Larger wind turbines required new projects to be installed in greater water depths. Figure 2-1 shows the trend in the increase in the size of wind turbines.

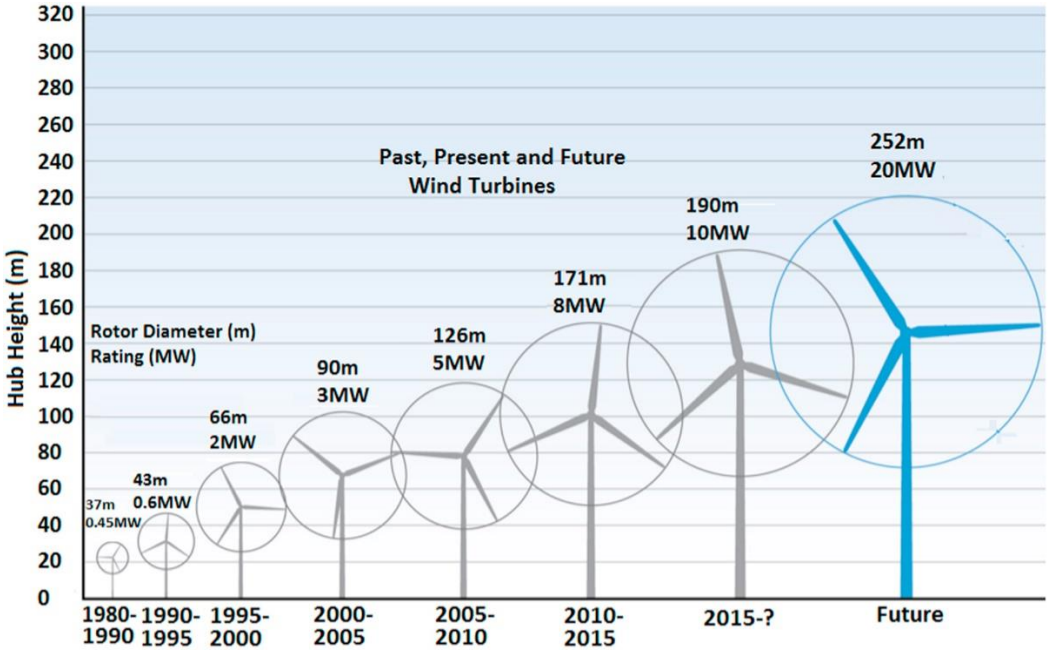



**Figure 2-1: Growth in size of wind turbines (Adapted from** [19])

### 2.1.2 Drivers and challenges

Offshore wind offers both environmental and economic advantages. It delivers clean, renewable electricity while creating employment and revitalizing port

infrastructure in coastal regions [20]. Several factors support the rapid growth of offshore wind:

- Abundant resource potential compared to the onshore wind with stronger and consistent winds
- Declining costs due to technological advancements
- Lower visual impact than onshore wind
- Ability to scale up to multi-GW capacities and turbine sizes
- Collaborations with the offshore oil/gas industry

Despite the enormous potential, offshore wind energy faces multiple challenges:

- High capital expenditures, especially for foundations and subsea cables
- Operation and maintenance costs due to accessibility constraints
- Corrosion and fatigue loading in the harsh offshore environment
- Logistics and supply chain problems due to the developing nature of the industry
- Grid integration difficulties due to variability and distance from shore
- Need for purpose-built installation vessels

### 2.1.3 Support structure innovation needs

The support structure is the most critical part of the economics of offshore wind. The cost of support infrastructure can account for up to 21% of the total cost of the wind farm [21]. Foundation costs are especially high in deeper waters exceeding 50-60 meters. Monopile foundations were the first large-scale offshore substructures to be deployed, accounting for 80% of operational capacity today [22]. According to a cost comparison study by Damiani et al. [23], monopile foundations are more cost-effective for water depths below 40 m. A jacket and floating foundations are often used for depths greater than 40 m.

The offshore oil and gas sector has grown considerably; lessons are gained and applied to the offshore wind sector. However, the offshore wind industry lacks the historical knowledge and data sources to do that. Their designs were mainly based on the design codes and industry standards of the American Petroleum Institute (API) and Det Norske Veritas (DNV) [6]. However, the problem with these

design codes is that they generate conservative and bulky designs, resulting in higher offshore wind costs.

Lowering the cost of offshore wind energy is essential to enhance adoption and unlock the full potential of Offshore Wind Turbines. Currently, efforts are being made to improve the designs of offshore foundations to enhance structural integrity and reduce costs with innovative designs. Since foundations account for a sizeable share of project expenditures, design optimisation provides major opportunities for LCOE reductions.

## 2.2 Offshore wind turbine support structures

the offshore wind industry is currently shifting towards installing larger wind turbines in deeper oceans to increase the industry's efficiency. The research on the suitability of a foundation type is on the rise. There are five commonly used types of Offshore Wind Turbine (OWT) foundations: gravity-based, monopile, tripod, jacket, and floating. Other variations are essentially derived from these four basic types [24]. Figure 2-2 shows commonly used types of support structures of OWTs. A brief description of these is discussed in the next section.

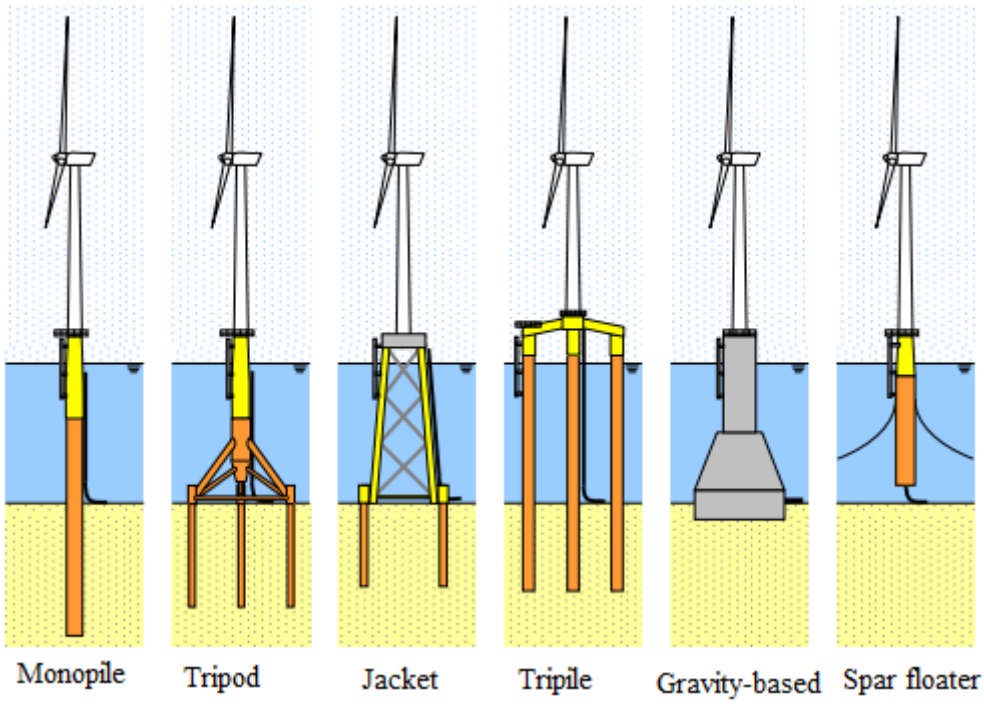



**Figure 2-2: Types of offshore wind foundations (Adapted from** [25]**)**

### 2.2.1 Monopile

Monopile is the most used foundation type in the offshore wind industry, making around 80% of the total installations. A monopile comprises a single, large-diameter steel tube pile driven into the seabed. Their diameter can range from 2 m to 8 m and have lengths from 30-85 m range [26]. These foundations have a simple, proven technology and an established supply chain. Monopiles are suitable for softer soils and are feasible up to around 30 meters in depth.

### 2.2.2 Jacket

The jacket is the offshore wind industry's second most widely used foundation type. Jackets have numerous welded steel sections arranged in a truss configuration to give stability and strength. Designs with three and four legs are often used. Jackets have an advantage beyond 40 meters depth where the practicality of monopiles is less. These have higher stiffness than monopiles and lower material volume, but their manufacturing cost is higher. Their manufacturing and design cost is higher because of a higher number of joints.

### 2.2.3 Tripod

Tripod foundations have three main tubular legs connected by braces and are suitable for 25- 50 m water depth. Compared to four-legged jackets, these are primarily designed for ease of transport and installation [27]. These structures offer higher stiffness and water depth usage than monopiles but have complex fabrication processes and supply chain issues due to the insolvency of early adopters [26].

### 2.2.4 Gravity based foundations

A gravity base foundation relies on its heavy weight and large outer base diameter rather than pile fixation for stability on the seabed [28]. These foundations have an optimal water depth of 30-60 m, but their use is still limited to shallow water because of the cost of transporting such heavy structures. Another disadvantage of gravity-based substructures is that significant scour protection and soil preparation are needed before installation [29].

### 2.2.5 Floating foundations

Floating wind turbine foundations are ideal for water depth exceeding 60 m, making them an ideal choice when fixed bottom foundations are not suitable. These are anchored through mooring systems, and there is no requirement for seabed preparation [30]. The main advantage is the extraction of higher wind resources further away from the shore. The major floating offshore wind foundations include spar buoys, tension leg platforms, and semi-submersible platforms.

## 2.3 Sources of loads

An offshore wind turbine faces a series of complex loads during its service life. The design standards DNV-ST-0126 [31] and IEC 61400-3 [32] suggest the list of loads to consider while performing analysis. The DNV-RP-C205 standard [33] provides guidance for estimating environmental loads. The loads an offshore wind turbine faces are usually classified into the following groups. Figure 2-3 depicts various loads acting on an offshore wind turbine jacket foundation.

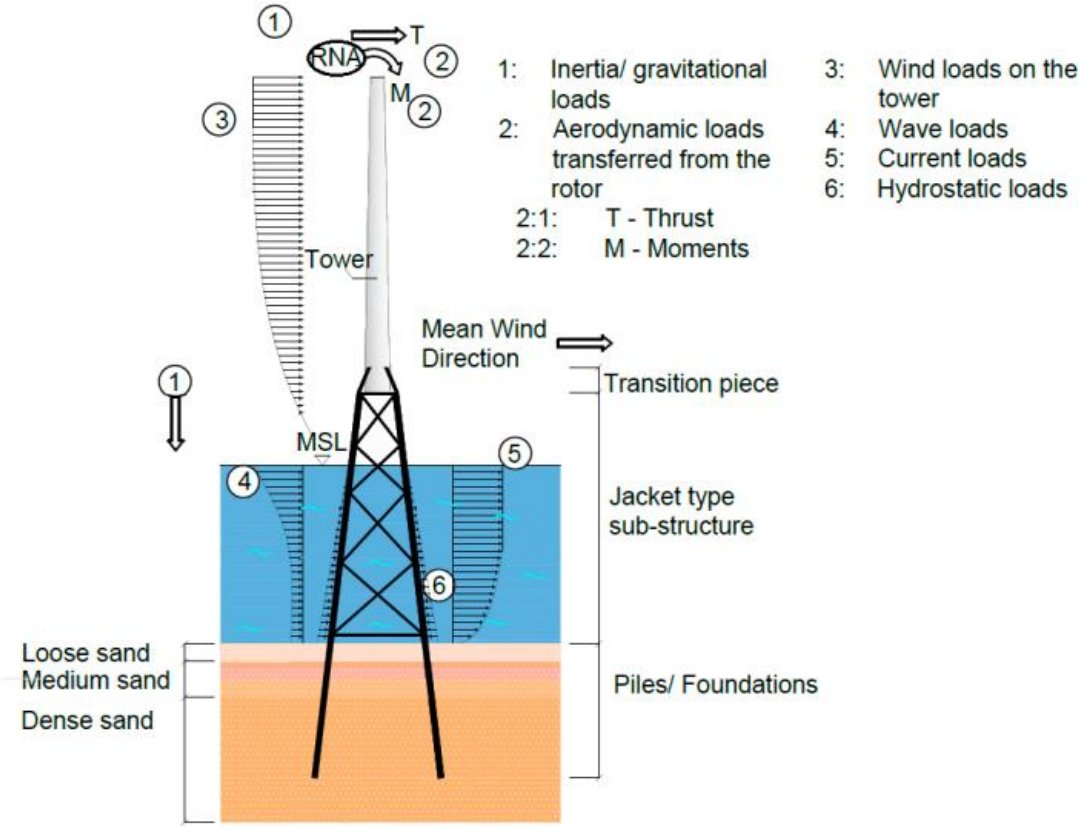



**Figure 2-3: Sources of loads on jacket foundation (Adapted from** [34]**)**

### 2.3.1 Inertia

The loads are encountered due to the self-weight of the Rotor Nacelle Assembly (RNA), Transition Piece (TP), tower, and foundation. These loads contribute most to the buckling and significantly affect the modal analysis. The structure can fail if an OWT encounters resonance due to poor design, emphasizing the need to consider these loads during the design process.

### 2.3.2 Wind

The wind loads are caused by the drag change with the height and the mean wind speed. The power-law profile is used to examine the variation of wind speed with height using Equation 2-1.

$$\bar{V}(z) = \bar{V}_r \left(\frac{z}{z_r}\right)^{\alpha} \qquad \textbf{2-1}$$

Where, $\bar{V}_r$ represents the hub height wind speed, and α shows the roughness coefficient, usually 0.115 for offshore conditions. The wind loads as a function of height can be calculated by using Equation 2-2. Where D(z) represents the tapered diameter of the tower and $C_{D,T}$ shows the drag coefficient of the tower at any height z.

$$\boldsymbol{F_{twr}(z) = \frac{1}{2}\rho_a C_{D,T} D(z)\, \bar{V}_r{}^2(z)} \qquad \textbf{2-2}$$

Due to airflow interaction, the combination of static and dynamic loads acting on the wind turbine rotor generates the rotor's aerodynamic loads. The loads faced by the rotor are transferred to the top of the tower.

A wind resource analysis at a given site is performed to calculate the aerodynamic loads acting on the structure. Section 3.3 explains the methodology to perform such analysis and includes a case study from a wind farm where wind speed was measured using a Lidar device. The wind resource assessment and economics of electricity generation in the Sinai Peninsula of Egypt were studied by Ahmed [35], [36]. Khan and Tariq [36] compared the wind resource assessment using Sonic Detection and Ranging (SODAR) with the metrological mast in Pakistan and concluded that wind resource assessment using SODAR is cheaper. The reliability of wind profiling using LIDAR is also discussed in [37], [38]. Mifsud et al. [38] analysed the performance of different Measure-Correlate-Predict (MCP) methodologies by gathering wind data from the LIDAR system. Fazelpour et al. [39] used the Windographer software to perform wind resource analysis, but they could not access the real wind data from LIDAR.

### 2.3.3 Wave

Sea waves are formed when the ocean's surface interacts with the wind [40]. These waves are random and of irregular shape. The key factors influencing wave generation are wind speed, wind direction, and fetch length, defined as the length of the water surface over which the wind blows. The recommended practices from different standards guide the analysis and prediction of environmental loads, including the loads acting on the jacket foundation due to

waves and currents. One such practice is published in DNV-RP-C205, “Environmental Conditions and Environmental Loads” [33].

Two methods are commonly used in the initial design of offshore structures: the design wave approach and the design based on statistical wave description. Table 2-1 compares these approaches against the suitability and limitations of each approach. Currently, design approaches utilise both methods to benefit from their individual strengths [41].

**Table 2-1: Preliminary design approaches** [41]

| Approach | Explanation | Suitable for | Limitation |
|---|---|---|---|
| Design wave approach | For the use as the worst encountered condition, given the return period (50/100 years), the highest wave likely to occur in the return period is statistically estimated. | Design against structure failure | Fatigue damage estimation |
| Design to statistical wave description | The waves are represented as a probability distribution, and the probability of occurrence is estimated based on wave height, period, and direction. For each range of these parameters, average number of waves is estimated | - Fatigue damage estimation<br>- Large structures in small waves<br>- Linear waves | - Estimation of loads when drag is greater than inertia force<br>- Estimation of loads from high waves |

#### 2.3.3.1 Wave theories

Wave theories are needed to estimate fluid acceleration, velocity and pressure at any point under the wave, which is required to determine the forces acting on the structure. These wave forces set the important aspect of the design of offshore structures.

This simplest yet powerful theory to provide analytical solutions for the waves was developed by G.B. Airy in 1845, hence also called the Airy linear small amplitude wave theory. The Airy theory is based on the following assumptions.

- The sea water is assumed to have constant depth and uniform density.
- The wave motion is irrotational.
- Viscosity and surface tension are neglected.
- Non-linear terms in the Navier-Stokes equation are neglected.

For an irrotational and incompressible flow, the final form of Airy velocity potential is given by Equation 2-3. The complete derivation can be referred to in [41]

$$\emptyset = -ec\,\frac{\boldsymbol{coshk(y+d)}}{\boldsymbol{sinhkd}}\,\cos\left(k_w x-\omega t\right) \qquad \textbf{2-3}$$

Where,

Φ = velocity potential (Units are $m^2/s$)

c = celerity (distance travelled by a crust per unit time) (m/s)

e = wave amplitude (m)

$k_w$ = wave number (1/m)

d = water depth (m)

x,y = horizontal and vertical coordinates

ω = wave frequency passing in a certain time (rad/s)

t = time (s)

The horizontal fluid velocity (u) and vertical fluid velocity (w) can be found in Equations 2-4 and 2-5, respectively. Moreover, the formulas for velocity potential, horizontal and vertical velocities for deep water conditions are given in Equations 2-6, 2-7 and 2-8, respectively [41].

$$u = \frac{\partial \emptyset}{\partial x} = -ac\ \frac{coshk(y+d)}{sinhkd}(-\mathrm{ksin}(kx-\omega t)) \quad \text{2-4}$$

$$w = \frac{\partial \emptyset}{\partial y} = -ack\frac{sinhk(y+d)}{sinhkd}(\cos(kx-\omega t)) \quad \text{2-5}$$

$$\Phi_{dw} = -ace^{ky}\cos(kx-\omega t) \quad \text{2-6}$$

$$u_{\infty} = \frac{\partial \Phi}{\partial x} = ack\ e^{ky}\sin(kx-\omega t) \quad \text{2-7}$$

$$w_{\infty} = \frac{\partial \Phi}{\partial y} = -ack\ e^{ky}\cos(kx-\omega t) \quad \text{2-8}$$

The linear wave theory is applicable in simplified conditions, such as when the wave height is low. The dynamic and kinematic boundary conditions can be applied at the still water level but not on the wave-disturbed surface. However, in the case of larger wave amplitude, there is a need to apply nonlinear wave theory. In order to satisfy non-linear and free surface boundary conditions, higher orders terms are added to the velocity potential. The velocity potential for Stokes' 3rd-order wave theory is given in Equation 2-9.

$$\emptyset = \frac{c}{k}\Big[F_1 coshk(y+d)\sin(kx-\omega t) + \frac{1}{2}F_2 cosh2k(y+d)sin2(kx-\omega t) + \frac{1}{3}F_3 cosh3k(y+d)sin3(kx-\omega t)\Big] \quad \text{2-9}$$

Where,

$$F_1 = ka\ \frac{1}{sinhkd} - (ka)^2\frac{1+5cosh^2kd}{8sinh^5kd}$$

$$F_2 = \frac{3}{4}\ (ka)^2\frac{1}{sinh^4kd}$$

$$F_3 = \frac{3}{64}(ka)^3\frac{11-2cosh2kd}{sinh^7kd}$$

The 5th-order wave theory of Stokes is complex to perform, and computers are typically used to perform calculations in the offshore industry. The computer is

supplied with inputs to calculate velocity, acceleration, and pressure at any given coordinate.

All the theories developed for offshore design purposes have some limitations. Moreover, the selection of wave theory for design is always a compromise between accuracy and computational effort. Figure 2-4 uses different parameters that separate wave regimes into different parts. The wave theories can be selected based on the values of $d/gT^2$ and $H/gT^2$. The linear wave theory can be used for small to moderate sea states, hence unsuitable for complex fatigue life simulations under extreme conditions [42]. Moreover, Stokes' 5th-order wave is useful when using the design wave approach [41], [42]. It should also be noted that Stokes' 5th-order theory can not be used for shallow water.

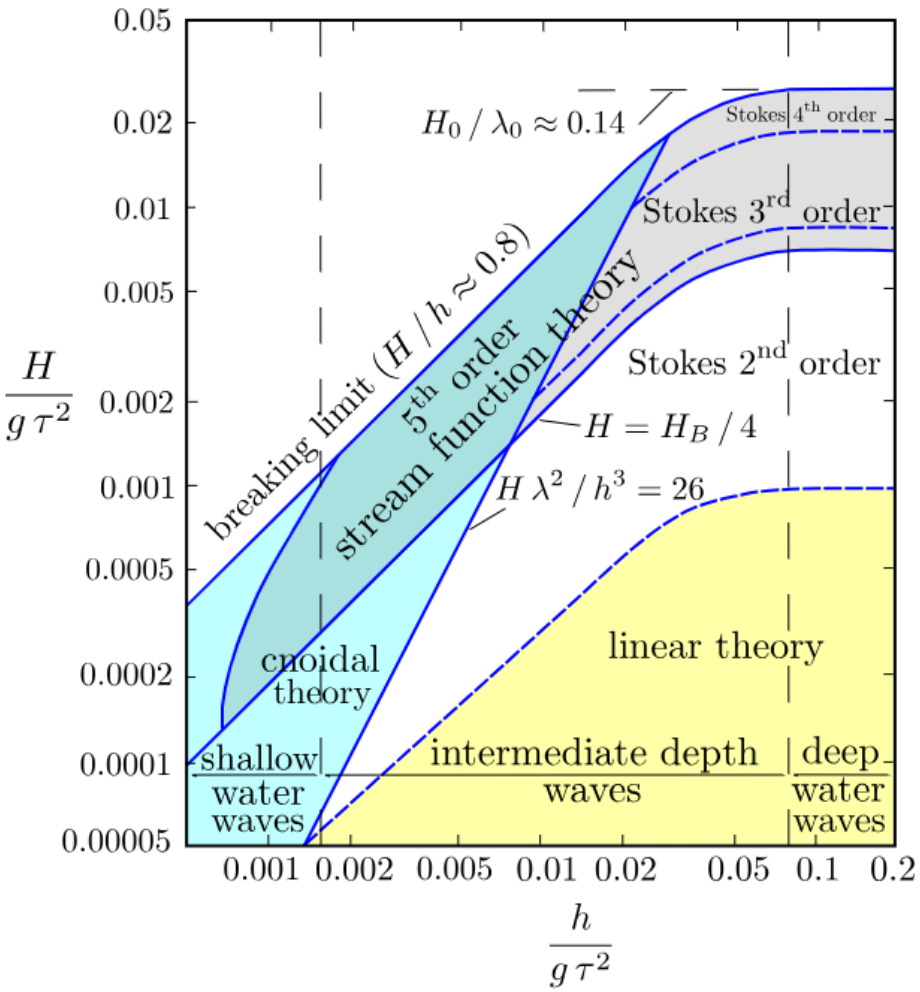



**Figure 2-4: Selection of wave theory (Adapted from** [43]**)**

### 2.3.3.2 Probabilistic approach

Wave properties are not often fully explained by the wave theories discussed in the previous section. This is because the energy of the sea surface moves in both the wave direction and angular directions. However, a probabilistic approach can be used to find short and long-term wave properties. It can also help determine extreme wave height that may occur in 50 or 100 years. A similar approach is used in this research to explain short and long-term wind properties in Section 3.3.2. The evaluation of the structure to withstand such waves is one of the design load cases of offshore structures, which are defined later. The properties of a wave's elevation, such as its velocity, acceleration, and pressure, are determined by a Gaussian random process considered stationary and unchanging over time. The probability of a random variable (wave elevation) falling in a given range is defined by the probability density function (PDF).

Several spectral shapes define the shape of the wave spectrum, and the most important ones are JONSWAP and Pierson-Moskowitz wave spectra. The Pierson-Moskowitz wave spectrum is often used for the fully developed sea states [44], [45], and the JONSWAP spectrum is used where fetch is limited (underdeveloped sea states) [45]. The expressions for calculating significant wave height and average zero crossing wave period for a given wind speed (V) are given in Equations 2-10 and 2-11, respectively. Equation 2-12 shows the Pierson-Moskowitz wave spectrum in terms of frequency, where A is the Philips constant (0.0081), and $f_p$ is the peak frequency.

$$H_{1/3} = 2.12\ X\ 10^{-2} V^2\ (m) \qquad \textbf{2-10}$$

$$T_z = 0.81\ \frac{2\pi V}{g} \qquad \textbf{2-11}$$

$$S_{\eta\eta}(f_p) = \frac{Ag^2}{(2\pi)^4 {f_p}^5}\ .\ e^{\left[-\frac{5}{4}\left(\frac{f_p}{f_m}\right)^{-4}\right]} \qquad \textbf{2-12}$$

The JONSWAP spectrum is given in Equation 2-13. When the shape parameter (γ) equals 1, the JONSWAP spectrum equals the Pierson-Moskowitz spectrum

[46]. Figure 2-5 compares JONSWAP and Pierson-Moskowitz spectrum for a significant wave height of 5 meters and a mean zero crossing period of 8 seconds.

$$S_{\eta\eta}(f) = \left(\frac{Ag^2}{(2\pi)^4 f^5} \cdot e^{\left[-\frac{5}{4}\left(\frac{f}{f_m}\right)^{-4}\right]}\right) \cdot \left(\gamma^{e\left[-\frac{(f-f_m)^2}{2\sigma^2 {f_m}^2}\right]}\right) \qquad \textbf{2-13}$$

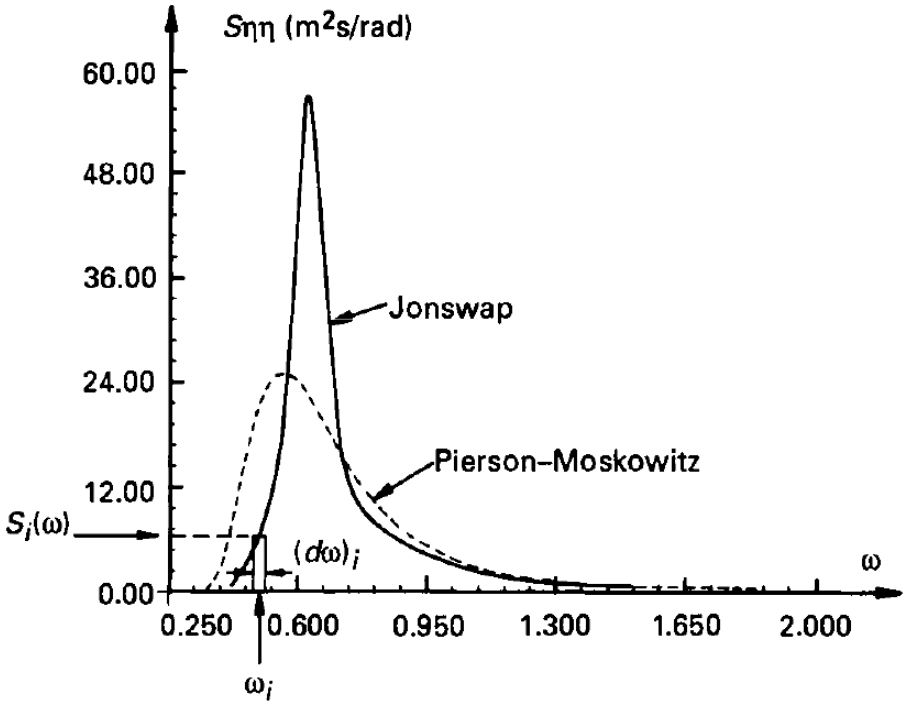



**Figure 2-5: Comparison of JONSWAP and Pierson-Moskowitz spectrum for Hs = 5m and Tz = 8s (Adapted from** [41]**)**

### 2.3.3.3 Short-term wave properties

The short-term wave properties are defined for 20 minutes and 3 hours when the wave properties are constant or vary slowly. The wave elevations are derived from the Gaussian PDF in this time scale and given variance. Since the sea spectrum tends to be of a narrow band, Rayleigh PDF is used for short-term statistics. The Rayleigh PDF written in terms of significant wave height is given in Equation 2-14.

$$P_H(H) = \frac{4H}{{H_{1/3}}^2} . e\left(\frac{-2H^2}{{H_{1/3}}^2}\right) \quad \text{2-14}$$

### 2.3.3.4 Long-term wave properties

During the design phase of offshore structures, a significant amount of data is required to determine their fatigue life and assess the probability of extreme events. This data is usually acquired from the records of wave elevation obtained from buoys, satellites, and platforms or estimated from metrological stations' data. A scatter diagram gives the probability of occurrence of each combination of Hs and Tz using the method of bins (similar to the method discussed in Section 3.3.2.5).

Normally, the data obtained is for 1-3 years, which is insufficient to show the long-term behaviour of the wave. Therefore, the probability of occurrence of significant wave height in 1-3 years is plotted with a distribution function (lognormal, Weibull, and Gumbel distribution). This probability distribution predicts the maximum wave height likely to occur over a very long time (5-100 years). The scatter diagrams are site-specific and can not be generalized for use at any other site. A scatter diagram obtained from the UK Offshore Operators' Association normalized to parts per 1000 is shown in Figure 2-6.

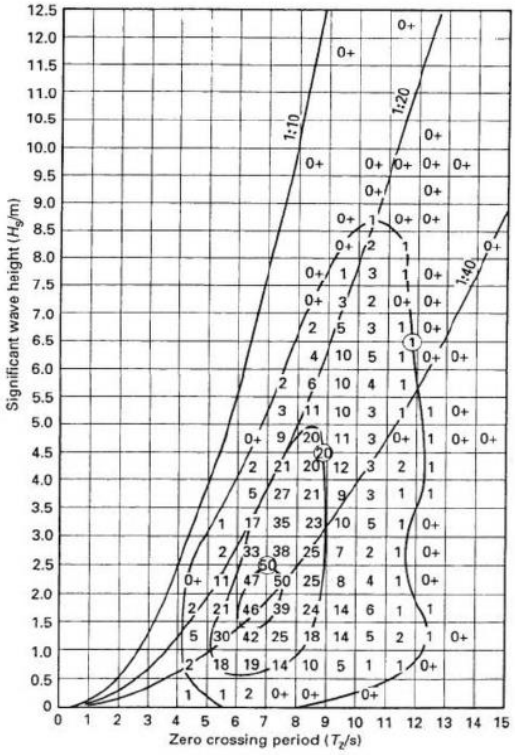



**Figure 2-6: Scatter diagram normalized in parts per 1000 (Adapted from** [47]**)**

Patel et al. performed the wave resource analysis by comparing 19-year ERA5 data with the 12-month measured data at the buoy site and found a spatiotemporal variation of the wave energy [48]. A similar study was performed in [49] to evaluate the wave energy resource. The authors extracted the wave heights, wave periods, and wave directions based on 12 months of wave data from the buoys. The study also presented a methodology to determine wave power density. The effect of environmental conditions, including wind and wave data, on the performance of the wind turbine is given in [50].

### 2.3.3.5 Wave loads

The ratio between the member diameter and wavelength (D/λ) and the ratio of wave height to member diameter (H/D) determines the approach used to estimate loads. Morison's equation is used for a body considered small (D/λ < 0.2), where a small body is assumed not to change the wave characteristics. The equation is valid for vertical piles in shallow water and is also considered valid for cylinders in deep/shallow water if the coefficients of inertia and drag are chosen experimentally. Morison's equation is given in Equation 2-15, Where $C_m$ and $C_d$

are inertia and drag coefficients, D is the member's diameter, $u_x$ and $a_x$ are velocity and acceleration induced by the current and wave. Morison's equation can compute the current and wave loads for the structure submerged in the water [4].

$$F = F_d + F_m = \frac{1}{2}\rho_w C_d D|U_x|U_x + \rho_w C_m \frac{\pi D^2}{4} a_x \quad \textbf{2-15}$$

Like the wind loads, the current loads are height and drag-dependent. Morison's equation describes the sub-surface current velocity by an exponential profile from the mean sea level (MSL) to the seabed [51]. The current velocity can be calculated using Equation 2-16, Where d is the water depth from MSL to the seabed and $V_{c,MSL}$ is the current velocity at MSL.

$$V_c(z) = V_{c,MSL}\left(\frac{d+z}{d}\right)^{1/7} \quad \textbf{2-16}$$

The offshore foundation is immersed in seawater, which results in hydrostatic pressure. The hydrostatic load ($F_h$) is a permanent normal load that increases with depth (h) and can be calculated by Equation 2-17, where g is the gravitational constant.

$$F_h = \rho_w g h \quad \textbf{2-17}$$

## 2.4 Design standards and code of practices

The necessary considerations for the foundation design depend on the site characteristics (wind speed, wind turbulence intensity, wave height/period, water depth), type of foundation (monopile, jacket, floating), turbine characteristics (rated power, rated wind speed, rotor diameter, mass of rotor-nacelle assembly and tower), ground profile, economics, and the type of investor (government or private). The design criteria of the foundations are based on different design codes, and the certification bodies validate if the design is supported by sound engineering and test results.

### 2.4.1 Design codes

The most prominent design codes are provided by the International Electrotechnical Commission (IEC) regulations: IEC 61400-1 [52], IEC 61400-3 [32], IEC 61400-12-1 [53]; DNV guidelines for the design; Design of Offshore Wind Turbine Structures [31], Support Structures for Wind turbines (DNV-ST-0126) [54], and Environmental Conditions and Environmental Loads (DNV-RP-C203) [55]; ISO standard [42], American Petroleum Institute (API) code [56], Eurocode-3 [57], British Standards Institute (BSI) BS EN 61400-3 [58].

A brief introduction to the above-mentioned codes is given below.

- IEC provides guidelines for various kinds of devices that can produce electricity. IEC is one of the biggest organizations that publishes onshore and offshore wind turbine standards.
- DNV is a Norwegian classification society and has given numerous standards and guidelines for the offshore industry. This study has extensively used DNV standards, and the software used for analysis is also developed based on the DNV standards.
- BSI provides design standards for most of the UK industry and helps design and construct offshore wind farms. BSI has published “Design requirements for offshore wind turbines (BS EN 61400-3)”. BSI’s standards are mainly drawn from IEC regulations.
- API is a trade association that has provided regulatory services for the oil and gas industry but has not provided any guidelines for designing offshore wind turbines. Due to the similarity in both industries, their guidelines are of significant importance.
- Eurocode is the European Committee for Standardization that provides a common approach to structural design across the European Union. Their Eurocode-3 standard provides technical rules for the structural design of steel components. The code provides guidelines for material properties and the basis for design for steel components like beams, columns, trusses, and frames.

### 2.4.2 Design load cases

The response of OWTs is investigated based on the design load cases given in the IEC 61400-3 standard on “Design requirements for offshore wind turbines” [32]. The number of design load cases (DLCs) is analysed to ensure the safe operation of the wind turbines throughout their lifetime. However, not all design cases are important for the design of offshore foundations [4]. The selection of the number of DLCs directly impacts the accuracy of the design. For higher accuracy and redesign applications, there is a need to select more DLCs. The study by Arany et al. [59] used five design cases for the basic conceptual design. The design load cases analysed by [60] are summarized in Table 2-2.

**Table 2-2: Summary of design load cases**

| Code | Description | Wind & wave directionality |
|---|---|---|
| DLC 1.2 | It is the only case considered for the fatigue analysis by considering Normal Turbulence Model (NTM) and Normal sea state (NSS) | Co-directional & multi-directional |
| DLC 1.3 | It is used for ultimate loading from Extreme Turbulence Model (ETM) and combined with NSS | Co-directional & uni-directional |
| DLC 1.4 | The ultimate loading case with Extreme Coherent Gust (ECD) and direction change, combined with NSS. | Misalignment |
| DLC 1.5 | The ultimate loading case with extreme shear, NSS and NCM | Co-directional & uni-directional |
| DLC 1.6 a | The ultimate loading case with Severe Sea State (SSS) and NTM | Co-directional & uni-directional |
| DLC 1.6 b | The ultimate loading case with a Severe Wave Height (SWH) of a 50-years return period, and NTM | Co-directional & uni-directional |
| DLC 2.3 | Abnormal case of ultimate loading in the event of Extreme Operating Gust (EOG) and NSS | Co-directional & uni-directional |

| | | |
|---|---|---|
| DLC 6.1 | The ultimate loading case for parked conditions. | Misalignment, Multi-directional |
| DLC 6.2 | This case discusses the loss of electrical power occurring simultaneously with the storm | Misalignment, Multi-directional |
| DLC 6.3 | The ultimate loading case for extreme weather conditions with a 1-year return period | Misalignment, Multi-directional |
| DLC 6.4 | The case used for fatigue analysis in parked condition by considering NTM and NSS | Co-directional, Multi-directional |

## 2.5 Fatigue design methodologies

Fatigue is gradual damage caused to material due to continuous cyclic loading over an extended period. This load slowly deteriorates the object until it eventually breaks. The fatigue life of an object can be categorized into three stages: crack initiation, crack propagation, and crack growth leading to brittle failure [61]. The fatigue damage usually initiates from a hotspot, which may result from some manufacturing defect, stress concentration at a certain point of geometry, or welding defect.

The S-N curve or Linear Elastic Fracture Mechanics (LEFM) crack growth mode can be used to perform fatigue analysis [62]. The DNV recommended practice

given in [31] recommends using the S-N curve method to design offshore wind turbines. However, the industry practice is to use the S-N curve method during the design stage and the LEFM method for the inspection and life-estimation stage.

An OWT faces a combination of complex loads throughout life, and fatigue life is the main performance criterion of OWT foundations [3]. The effect on the fatigue life of monopile foundations was studied using four soil foundation models in [63], which resulted in the variation of fatigue damage by up to 22% based on different soil models. The soil-structure interaction is a key player in offshore foundation fatigue design and is discussed in [64]. The industry standard definition of pile-

soil interaction is inaccurate for offshore foundations with a large diameter (monopile). The PISA project proposed a different soil-pile definition method based on field testing and numerical results [65]. However, the method only shows good accuracy at the testing site and can not be used on other or multi-layered soils. A detailed FEA analysis was performed in [34] based on five constraints (fatigue, stress, vibration, buckling, and deformation). It was observed that fatigue performance is the primary design driver of the jacket foundations. Abdulhakim et al. studied the structural reliability of the jacket subjected to corrosion fatigue [66].

DNV's recommended practice is to calculate the fatigue damages based on the time-series loads because it can consider the real-world complex loading conditions for the entire duration of the load history. This research is based on the time-series fatigue calculation. However, in the literature spectral fatigue analysis is also used. Spectral fatigue calculation involves the frequency domain method where the fatigue life is based on the spectral density of the applied load. However, this approach can not capture the complex dynamic transient events and is more suited for linear systems. The spectral fatigue analysis method was used on an eight-legged oil and gas jacket foundation to calculate fatigue life at each joint. The study showed that 73 joints of the jacket had a service life shorter than 20 years [67]. The research was performed to study the effect of design parameters and foundation types (fixed base, monopile, and caisson) on the dynamic response and fatigue [68]. However, the fatigue analysis was performed in a MATLAB-based tool (MLife) and did not include the time series aspect. The structural redundancy’s effect on fatigue life and life extension was studied in [69]. The author proposes using the fracture mechanics approach along with the fatigue analysis in the future. Thanh-Tuan et al. presented a cost-effective three-legged jacket by studying various bracing patterns. The dynamic response was significantly changed with the change in the bracing pattern [70]. The dynamic responses of monopile and jacket foundations were compared in [71]. The jacket foundation was observed to have a better dynamic response, and the monopile foundation was unsuitable for the Korean offshore wind farm.

### 2.5.1 S-N curve method

Fatigue failure of an object can be determined using the S-N curve, which is based on experimental data and shows the relationship between Stress S and the number of cycles N. The experiments are repeated for similar specimens under stress to obtain the design S-N curve. The design standard developed by DNV and API lists different S-N curves for different details. The difference in the curves is because of the different types of weld connection and environment (air, seawater with cathodic protection, and seawater without cathodic protection).

The stress range at a point is related to the number of cycles to failures with the help of Equation 2-18. Where N is the number of cycles to failure, m is the negative inverse slope of the S-N curve, σ is the stress, and C is the intercept of the S-N curve with the log of the number of cycles N. Figure 2-7 shows a basic S-N curve for different structural details in the air.

$$\boldsymbol{log_{10}(N) = C - m log_{10}\Delta\sigma} \qquad \textbf{2-18}$$

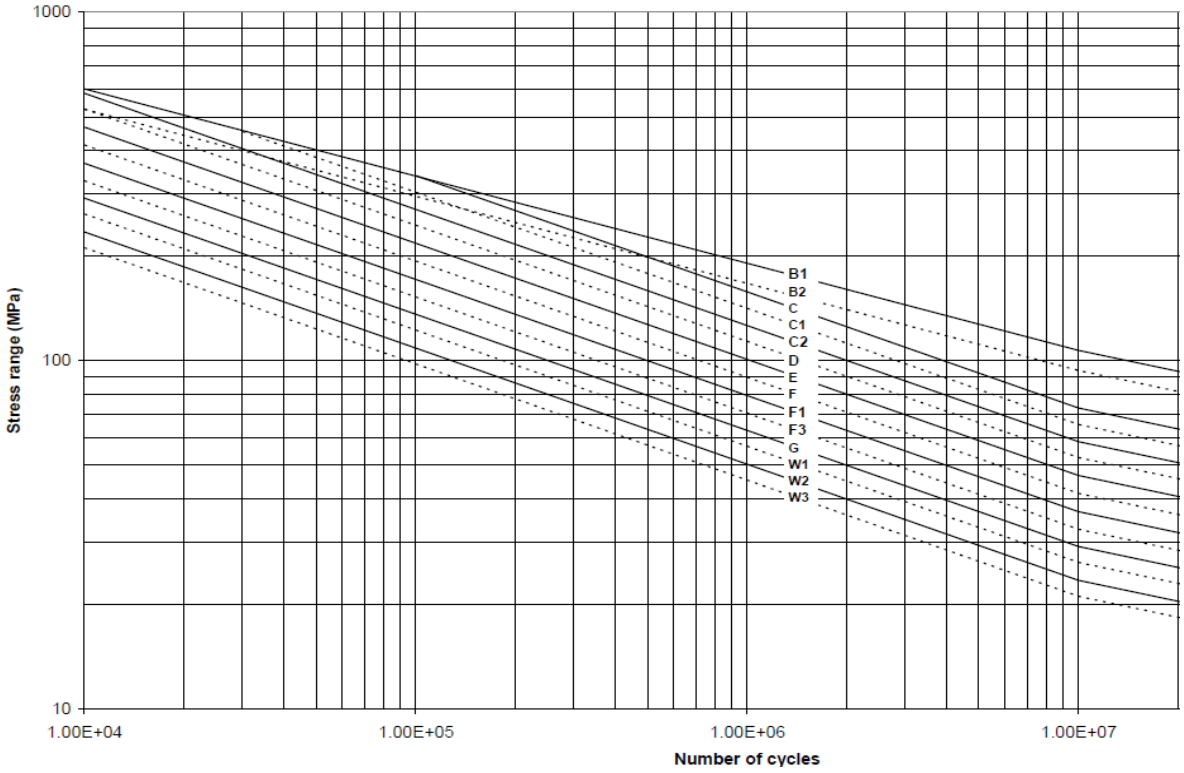



**Figure 2-7: S-N curve for steel in the air** [31]

### 2.5.1.1 Accumulated fatigue damage

The Palmgren-Miner rule, which assumes linear cumulative damage, is used to calculate fatigue damage using the S-N curve. The accumulated fatigue damage (D) is calculated when the long-term stress range is expressed in the stress histogram, which consists of the stress range blocks ($\sigma_i$) with the number of stress repetitions $n_i$ [31]. The accumulated damage until the object under cyclic loading fails is given in Equation 2-19.

$$\boldsymbol{D = \sum_{i=1}^{k} \frac{n_i}{N_i} = \frac{1}{\bar{a}} \sum_{i=1}^{k} n_i (\Delta \sigma_i)^m} \qquad \textbf{2-19}$$

Where,

D = accumulated fatigue damage

m = negative inverse slope of S-N curve

k = number of stress blocks

$n_i$ = number of stress cycles in stress block i

$N_i$ = number of cycles to failure

$\bar{a}$ = intercept of design S-N curve and log of N axis

### 2.5.1.2 Fatigue analysis based on the S-N curve method

The DNV C-203 recommended practice gives three different concepts for calculating stresses based on different definitions of stresses. These methods rely on the definition of stresses combined with the S-N curve. There are different concepts of S-N curves, including:

- Nominal stress S-N curve
- Hotspot stress S-N curve
- Notch stress S-N curve

The nominal stress approach involves comparing a structure's fatigue damage with the permissible stress of the S-N curve. When analysing stress levels for a structure, this method considers the stress experienced by the entire cross-section of the component. It is suitable for structures with uniform stress distributions and simple geometries. Normally, design stress is called the nominal

stress for the weld under consideration. However, if the joint is located in the hotspot region (e.g., hole or structural discontinuity), the stress concentration factor (SCF) is multiplied by the nominal stress. Moreover, for a tubular joint, the design stress is the range of hotspot stresses, which are the greatest value of extrapolation of the maximum principal stress distribution outside the region of weld geometry [55]. This research uses the hotspot stress approach to calculate stresses as it is more suitable for complex geometries and regions of localized stress concentration.

The notch stress S-N curve approach is only used when performing fatigue analysis using other methods is difficult. This method considers the structure's stress levels at critical notch or discontinuity. It is suitable for components that have notches or other stress concentration features. This approach estimates the fatigue life of a component using S-N curves built specifically for notched geometries.

### 2.5.2 Linear Elastic Fracture Mechanics Method

The purpose of Linear Elastic Fracture Mechanics (LEFM), defined by DNV RP-C203, is to determine the fatigue crack that may occur during the service life of a component and ensure that the size of the crack does not exceed a limit that could cause a fracture. The LEFM can complement the S-N curve method in a way that the structural reliability calculated by the fracture mechanics should not be less than that achieved by the S-N data. Since the crack initiation is not included in the LEFM method, the fatigue life derived from LEFM is shorter than the S-N method.

The fatigue analysis using the LEFM method depends on calculating hotspot stresses. The stress value on the hotspots depends on three fracture or crack surface displacement modes given in Figure 2-8.

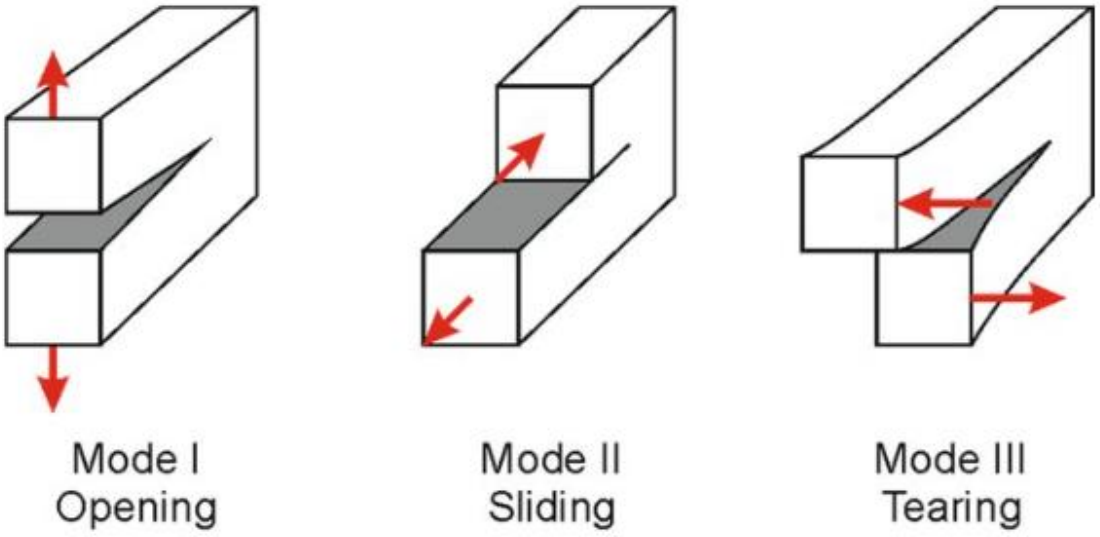



**Figure 2-8: Fracture modes (Adapted from** [72]**)**

The stress intensity factor (K) is an important parameter related to the stress and displacement near the crack tip. It can be calculated accurately by the FE modelling. Alternatively, analytical solutions are given in the recommended standards for relatively simple crack geometry and boundary conditions. However, experimental methods to calculate stress intensity factors are most reliable for tubular joints [62]. Mathematically, the stress intensity factor is related to the nominal stress normal to the crack (σ) and geometry factor (Y) by Equation 2-20. Moreover, the value of Y depends on the geometries of the member, crack and weld.

$$\boldsymbol{K = \sigma Y\sqrt{\pi a}} \qquad \textbf{2-20}$$

Design using LEFM involves the calculation of fracture toughness ($K_c$), which is the critical value of the stress intensity factor at which brittle fracture can occur. The fracture toughness is the function of specimen geometry. However, in mode-1, when $K_c$ is independent of the geometry, then it is called plain strain fracture toughness ($K_{Ic}$). Both $K_c$ and $K_{Ic}$ are material properties, and both can be used for the design process, but $K_{Ic}$ is often used because it gives a more conservative value of design. ASTM standard E399 describes the methods used to calculate the value of $K_{Ic}$, along with the experimental procedures.

The design stress ($\sigma_d$) is related to the $K_{Ic}$ by Equation 2-21. During the design process, the designer has to choose the constraints and the parameters to be controlled by the design.

$$\boldsymbol{\sigma_d = \frac{K_{Ic}}{Y\sqrt{\pi a}}} \qquad \textbf{2-21}$$

The use of LEFM for inspection and lifetime extension calls for the need to observe the crack propagation of the object. According to Paris' law, crack propagation per load cycle is related to the stress intensity factor (ΔK) by Equation 2-22. Where, C and m material parameters. Moreover, the crack depth (a) to length ratio should be less than 1:5; crack growth analysis in two axes is recommended if this condition is not satisfied [31].

$$\boldsymbol{\frac{da}{dN} = C(\Delta K)^m} \qquad \textbf{2-22}$$

The da/dN, which is fatigue crack growth rate, is the slope of crack size vs the number of cycles found from the constant amplitude fatigue tests. For a given crack size, the corresponding stress intensity factor range can be calculated as a function of the stress range from Equation 2-23. The log-log plot of fatigue crack growth rate vs stress intensity factor range is shown in Figure 2-9, which is divided into three regions. Regime-A shows the area with no crack, Regime-B follows the crack growth rate according to the Paris law, and Regime-C shows the unstable region where crack growth rates are extremely high [73]. The fracture toughness parameters $K_c$ and $K_{Ic}$ mainly used for the initial design correspond to Region-3.

$$\boldsymbol{\Delta K = \Delta\sigma Y\sqrt{\pi a}} \qquad \textbf{2-23}$$

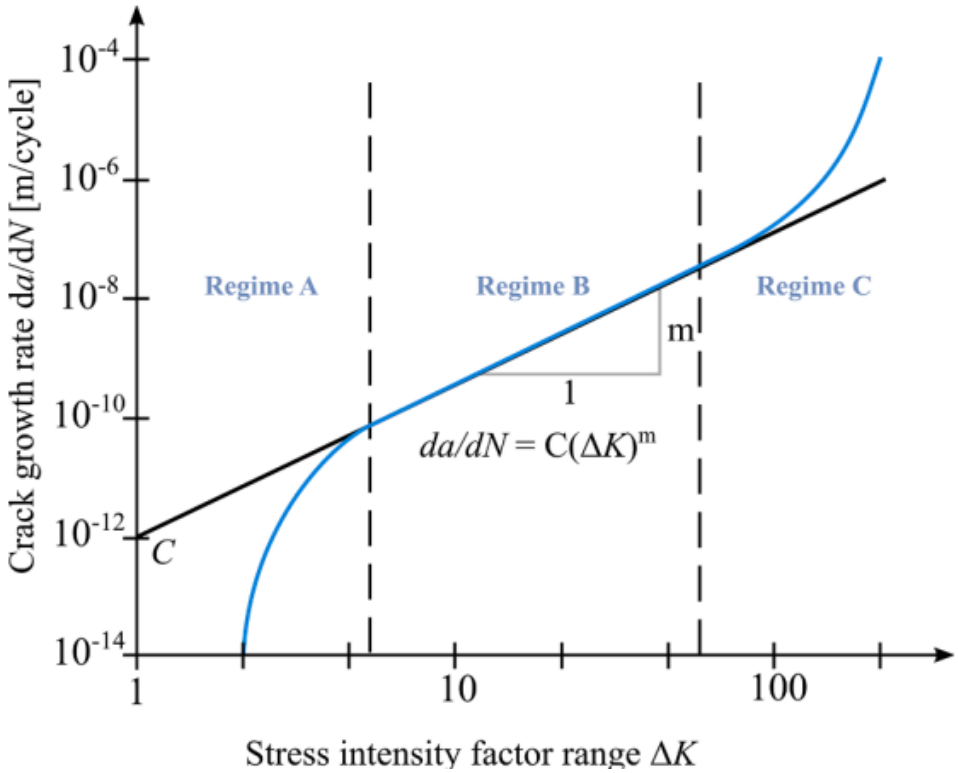



**Figure 2-9: Relation between crack propagation rate and stress intensity factor (Adapted from** [73] **)**

## 2.6 Finite element analysis methods

Soil modelling plays a critical role in analysing OWT support structure due to the complex nature of pile-soil interaction. Different modelling techniques being used for such analysis are discussed below.

### 2.6.1 Standard analysis method (p-y method)

The laterally loaded piles are often modelled with a simplified method known as Beam on Nonlinear Winkler Foundation (BNWF) or a p-y method. The hypothesis is that the soil reaction (p) exerted by the soil at the pile is proportional to the pile deflection (y). This approach is widely used in the offshore oil & gas industry to find pile deformations and stiffness and is given in [56], [74]. The Winkler approach is based on modelling soil-pile interaction as independent springs along the length of the pile. Although this approach has been widely used for the oil & gas industry design, its accuracy is questionable for offshore foundations having a large diameter [75].

The study by Kim et al. [76] has determined that the p-y method overestimates the displacement and bending moment compared to the 3D FE methods. The study also demonstrated how a p-y curve obtained from the 3D FE analysis (instead of existing p-y curves) can improve the accuracy of predicting the behaviour of large-diameter piles. Moreover, Velarde et al. [77] concluded that the API and FE methods show good agreement for shallow depths, but the API method overestimates stiffness with further depth increases. However, the accuracy of the p-y curve has been established for slender bodies like jacket foundations in the design standards and research publications. Asgarian et al. [58] compared the jacket's dynamic response using the soil's 3D and p-y models. The study found a good agreement between the two methods and suggested using the p-y curve method for jacket foundations due to simplicity and lower computational cost.

### 2.6.2 3D design method

The p-y curve method cannot capture the complex nature of soil-pile interaction to efficiently design large-diameter foundations like monopile. Much work has been done to better design monopiles using FE methods. This approach helps capture realistic soil behaviour under cyclic and dynamic loading conditions. Many constitutive models, such as Mohr-Coulomb, Drucker-Prager, or Hardening Soil models, can depict the nonlinear behaviour of soils under varied loading situations. Velarde at al. [77] used the Hardening Soil (HS) model to capture the non-linear and time-varying behaviour of monopile foundation, and Shittu et al. [66] demonstrated the use of soil modelling using the Drucker-Prager model in ANSYS. The HS model used a hyperbolic stress-strain curve, which better captures stiffness variation in sand layers compared to other models.

### 2.6.3 Beam element model

The computational cost of fatigue life estimation is quite high in 3D models due to the fine mesh requirements. The jacket structure's legs, braces, and piles are modelled using beam elements in this approach. These elements are defined as line segments with specific cross-sectional properties along their length. Beam elements can efficiently capture the bending, axial, and shear behaviour of

slender members of the jacket foundation. The mesh size does not affect the accuracy of beam element models, and the definition of nodes at the member's end can accurately capture the member's behaviour. The pile-soil interaction is accurately modelled using the p-y curve method for slender bodies.

Moreover, The joints are modelled as rigid or flexible based on detailed properties like cans and chords. The benefit of using beam elements is the ability to efficiently solve the model dynamics in the time domain, which is critical for fatigue analysis under coupled wind and wave loading. This research uses beam element models to capture the integrated dynamic response of the jacket and iterate designs for improvements. The amount of design modifications analysed in this research would not be possible with 3D design models.

## 2.7 Structure optimisation

With the growing utility of Artificial Intelligence (AI) in technical advancements, designers are turning to AI to create novel designs. A generative design process generates innovative designs that are unknown to designers based on specific constraints and variables, including weight, size, material, and manufacturing method.

Optimisation algorithms comprise computational methods for finding an objective function's maximum or minimum value subject to certain constraints. The specific objectives and corresponding performance metrics in structural optimisation vary depending on the application. However, some common goals include minimizing weight, especially in weight-sensitive industries like aerospace and automotive, where lighter structures can improve efficiency. Maximizing stiffness is often desirable as stiffer structures reduce deflections and enhance overall stability.

Different optimisation algorithms are being used to optimise engineering applications like aerospace, offshore wind, and commercial buildings. Gradient-based algorithms rely on the availability of the objective function's gradient with respect to the design variable to improve the design. Gradient-based algorithms work on the principle of starting with an initial design, calculating the gradient of the objective function at that point, and then updating the design variables in the

direction of the negative gradient (for minimization problems) or the positive gradient (for maximization problems). However, gradient-free algorithms are used when the objective function is discontinuous or a discrete variable.

However, the optimisation of jacket foundation in the literature is dominated by population-based algorithms, mainly called evolutionary algorithms and swarm intelligence algorithms. The most commonly used evolutionary and swarm intelligence algorithms for jacket foundations are Genetic Algorithm (GA) and Particle Swarm Optimisation (PSO), respectively. GA mimics biological evolution, using selection, crossover, and mutation operators on encoded design solutions. Information is exchanged through crossover between solutions. On the other hand, PSO simulates the social behaviour of birds flocking, with particles moving the search space to find the optimal solution.

Regarding randomization, GA applies mutations to maintain diversity and explore the design space. PSO uses random coefficients to vary particle velocities in a stochastic manner. For convergence control, GA uses selection pressure and population diversity parameters. PSO regulates convergence through inertia weight and acceleration coefficients. Moreover, PSO often converges faster as all particles profit from shared information. But GA is more adaptable and better equipped to avoid getting stuck in local optima due to its broader search approach. A modified form of the evolutionary algorithm called bi-directional evolutionary structural optimisation (BESO) is given in [78], where the option of adding material in the overstressed regions is also included. However, both evolutionary and BESO algorithms are criticized because of the ability to often produce non-optimal designs and being able to handle limited constraints [79]–[81].

The use of density-based algorithms is on the rise for offshore jacket foundations because it can avoid the shortcomings of other methods by employing finite element methods. It can include the complex dynamic interaction of different structural components and simulate loads from the aero-hydro-servo-elastic simulations. The basic concept of density-based optimisation is to give each element or grid point in the design domain a material density value. The density

value indicates the amount of material present at a given location. This study uses the Density-based Topology Optimisation (TO) algorithm and will be further discussed in the following section.

### 2.7.1 Structural optimisation of the offshore foundations

As discussed in Section 2.1.3, the offshore jacket foundations' design is inspired by the oil and gas industry, leading to conservative designs and results in the higher costs of offshore wind energy. Currently, efforts are being made to improve the designs of the jacket structure to enhance the structural integrity using different algorithms like gradient-based methods, level-set-based methods, and genetic algorithms. Kaveh et al. [82] used general Colliding Bodies Optimisation (CBO) and enhanced CBO (ECBO) methods to improve the design of OC4 jacket foundations. The jacket was modelled in 2D space with MATLAB, and a weight reduction was achieved by finding the optimal diameter and thickness. A similar study was performed by Häfele et al. [83] using a particle swarm optimisation algorithm and found that the algorithm's efficiency was affected by the number of evaluated functions and load cases. However, the model only generated the designs at the conceptual level, and the structural design validation was not performed.

The use of genetic algorithms to improve the design of offshore structures is discussed by Pasamontes et al. [84]. The study jointly optimised the member thickness, diameters, and locations of the nodes and found that the optimisation can be performed using the discrete values of the design variables from a catalogue. However, the author discovered that while the method produced lighter designs, many designs were not viable due to Stress Concentration Factors (SCFs) that exceeded the validity limits of the SCF calculation procedures. Savsani et al. [85] used teaching-learning-based optimisation (TLBO) and genetic algorithms to optimise the jacket foundation and found that the efficiency of the TLBO algorithm is better than the genetic algorithm. Asgari et al. [86] used a genetic algorithm to optimise the design of the jacket foundation and achieved a 15% reduction in mass. However, their optimised structure exhibited failures at four locations before reaching the intended service life of 20

years. The genetic algorithm was also used to optimise the oil and gas jacket foundation to achieve an 8% weight reduction by Kling et al. [87]. The author liked the automated process and ease of implementation but emphasized the efficient use of mutations and design variables to reduce non-practical designs. Moreover, the parametric structural optimisation of a three-legged and a four-legged jacket was compared by Chew et al. [88], who observed that a three-legged jacket optimisation could save more weight, but the fatigue damages are greater than the reference OC4 jacket foundation.

The use of TO in the offshore industry is relatively new but rising. Research is being done to optimise the offshore structures using the TO method to overcome the incapacity of some algorithms to model the complex nature of integrated aerodynamic and hydrodynamic loads. The jack-up offshore structures used in the oil and gas industry are optimised in [89], [90] by maximizing the structural stiffness of the structure under extreme environmental conditions. The transition piece of a jacket foundation was optimised using TO by Lee et al. [91], and the authors found that the TO model reduced the stresses by 15%. Tian et al. [92] optimised the OC4 jacket foundation and also used shape and size optimisation to determine the size and diameters of the braces. A similar study was performed to optimise the topology of a jacket foundation; however, it was recommended to perform strength and fatigue checks in the future [93]. Lu et al. [94] showed the use of TO to optimise the tripod structure to extend the design life.

### 2.7.2 Topology optimisation algorithm

Topology Optimisation (TO) is a computational method used to generate an optimal distribution of material to achieve lightweight structures without compromising on structural integrity. TO can improve existing or AI-generated designs by removing materials and generating an optimum load path under the specified constraints. The result is a lighter structure with similar structural integrity but a reduced mass and hence the cost.

The application of TO in structural optimisation has been extensively reviewed in [95]–[98]. The work by Meng et al. [99] involved a review of TO methods and their application in additive manufacturing techniques. The researchers highlighted the

trade-off between the ease of manufacturing and the unity of components in multi-functional products. Various literature studies show the growing use of TO and additive manufacturing in Aerospace [100], [101], and the automotive industry [102]. TO is assisting in developing revolutionary aviation wings, fuselages, and engine components, and new suspension systems and chassis designs are being developed in the automation industry. Moreover, the use of TO in optimising geometrically complex and aesthetically pleasing high-rise buildings is studied in [103], [104]. TO is increasingly used in biomedical engineering as new implants and prostheses are being developed and 3D printed [105].

Jacket structures are designed according to oil and gas industry practices and tend to be very conservative with high safety factors [106]. Excessive steel weights and high capital costs can result from using non-optimised jacket designs for OWTs. However, tailored jacket designs optimised for these turbines can substantially save weight and cost. Topology optimisation is a promising technique to explore novel, efficient jacket configurations specific to offshore wind requirements. This approach is particularly useful when a structure faces multiple complex loads, like in the case of offshore wind turbines. Mathematically, a TO problem can be written by Equation 2-24.

$$\min_{y} c(y) = M^T J M = \sum_{i=1}^{m} (y_e)^p V_i^T k_i v_i \qquad \textbf{2-24}$$

$$\textit{Subject to}: \begin{cases} \dfrac{G_y}{G_0} = R \\ JM = F \\ 0 < z_{min} < z_j < 1 \end{cases}$$

Where J and M show the global displacement matrix and stiffness matrix, respectively, y represents the design variables, $z_{min}$ is the minimum relative density vector, F shows the overall stiffness matrix, p is the penalty factor, $G_o$, and $G_y$ represent the design area volume and overall material volume respectively, N represents the number of finite elements in the design area, and R is specified volume ratio [89].

The most common algorithm for TO is solid isotropic material with penalization (SIMP), where an optimal density is found for each element inside a design space [107], [108]. The conventional optimisation methods result in the continuous variation of the density; however, the SIMP method forces the density near 0 or 1 by removing intermediate values with the help of a penalization method [109].

Level set-based optimisation is another approach S. Osher and J. Sethian developed for determining the structure's local minimal compliance. The focus of this method is to improve the shape and interface of the structure. This method is particularly useful where the structure may have holes, or the profile is split into several components. One drawback of this method is that volume conservation is not always achieved, resulting in a distorted shape [110]. Compared to this method, SIMP results in manufacturable designs and has clear material boundaries [110], [111]. A mixable density algorithm combines the traits from the SIMP and level-set-based methods, but the SIMP method is often preferred due to the improved accuracy and reduced computational cost.

# 3 Evaluation of Wind Resources and Windfarm Income

This chapter presents a comprehensive analysis of the performance of a wind farm, utilizing the wind turbine power measurement standard IEC61400-12-1 [53]. By acquiring ten-minute averaged wind data from a Windcube v2 LIDAR over twelve months, the wind resource at the wind farm is analysed and compared with ten years' worth of data from a weather station. This comparison enables a detailed assessment of the wind resource availability and its variability at the wind farm. The performance of one of the wind turbines located in the wind farm is also evaluated by comparing the wind power potential of the wind turbine with its actual power production. The annual energy production and power curve were established for one Vestas V-27 turbine. The impact of electricity spot pricing and green certificate prices on monthly revenue generation was also evaluated, finding that market factors have a greater influence than underlying wind resources.

The detailed wind resource assessment and turbine performance evaluation conducted in this study of an onshore wind farm provides a model for how similar analyses could be applied to offshore wind farms. In particular, the use of LIDAR to collect high-resolution wind data at hub height would be critical for offshore sites, where installing fixed meteorological masts is more challenging. The data collected on wind speeds, turbulence intensity, and dominant wind directions could then feed into load calculations to determine environmental loads experienced by offshore wind turbines. A similar approach could be taken with wave buoys equipped with LIDAR to measure wave statistics like significant wave height and peak wave period to obtain wave loads for fatigue life estimation. The 12 months of wave data from the LIDAR buoys could then be correlated with long-term hindcast datasets from wave models to establish a statistical relationship. This is analogous to correlating the 12 months of LIDAR wind data with long-term meteorological data. The correlation could synthesise long-term wave climate

---

A version of this chapter has been published as: Marjan A, Shafiee M. Evaluation of Wind Resources and the Effect of Market Price Components on Wind-Farm Income: A Case Study of Ørland in Norway. Energies. 2018; 11(11):2955

data by applying the derived relationship to the historical wave model hindcast time series. A similar approach is used in this study to extend the 12 months of wind data to 38 years.

Moreover, this would provide statistically robust long-term wave climate data, including parameters like wave height, period, and directional spreading. The long-term data would capture seasonal and inter-annual variability. Uncertainty analysis similar to that presented in the paper could also be applied to quantify confidence intervals in the long-term wave estimates. The long-term wind and wave climate data could then be used as input for DLCs (see Section 2.4.2) to calculate the fatigue life of offshore foundations.

## 3.1 Introduction

Wind power density is a crucial evaluation parameter that indicates the wind energy potential at a specific location. Additionally, considering the wind direction is vital in determining the optimal positioning of wind turbines within a wind farm to maximize power production. Light Detection and Ranging (LIDAR) is extensively used for wind turbines' accurate site analysis and performance testing [112]. The obvious benefits of using LIDAR over traditional met-mast are the ease of installation, higher resolution, and longer range [113]. Moreover, the use of the power performance measurement standard IEC61400-12-1 ensures consistency and accuracy in measurements and analysis of the power performance of the wind farm. An analysis of the wind resources of a small wind farm consisting of 3 wind turbines in Norway is performed using the standard IEC61400-12-1.

Given that a few months of data may not accurately represent the true potential of a site, the long-term potential is estimated using the MCP (Measurement Correlate Predict) method. Subsequently, the power potential of a wind turbine is compared to its actual power production to assess the turbine's performance. This study presents a novel approach by acquiring real wind data by deploying a LIDAR directly within the wind farm, instead of relying on weather station data, to predict wind resources accurately. This innovative methodology allows for a more precise assessment of the wind conditions specific to the wind farm location, leading to improved predictions of available wind resources and enhancing the reliability of the study's findings.

## 3.2 Site description

Ørland is located in Sør-Trøndelag county, Norway, having the administrative centre in Brekstad city. It is located at the northern shore of Trondheimsfjord, which further meets the Atlantic Ocean. Most of the terrain is normally flat, uniform, and unique from the rest of Norway in the way that only 2% of the municipality exceeds the height of 160 m above sea level. It consists of wide-open spaces that are mainly used for agriculture and the main air base of Norway having coordinates (63.7045N, 9.6105E). There is also an official weather station

of Meteorologisk institutt, which has been providing weather observation since 1957.

The wind farm site selected for this study is located around 2 km away from the weather mast (see Figure 3-1). It consists of three Vestas V-27 wind turbines. The top view of these wind turbines is shown in Figure 3-2. On the site, there is a LIDAR system having exact coordinates of (63.70173N, 9.653E). The distance of LIDAR from the middle wind turbine is almost 112m, and the direction is 180. The LIDAR is placed behind the hut, as shown in Figure 3-3.

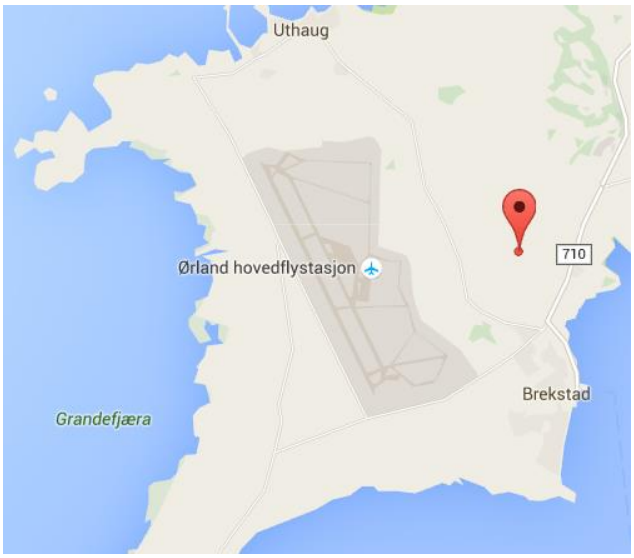



**Figure 3-1: Wind farm's location**



**Figure 3-2: Wind farm's view**

The Vestas V-27 is a type of wind turbine that operates with an upwind configuration, utilizing pitch regulation. It features a horizontal axis design with active yaw control and is equipped with a three-blade rotor. The rotor blades are constructed using glass fibre-reinforced polyester and are composed of two blade shells that are bonded to the supporting beam. Two-stage gearboxes facilitate power transmission to the generator. The wind turbine generator can be adapted to operate in either eight or six poles configurations to maximize efficiency across a range of wind speeds. Depending on the chosen generator (generator-1 or generator-2), the rotor rotates at different rotational speeds to achieve maximum efficiency. The braking mechanism of the wind turbine utilises full feathering, while hydraulic disk brakes are employed for emergency stops, which are fitted with the high-speed shaft of the gearbox. Adjusting the blade position is carried out using the hydraulic system. A microprocessor-based control unit facilitates monitoring and controlling the wind turbine's functions. Yawing, the movement of the turbine to face the wind, is achieved through two wheel-mounted yaw motors located at the top of the turbine tower. The nacelle, which houses the internal components, is enclosed within a cover made of glass fibre reinforcement. Access to the nacelle is provided through a central opening. The detailed specifications are given in [114].

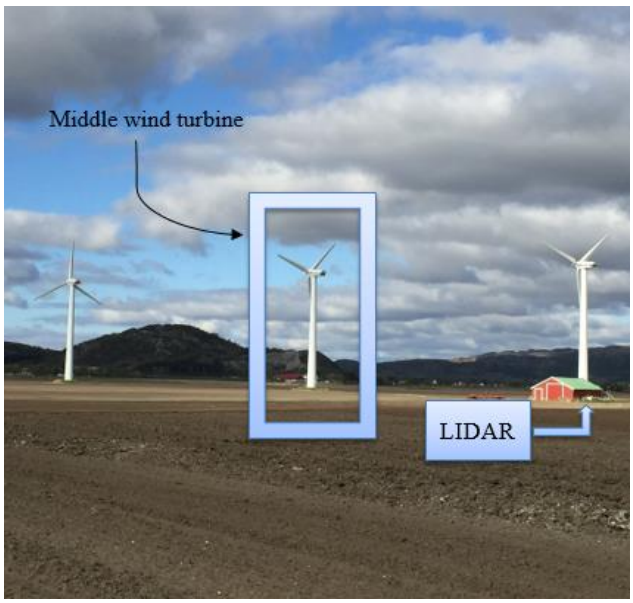



**Figure 3-3: Location of LIDAR and middle wind turbine**

## 3.3 Wind resource analysis

### 3.3.1 Theory

A wind resource analysis is the most important step for measuring the power potential of any wind farm site. There are many ways to model wind speed over time, but the most widely used one is the probability density function (PDF). The Rayleigh and Weibull PDFs are the most used for wind resource analysis. The Weibull distribution is more versatile and useful for modelling data because it uses two parameters: scale and shape. The wind resource analysis is analysed using Weibull distribution in this study because it can provide a better approximation using the two parameters [115]. The general form of Weibull distribution is given in Equation 3-1

$$f(u) = \left(\frac{k}{o}\right)\left(\frac{u}{o}\right)^{k-1} e^{-\left(\frac{u}{o}\right)^{k}} \qquad \textbf{3-1}$$

Where, $f(u)$ is the probability of observing the wind speed *u*, and *k* and *o* represent the scale and shape parameters of the Weibull PDF, respectively. For estimating parameters k and o, various methods are available. However, the

maximum likelihood (ML) method is selected in Windographer software for this study, due to its consistent approach to dealing with diverse parameter estimation problems. The ML estimators of parameters *k* and *o* are represented by Equations 3-2 and 3-3, respectively. Where $u_i$ represents the observation i from the sample and N is the number of samples.

$$\boldsymbol{k} = \left[\frac{\sum_i^N \boldsymbol{u}_i^{\boldsymbol{k}} \ln(\boldsymbol{u}_i)}{\sum_i^N \boldsymbol{u}_i^{\boldsymbol{k}}} - \frac{\sum_i^N \boldsymbol{u}_i}{\boldsymbol{N}}\right]^{-1} \quad \textbf{3-2}$$

$$\mathbf{o} = \left[\frac{\sum_i^N \boldsymbol{u}_i^{\boldsymbol{k}}}{\boldsymbol{N}}\right]^{1/k} \quad \textbf{3-3}$$

### 3.3.2 Results

The wind data was extracted from the Windcube v2, which collects the measurements at different heights up to 200m. The hub height of Vestas V-27 is 31.5m; hence, the wind data was extrapolated at 31.5m for the analysis.

#### 3.3.2.1 Wind speed frequency

The frequency distribution of wind speeds at the hub height is given in Figure 3-4. The wind speeds are categorized into bins of 0.5 m/s width. The wind speed frequency at the wind farm site being analysed follows the Weibull distribution with the parameters *k* = 1.84 and *o* = 7.46 m/s. The low values of *k* imply that the wind speed is not steady and varies to different ranges of values, while the value of *o* shows the average wind speed at the site.

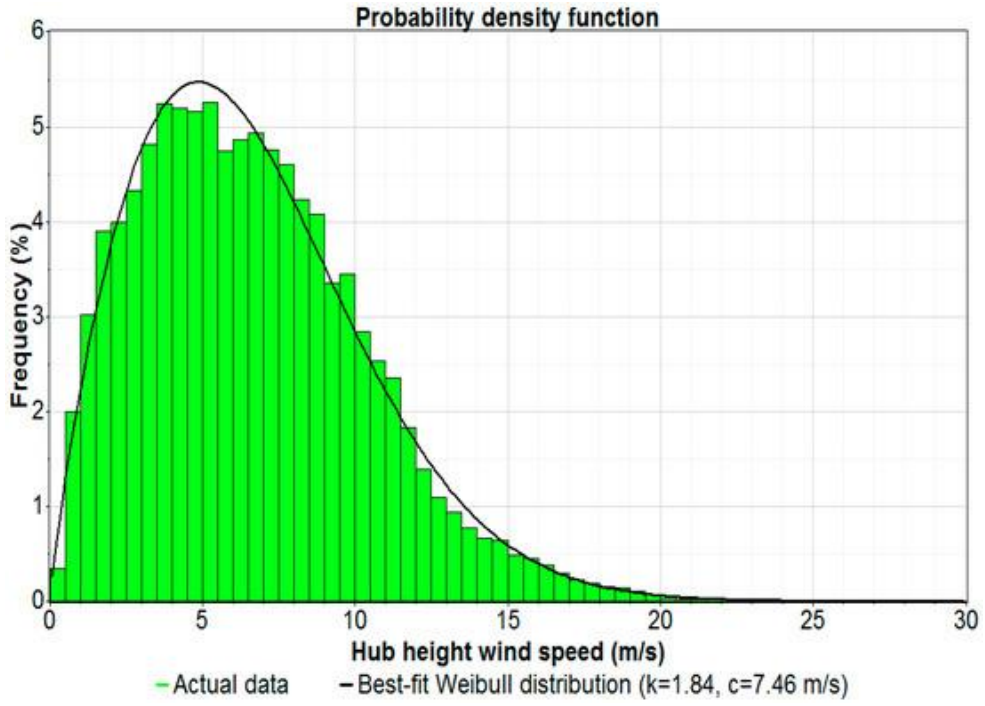



**Figure 3-4: Hub-height wind speed frequency for 12 months.**

### 3.3.2.2 Wind direction

The wind rose is a graphical tool used to understand the wind direction at any location. It displays the frequency with which wind direction falls in a certain direction sector. The frequency with which the wind blows from a certain direction is shown in Figure 6. As shown, most wind blows from the southeast direction (40%), whereas only 21% of the wind blows from the southwest. The power produced by the wind coming from the north is lesser. The blue line shows the position of wind turbines in the wind farm. Wind turbines are positioned straight and make a $173^0$ angle with the north.

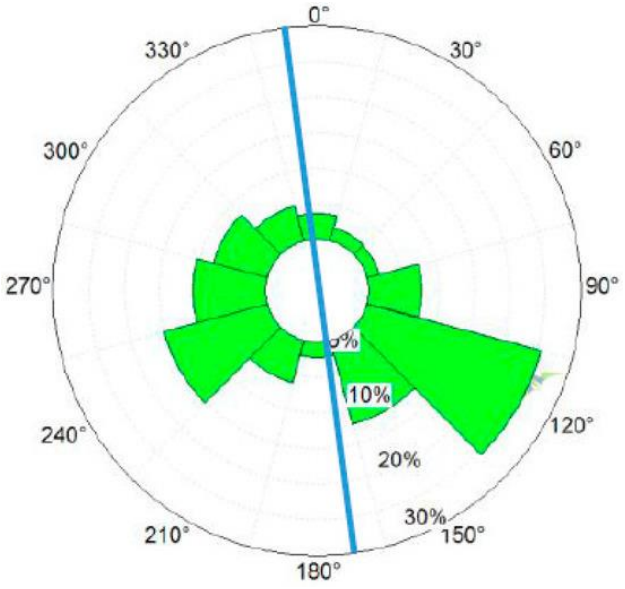



**Figure 3-5: Frequency wind rose of 12 months**

The detailed analysis with different speed bins from each direction sector is shown in Figure 3-6. The bin size of 6 m/s is used with a sector length of 300. The slower wind speed (0-6 m/s) comes from all directions, and the medium wind speed (6-12 m/s), as shown with the green colour, blows from the south and west directions. Moreover, the major portion of strong wind (12-24 m/s) shown with yellow and orange colours in the figure blows from the southeast and southwest direction throughout the year.

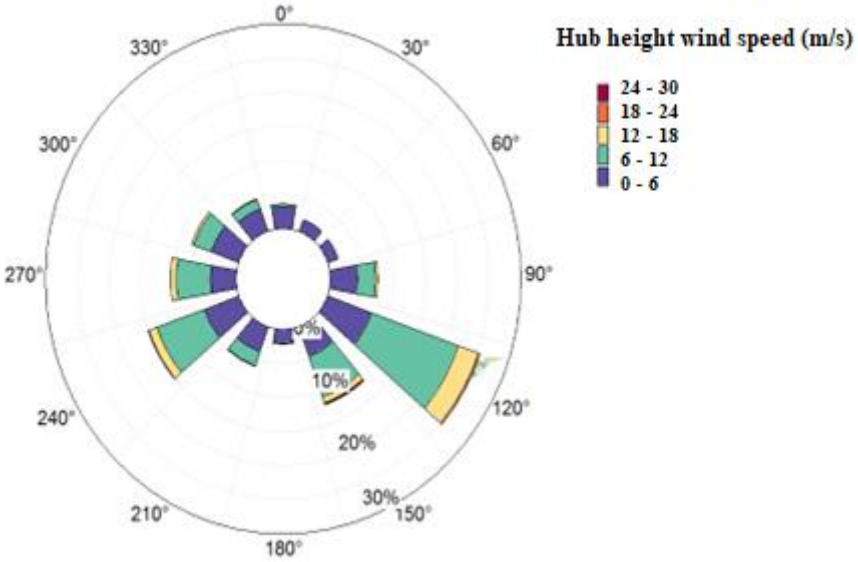



**Figure 3-6: Wind rose with the method of bins**

### 3.3.2.3 Monthly Wind speed

The 10-minute averaged data from LIDAR was analysed to obtain the mean monthly wind speed profile of the wind farm from May 2015 until April 2016. As observed from Figure 3-7, the average wind speed was higher in the winter months and reached its maximum level in December (9.70 m/s). However, the summer months had lighter wind; hence, lower power output was obtained, with the lowest value in July (4.27 m/s). It can further be observed that the wind speed started increasing after July and decreased after reaching its peak in December.

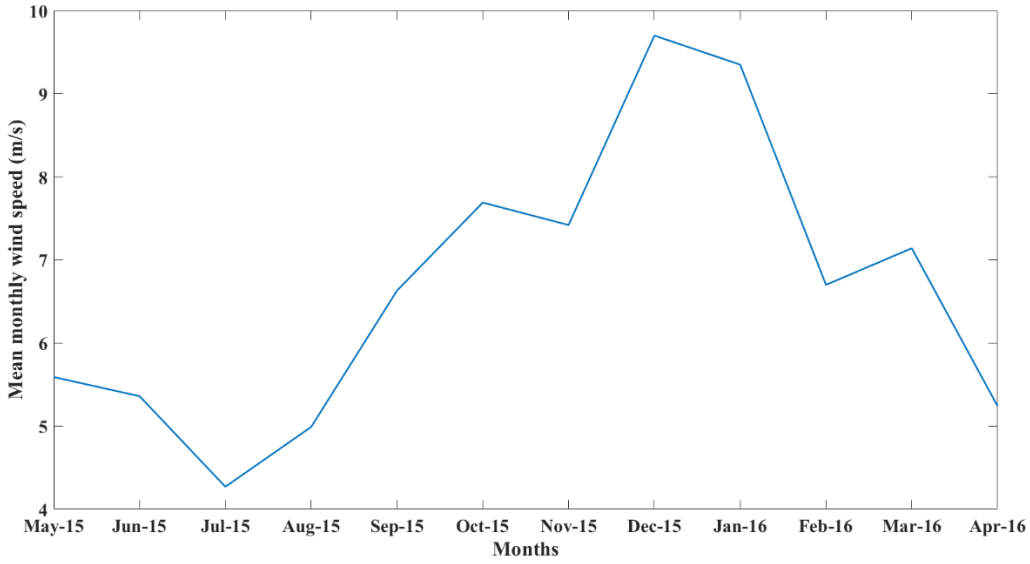



**Figure 3-7: Mean monthly wind speed**

### 3.3.2.4 Wind power class

The wind power class is defined as a number showing the energy content at any location. It depends on the mean wind power density at a 50 m height above the ground. Usually, class 3 and above are considered appropriate for wind power production (see Table 3-1).

**Table 3-1: Wind power class** [116]

| Wind Power Class | Wind Power Density (W/m$^2$) |
|---|---|
| 1 | 0–200 |
| 2 | 200–300 |

| | |
|---|---|
| 3 | 300–400 |
| 4 | 400–500 |
| 5 | 500–600 |
| 6 | 600–800 |
| 7 | 800–2000 |

The monthly wind power density (WPD) and Wind Power Class (WPC) of the wind farm under consideration are given in Table 3-2. It is observed that the wind farm is suitable for wind power production, apart from the months of April, June, July, and August when the WPC is less than 3. However, other months are rated as good for power production. WPC of 7 was obtained in December and January, which is rated as ‘superb’. Since the WPD varies in the vertical direction, the Linear Least Squares (LLS) regression can obtain the straight line that best fits the natural logarithmic variation of mean wind speed with a natural logarithmic height variation. To get the best estimate of WPD for the whole year, Windographer [117] computes the mean power density at which the best-fit line crosses 50 m height. As shown in Figure 3-8, the mean WPD at 50 m was 479 $W/m^2$, which is wind power class 4. From Table 3-1, the wind farm falls under ‘good’ and is close to the ‘excellent’ class for wind power production.

**Table 3-2: Monthly wind power class**

| Month | Average wind speed (m/s) | Wind Power density at 50m (W/m²) | Wind power class |
|---|---|---|---|
| Jun-15 | 5.36 | 257.5 | 2 |
| Jul-15 | 4.27 | 126.2 | 1 |
| Aug-15 | 4.99 | 225 | 2 |
| Sep-15 | 6.63 | 442 | 4 |
| Oct-15 | 7.69 | 622.3 | 6 |
| Nov-15 | 7.42 | 577.4 | 5 |
| Dec-15 | 9.7 | 1147.6 | 7 |
| Jan-16 | 9.35 | 1004.6 | 7 |
| Feb-16 | 6.7 | 429.5 | 4 |
| Mar-16 | 7.14 | 453.5 | 4 |
| Apr-16 | 5.24 | 269.6 | 2 |

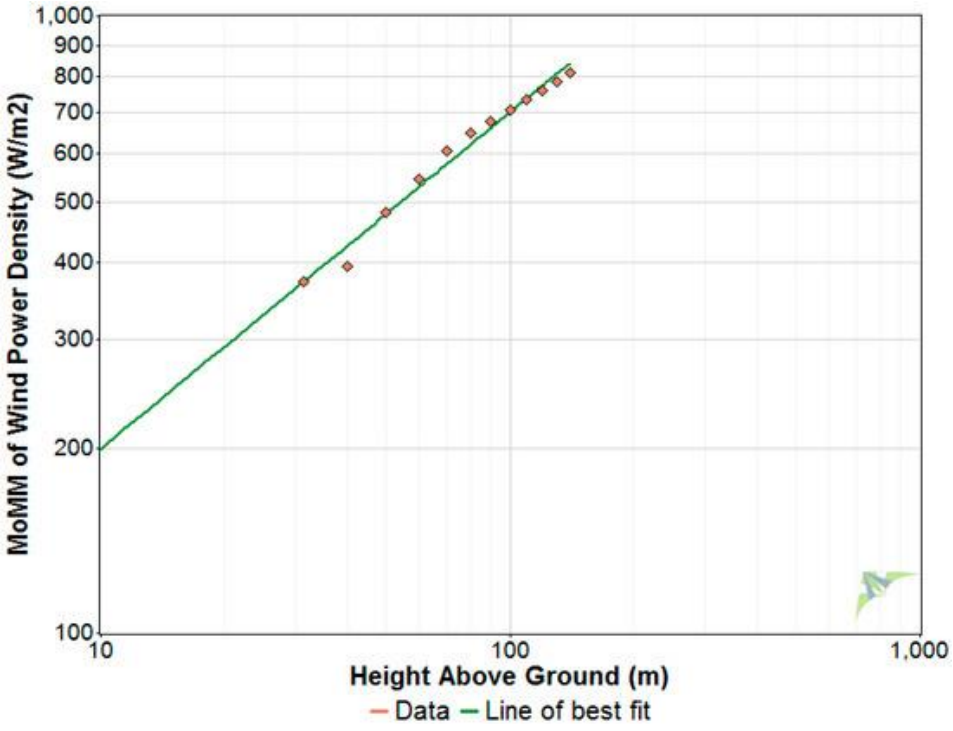



**Figure 3-8: Mean of monthly means of WPD vs. height**

### 3.3.2.5 Long-term analysis

Thus far, the wind resource analysis of a 12-month period was performed; however, to achieve a long-term analysis of the wind farm, there is a need to compare on-site data with the metrological station data. In this study, the Measure-Correlate-Predict (MCP) method is used to evaluate the relationship between the wind data of the target site (wind farm) and the nearby reference station (metrological station having coordinates 63.5 N, 9.375 E).

The MCP feature of Windographer lets the users analyse the relationship between wind speed and direction data measured concurrently at the target location and a reference location. The data from both stations should have some overlap in time because the Windographer analyses the correlation in concurrent data. Based on the relationship between the target and reference location, the Windographer applies the correlation to synthesize target data (wind speed and wind direction) in time steps that contain reference data but no target data [118]. Moreover, both the target and reference data should have the same time step. Windographer averages or subdivides time steps as needed to generate processed data with the time step of choice. This enables users to have the same target and reference processed data time steps, and their time steps perfectly align with each other.

In our case, the 12-month target data is compared with the 38-year reference data having 12 months of concurrent period. The Windographer converted the target data with a resolution of 10-min to 60-min data and then compared it with the 60-min data of the reference station (Table 3-3); hence, the number of time steps of speeds and direction was reduced after processing the data.

**Table 3-3: Properties of (a) target data and (b) reference data.**

| **(a)** | | |
|---|---|---|
| **Property** | **Original** | **Processed** |
| Start time | 8 May 2015 | 8 May 2015, 00:00 |
| End time | 9 May 2016 | 9 May 2016, 01:00 |

| | | |
|---|---|---|
| Duration | 12 months | 12 months |
| Time step size | 10 min | 60 min |
| No. of Time steps–speed | 51,027 | 8576 |
| No. of Time steps–direction | 50,354 | 8487 |
| **(b)** | | |
| **Property** | **Original** | **Processed** |
| Start time | 1 January 1980 | 1 January 1980 |
| End time | 1 July 2018 | 1 July 2018 |
| Duration | 12 months | 12 months |
| Time step size | 60 min | 60 min |
| No. of Time steps—speed | 337,464 | 337,464 |
| No. of Time steps—direction | 337,464 | 337,464 |

Figure 3-9 depicts the correlation between the target and reference wind speeds for all the directions using Linear Least Squares regression (LLS) [119]. The correlation value between the target and reference data is 0.527, which can be classified as a ‘moderate correlation’ according to the rule of thumb stated in [120]. This long-term wind farm data is predicted based on the reference data (as explained above), shown in Figure 3-10. It can be established that winter is windier than summer, while December and January have the highest wind speeds. The wind direction based on 38 years of data shows that the majority of the wind blows from southeast and southwest directions (Figure 3-11).

Table 3-4 compares the target and final predicted data, where final predicted data refers to the long-term predicted data of the wind farm. It can be observed that the long-term mean predicted wind speed of the wind farm is 6.705 m/s, which is about 1% greater than the original mean wind speed. The multi-annual variation of predicted mean wind speed at the wind farm is shown in Figure 3-12, where

LLS shows the results after the Least Squares Regression has been performed. The annual mean wind speed of the wind farm varies from 6 m/s to 7.4 m/s.

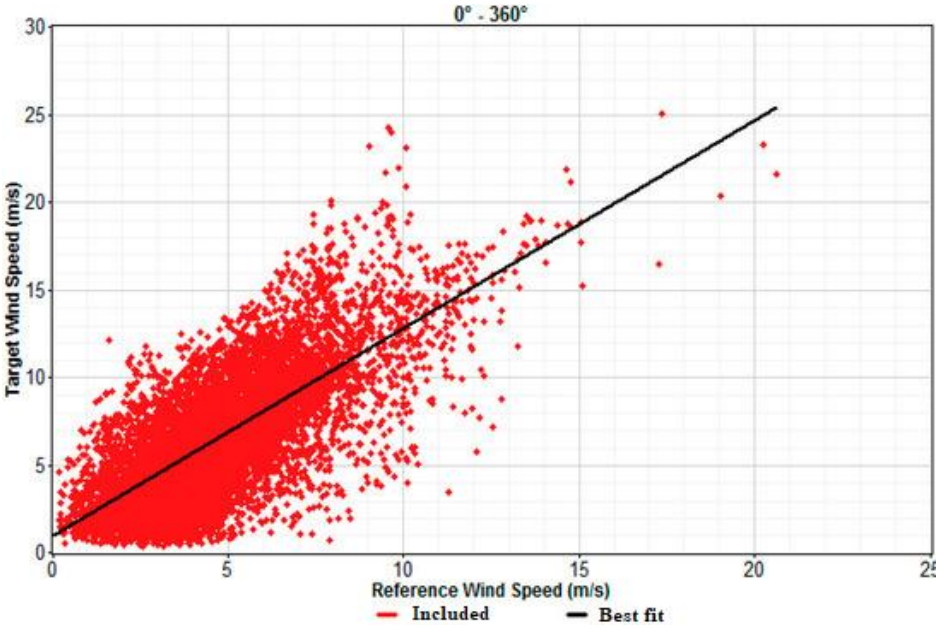



**Figure 3-9: Correlation between the target and reference wind speeds**

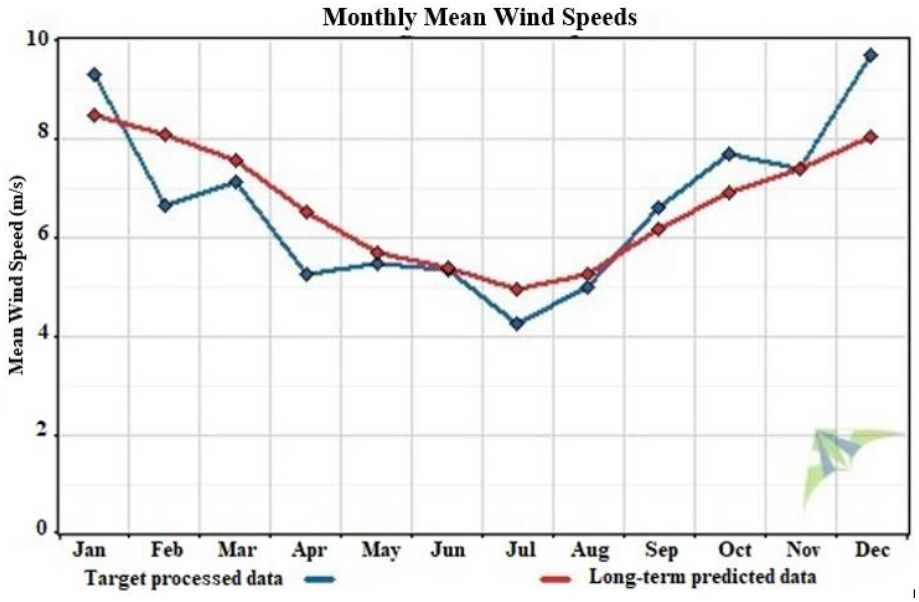



**Figure 3-10: Comparison of the wind farm's monthly mean wind speeds and the long-term predicted wind speeds**

**Table 3-4: Comparison of the target and long-term predicted data**

| Property | Target Original | Target Processed | Long-Term Predicted |
|---|---|---|---|
| Start time | 8 May 2015 | 8 May 2015 | 1 January 1980 |
| End time | 9 May 2016 | 9 May 2016 | 1 July 2018 |
| Duration | 12 months | 12 months | 38 years |
| Time-step size | 10 min | 60 min | 60 min |
| No. of time-steps—speed | 51,027 | 8576 | 337,463 |
| No. of time-steps—direction | 50,354 | 8487 | 337,463 |
| Mean speed at hub height | 6.641 m/s | 6.633 m/s | 6.71 m/s |
| MoMM speed at hub height | 6.642 m/s | 6.635 m/s | 6.702 m/s |
| Min. speed at hub height | 0.12 m/s | 0.36 m/s | 0.36 m/s |
| Max. speed at hub height | 27.19 m/s | 25.09 m/s | 30.80 m/s |
| Weibull k at hub height | 1.85 | 1.91 | 2.43 |

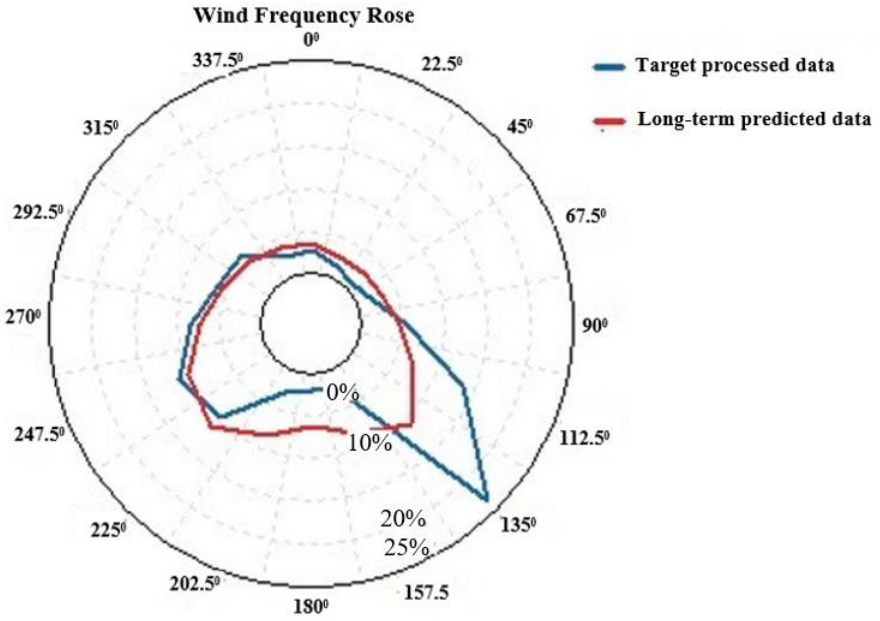



**Figure 3-11: Long-term predicted wind direction**

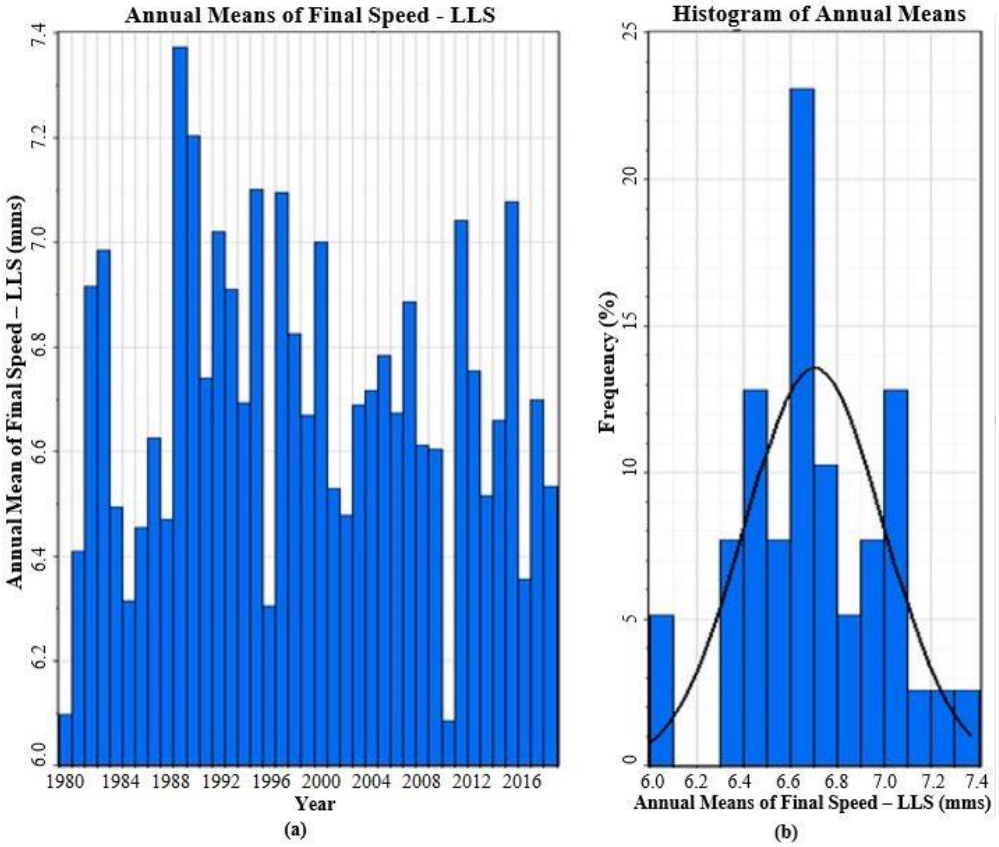



**Figure 3-12: Multi-annual predicted wind speed of the wind farm: (a) Annual mean wind speed of 38 years; (b) Histogram of annual means**

## 3.4 Power performance

### 3.4.1 Theory

The power available in the wind is computed by the 'method of bins' based on the IEC61400-12-1 standard. The theoretical maximum efficiency of the wind turbine is 59% (Betz limit). However, 30–45% efficiency is achieved even for the best-designed wind turbines when the losses due to gearbox, generator, bearings, and wake effects are considered. Power available in the wind can be calculated by equation 3-4.

$$\boldsymbol{P_{avail} = \frac{1}{2}\rho A V^3 C_p} \qquad \textbf{3-4}$$

$V$ is the velocity, $A$ is the swept area, $\rho$ is the standard air density, $C_P$ is the power coefficient, and $P_{avail}$ is the power available in the wind. The power data is acquired by applying the "method of bins" with the bin size of 0.5 m/s, and by calculating the power output, power coefficient, and the mean values of normalized wind speed in each bin using the equations below.

$$\boldsymbol{V_i = \frac{1}{N_i}\sum_{j-1}^{N_i} V_{n.i.j}} \qquad \textbf{3-5}$$

$$\boldsymbol{P_i = \frac{1}{N_i}\sum_{j-1}^{N_i} P_{n.i.j}} \qquad \textbf{3-6}$$

$$\boldsymbol{C_{P,i} = \frac{P_i}{\frac{1}{2}\rho A V_i^3}} \qquad \textbf{3-7}$$

Where $V_i$ is the normalized/averaged wind speed in bin i, $V_{n,i,j}$ is the normalized wind speed of data set j in bin i, and $P_i$ is the normalized/averaged power output in bin i, $P_{n,i,j}$ is the normalized power output of data set j in bin i. $N_i$ is the number of ten-minute data sets in bin i. $C_{P,i}$ is the power coefficient in each bin.

### 3.4.2 Methodology

The wind data from the LIDAR was acquired for 12 months, and the Windographer estimated the power available in the wind. The actual monthly power produced by the middle wind turbine was noticed for 12 months. Due to

the unavailability of power data from other wind turbines, the focus was set on the middle wind turbine, and all the results and comparisons presented in this study are based on the middle wind turbine.

### 3.4.3 Results

#### 3.4.3.1 Mean power and energy output

Gross mean power and energy data are based on the power available in the wind, which wind turbine V-27 should ideally produce based on the power curve data given by the manufacturer in [114]. However, the actual mean power and energy data indicate the real power and energy the wind turbine produces at the site.

The monthly variation of the mean power output is shown in Figure 3-13. The monthly mean power output of the wind farm. It can be observed that higher average wind speed results in higher power output during the winter, where maximum power of 101.01 kW and 100.24 kW is produced in December and January, respectively. These two months contribute 30% of the annual power production. However, the summer months are not ideal for power production, and the lowest power produced is 17.92 kW (July).

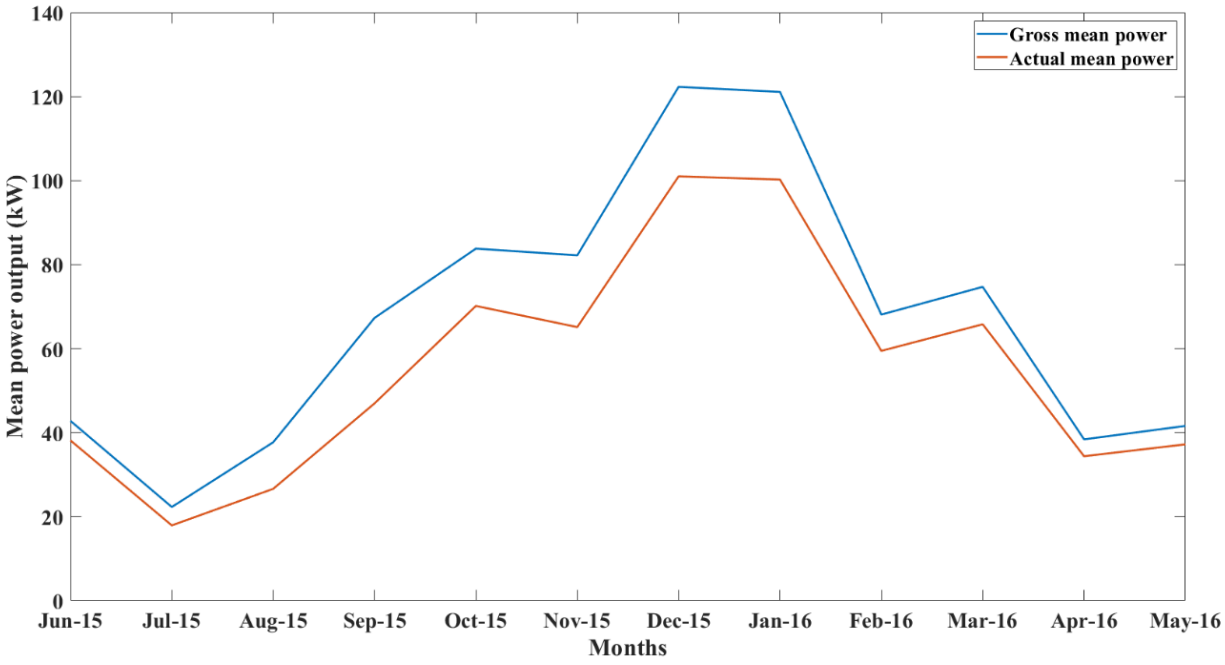



**Figure 3-13: The monthly mean power output of the wind farm**

Figure 3-14 depicts the monthly variation of the capacity factor of the wind farm. The capacity factor of a wind turbine is defined as the actual power produced by a wind turbine compared to the maximum possible power output during that time. The mean monthly power output was compared with the maximum possible power of the wind turbine to obtain monthly capacity factors. It can be observed that the capacity factor is higher in the winter months and reaches the maximum value of around 45% in December and January, while the value is much lower during the summer. The actual capacity factor of the wind turbine over the year is 24.55%, while the gross capacity factor estimated by Windographer based on the wind resource for V-27 is 29.95%. It can be concluded from this observation that the overall losses of the wind turbine are around 18%. These losses combine wake effects, bearing, availability, and generator losses. The overall capacity factor of 24.55% for the wind turbine is a good number in the European context because the average capacity factors in Europe, Germany, UK, Netherlands, and France from 2003–2007 were 20.1%, 29.3%, 25.9%, 25.7% and 21.8%, respectively [121]

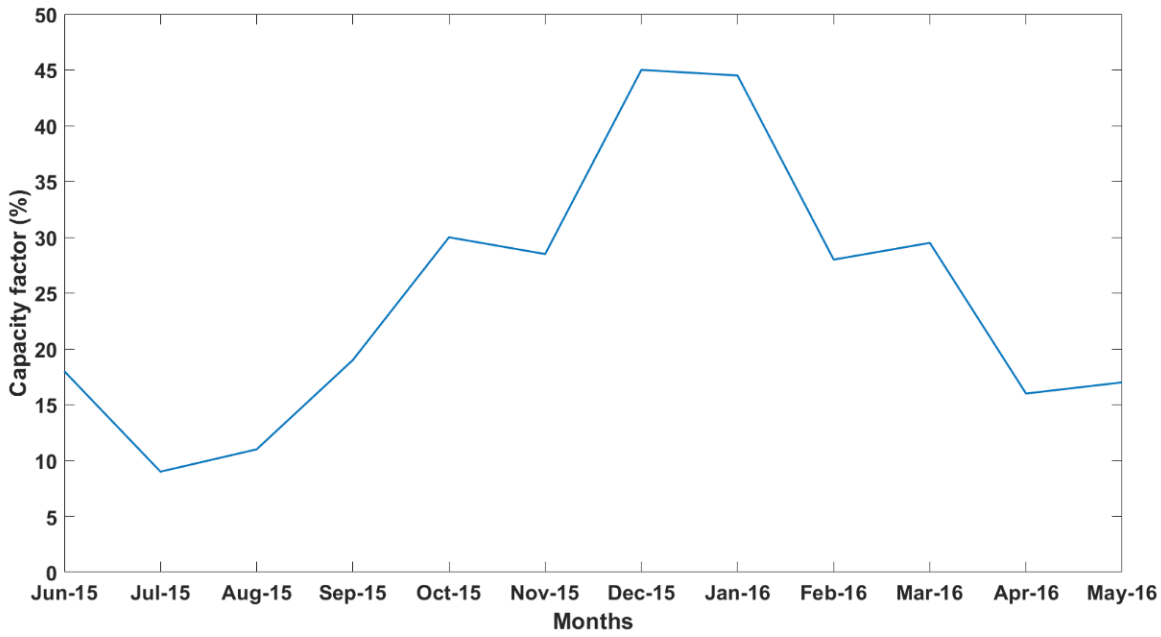



**Figure 3-14: The monthly capacity factor of the wind farm**

### 3.4.3.2 Power curve

The performance of a wind turbine is generalized by its power curve. The power output of the middle wind turbine was observed for two months. The wind turbine's wind speed and power data are used to obtain the scatter plot. The best-fit curve on the data points was plotted using polynomial curve fitting in MATLAB. The polynomials of various orders were tested to fine-tune the coefficients to the data points. The polynomial curve fit of the 8th order is plotted in Figure 3-15. As can be seen, a good fit with the data was found.

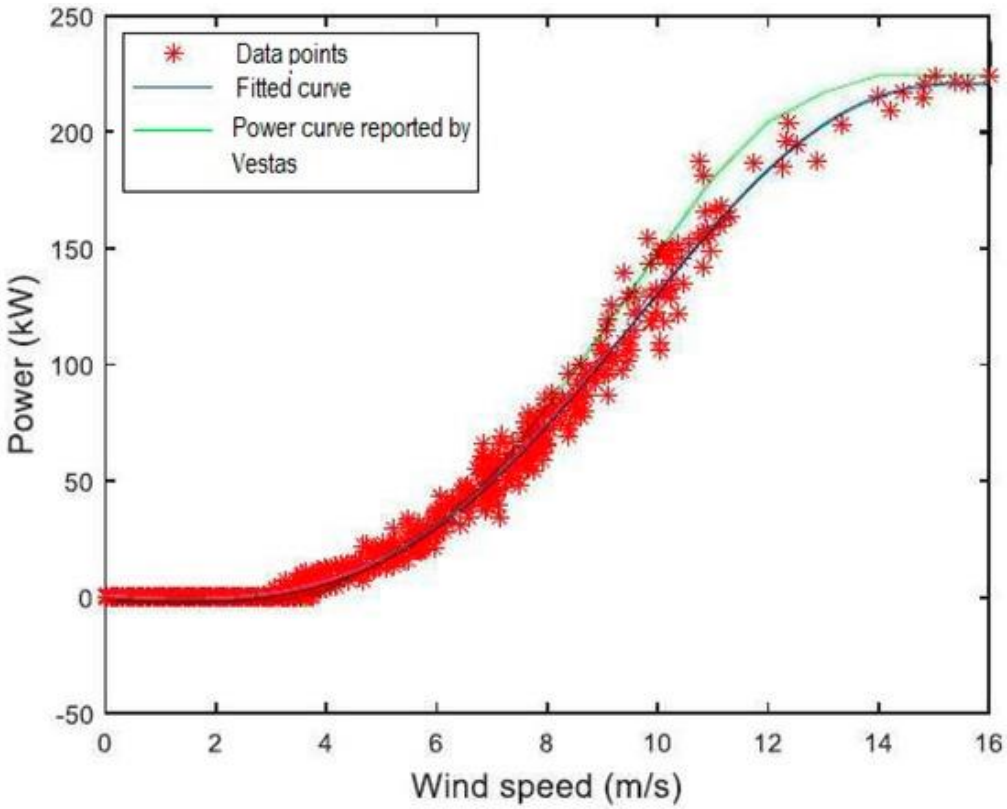



**Figure 3-15: Power curve with the scatter plot**

Moreover, Figure 3-15 compares the power curve of the wind turbine V-27 at the wind farm obtained with a best-fit curve and the power curve reported by the manufacturer. It is observed that the power curve of V-27 matches almost precisely with the manufacturer's power curve up to the wind speed of 7 m/s. However, the gap widens and reaches its maximum level (nearly 16%) at 11.80 m/s. This deviation is caused by the losses and the unavailability of enough data above the wind speed of 10 m/s.

## 3.5 Revenue estimation

The Energy Act, which manages the production, conversion, transmission, trading, distribution, and energy use in Norway, follows market-based power trading. Norway is embodied in the joint Nordic Power market along with Sweden, Finland, and Baltic countries, where most of the generated power is traded on Nord Pool spot power exchange based on market demand [122]. To achieve the country's goals under the EU's Renewable Energy Directive, Norway and Sweden established a joint Norwegian-Swedish tradable green certificate (TGC) in 2012 [123]. The financing of TGCs is carried out by consumers, with renewable energy producers possessing the ability to sell each certificate. In contrast to feed-in tariffs, TGC prices, along with electricity prices, tend to be higher during winter and lower during summer. This implies that TGC prices also fluctuate based on the principles of supply and demand.

The income generated by the wind farm is estimated by considering the average monthly spot prices of electricity traded on the Nord Pool power exchange, along with the average monthly prices of TGCs. The figures are based on the actual monthly mean energy output of the middle wind turbine, and it is assumed that the output of the other two wind turbines is equal to the middle wind turbine. The monthly income stream of the wind farm based on the monthly average TGC price and electricity price is given in Figure 3-16. The average monthly electricity and TGC prices are given in Figure A-1 and Figure A-2, respectively.

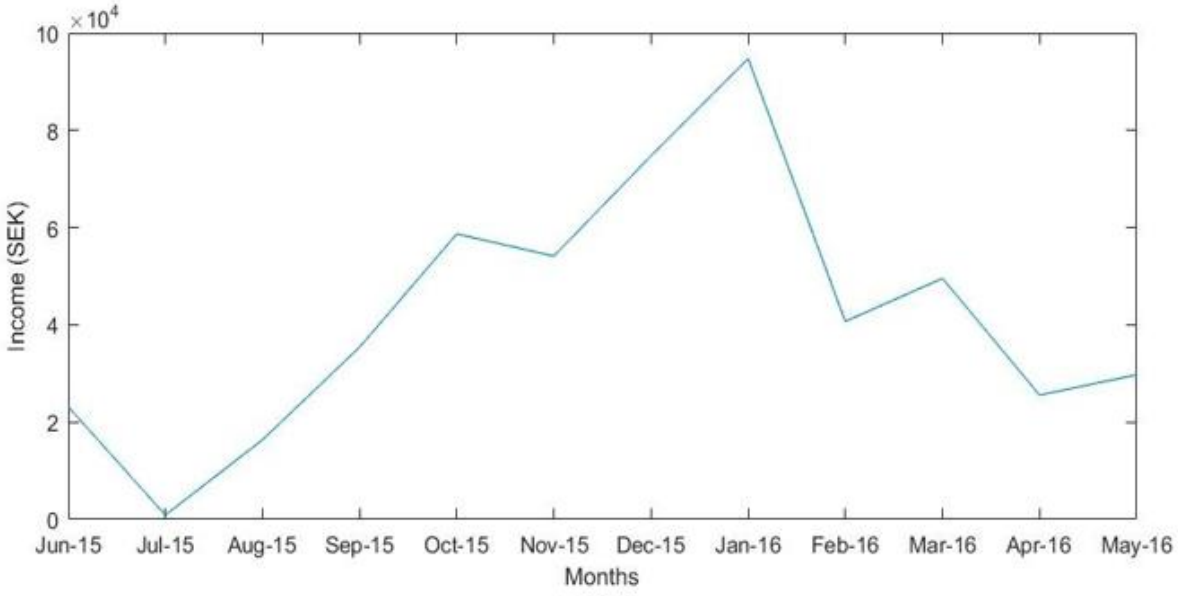



**Figure 3-16: Monthly income stream of the wind farm**

The stochastic nature of electricity and TGC prices is not considered in Figure 3-16. To address this, the Monte Carlo Simulation (MCS) approach is employed to estimate the income of the wind farm and analyse the impact of price components on the average income through sensitivity analysis. Historical data spanning ten years is collected for electricity and TGC prices, allowing the determination of monthly mean and standard deviation values for both parameters (see Table 3-5). The @Risk software [124] was used for 10,000 iterations of MCS each month, where both input parameters were assumed to follow a normal distribution. The MCS derived the PDFs of monthly incomes by generating random values of monthly electricity and TGC prices (based on the parameters given in Table 3-5). These PDFs were further used to obtain the simulated monthly mean incomes, shown in Figure 3-17. The analysis revealed a consistent pattern in the income generated by the wind farm, where both the simulated and actual incomes exhibited similar trends. Notably, the income was significantly higher during the winter months compared to the summer months. However, an intriguing observation was made: the simulated income values exceeded the actual income recorded from 2015 to 2016. This observation suggests a decline in prices over the years, as the historical mean prices were higher than the actual prices observed during 2015-2016.

**Table 3-5: Parameters for Monte Carlo Simulation**

| Month | Monthly mean electricity prices (SEK/MWh) | Standard deviation of electricity prices (SEK) | Monthly Mean TGC prices (SEK/MWh) | Standard deviation of TGC prices (SEK) |
|---|---|---|---|---|
| January | 398 | 151.31 | 225 | 56.35 |
| February | 426 | 209.23 | 226 | 55.8 |
| March | 374 | 142.3 | 222 | 53.34 |
| April | 361 | 99.14 | 219 | 59.23 |
| May | 336 | 80.53 | 216 | 71.89 |
| June | 348 | 103.8 | 210 | 66.49 |
| July | 330 | 125.17 | 212 | 67 |
| August | 365 | 142.24 | 218.91 | 66.12 |
| September | 379 | 162.38 | 222.7 | 68.91 |
| October | 378 | 110.69 | 225 | 68.81 |
| November | 387 | 92.262 | 223 | 60.32 |
| December | 414 | 166.37 | 217 | 53.94 |

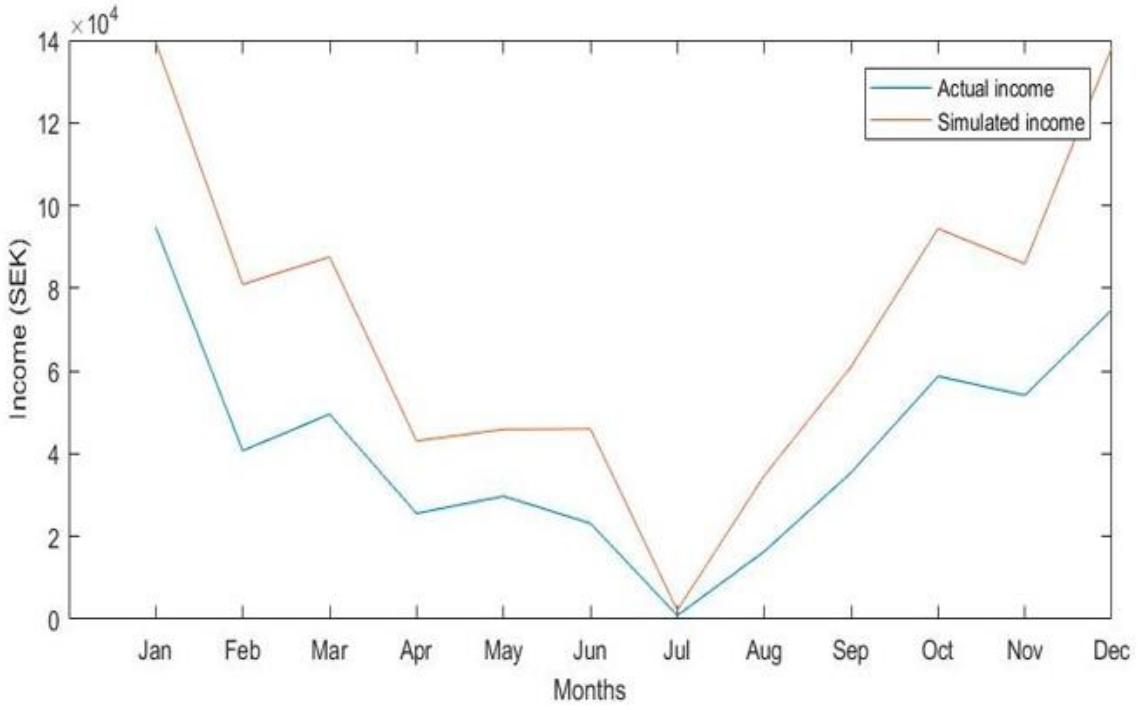



**Figure 3-17: Actual and simulated income of the wind farm**

Moreover, the sensitivity analysis was performed using @Risk software to see how both prices affect the overall monthly incomes. For demonstration, a 'Tornado graph' for January 2016 is represented in Figure 3-18. The Tornado graph visualizes how the simulated income of the wind farm fluctuates as each uncertain price varies within its range. The input displayed at the top exhibits the highest impact on the wind farm's income. Additionally, Figure 3-19 illustrates the contribution of each input to the variance of the mean monthly income for January. It is observed that electricity prices contribute 87.85% to the variance of the monthly income for January 2016, while TGC prices contribute 12.15%. This indicates that electricity prices significantly impact the wind farm's monthly income compared to TGC prices.

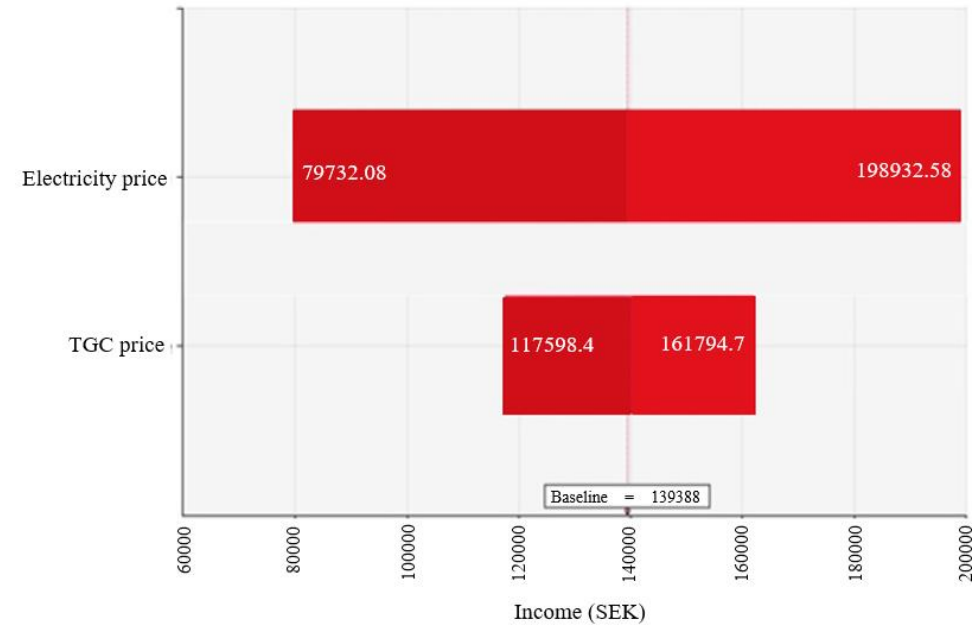



**Figure 3-18: Changes in mean output with respect to electricity price and TGC price for January**

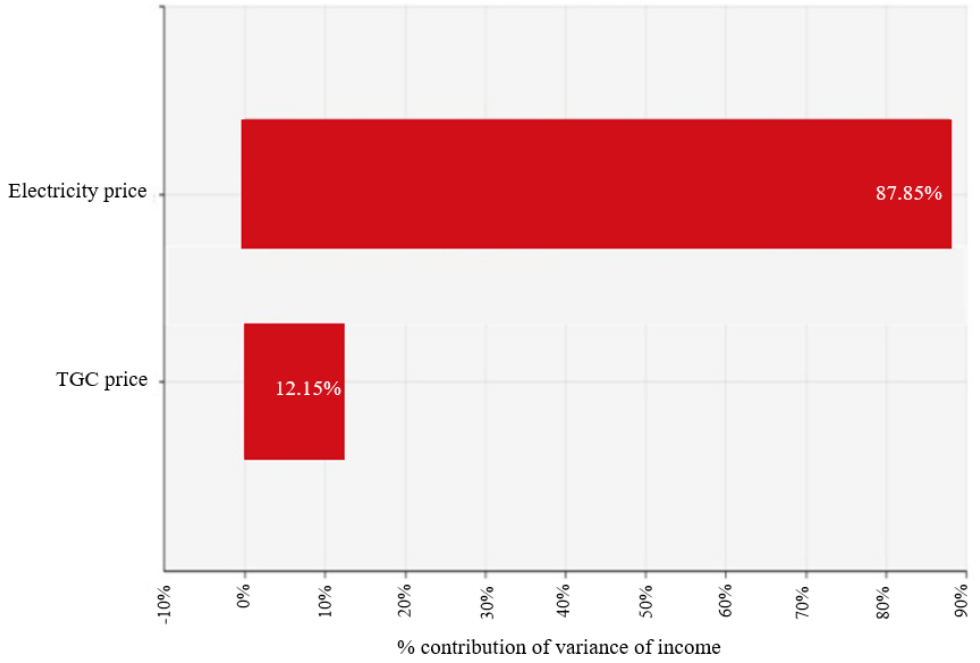



**Figure 3-19: Contribution of electricity price and TGC price to variance of income for January**

## 3.6 Conclusions

A methodology was developed to conduct wind resource analysis for a wind farm comprising three wind turbines, utilizing the wind turbine IEC61400-12-1 power measurement standard. The analysis incorporated data collected over a span of 12 months from the LIDAR positioned within the wind farm. The MCP method was used for the long-term analysis to predict wind behaviour by comparing it with the 38 years of wind data collected from a metrological station located at 63.5 N, 9.375 E. It was observed that winter contributed considerably towards the AEP, whereas only December and January contributed to 30% of the AEP. Moreover, it was found that wind mostly comes from southeast and southwest directions at the wind farm. The wind power class of the wind farm was also rated between 4 and 5, representing good to excellent category.

The mean monthly power and energy generated by a Vestas V-27 wind turbine were acquired and subsequently compared to the turbine's actual power production. The analysis revealed that the power production calculated based on the manufacturer's provided power curve exceeded the actual power produced. This difference was attributed to various factors such as wake effects losses, bearing losses, availability losses, and generator losses. Moreover, the power curve obtained through the best-fit curve of the measured data in the wind farm exhibited a similar trend to the actual power curve.

The effect of spot prices of electricity and the TGC on the income generated by the wind farm was also investigated. Additionally, a sensitivity analysis was conducted to account for the stochastic nature of these prices and capture their potential fluctuations. The percentage contribution of electricity price and TGC price to the variance of monthly income for January is 87.85% and 12.15%, respectively. Moreover, a similar pattern was observed for other months. It can be concluded that the variation in electricity prices has outnumbered the variation in TGC prices over the years.

This analysis is crucial for the fatigue design of OWTs as wind farms' performance provides insights into the turbines' behaviour under real-world conditions. This chapter demonstrates the methodology for obtaining the 2D

scatter diagram (wind speed and wind direction). The offshore wind industry makes use of a 3D scatter diagram which includes information on wind speed, wave height and wave period. The same methodology is extended further by placing a LIDAR with a buoy to obtain simultaneous wind and wave data. The environmental load information is needed to obtain the 3D scatter diagram and the fatigue damages are based on the values of this scatter diagram. Moreover, this information helps identify critical loading scenarios and assess the OWTs' ability to withstand long-term cyclic loading. Furthermore, wind resource analysis and performance evaluation provide valuable insights for decision-making processes related to turbine design and maintenance strategies. The income estimation approach may help compare the real income generated by the wind farm containing the optimised wind turbines to the original wind turbines.

The next chapter presents a methodology for constructing an OWT model specifically designed for fatigue design purposes. The analysis will focus on identifying the key parameters that influence the dynamic response and fatigue life of the OWT. As this chapter showed the methodology to determine the wind resource for an onshore wind turbine, the wave resource at a given site is also estimated using a similar approach. The next chapter will utilise the aerodynamic and hydrodynamic loads calculated through this methodology to conduct fatigue life calculations for the OWT.

# 4 Dynamic Response and Fatigue of Offshore Jacket Foundation

The durability of offshore foundations is influenced by a combination of harsh environmental conditions and intricate service loads. To accurately capture the complex nature of this phenomenon, fatigue limit state (FLS) analysis must be conducted in the time domain. This chapter reports work on investigating different parameters and design modifications that can impact the design life of an offshore jacket foundation. An OC4 jacket foundation is designed in industrial software from DNV and reduced to a superelement model. The superelement model is connected to an NREL 5 MW wind turbine designed in Bladed software. By utilizing time-series loads, the analysis calculates the fatigue damage experienced by the foundation throughout its service life. The comparison is made between the effects of the nonlinearity of soil, marine growth, scour size, the transition piece's mass, and the grouted connection's design on the dynamic response and fatigue damages. The analysis introduces a novel approach incorporating distinct modifications in the offshore foundation design and the grouted connection. It also utilises a different material for the transition piece to assess the effect of these changes on the structure's dynamic response and fatigue life.

A version of this chapter has been published as: Marjan A, Hart P. Impact of Design Parameters on the Dynamic Response and Fatigue of Offshore Jacket Foundations. *Journal of Marine Science and Engineering*. 2022; 10(9):1320

## 4.1 Introduction

The International Renewable Energy Agency (IRENA) predicts that wind power will meet over 33% of the world's electricity needs by 2050 [125]. Constantly improving the design of offshore wind turbine (OWT) foundations is essential for accelerating their adoption and reducing costs. An OWT faces a combination of complex loads throughout life, and fatigue life is the main performance criterion of OWT foundations [3]. An integrated or super-element design approach can be used for time-series fatigue analysis. A previous study compared integrated and superelement approaches in [126] and found similar fatigue damages. The same set of software was used to perform fatigue analysis of a 10-MW wind turbine using an integrated design approach in [127]. It was observed that integrated or super-element approaches could be used alternatively.

The primary objective of this research is to establish the effect of various parameters on the jacket foundation's dynamic response and fatigue life. This study focuses on a superelement method, where an OC4 jacket foundation modelled in Sesam is reduced to the superelement file. The interface point is then shared with the Bladed software to compute the time series of forces and moments in three axes. The time series of loads are imported in the Sesam Wind Manager (SWM) to generate a time series of stress ranges, which eventually is used to determine fatigue damages. The process is repeated on similar environmental conditions for a set of parameters and design modifications to obtain their effect on the dynamic response and fatigue damages.

### 4.1.1 Reference model

### 4.1.2 Site specifications

The site-specific data used in this study is from the K-13 deep water site. The site is located in the North Sea and has a water depth of 50 m. The wind and wave climate definition is discussed in detail in Upwind Design Basis [128] and has been used by many studies due to data availability and validation purposes. JONSWAP spectrum is mostly used in coastal or shallow water, while the Pierson-Moskowitz (PM) is preferred for deep water as it can provide reasonable

energy distribution of waves in open sea. Moreover, the PM spectrum assumes that the sea state is mature (reached equilibrium) According to the PM wave spectrum, the wave conditions are characterised by the peak spectral period and significant wave height. Important site-specific data are summarised in Table 4-1. A peak-ness factor of 1.0 was used for fatigue load cases, and a factor of 3.3 was used for all other cases, as advised in [128]. The effect of wind-wave directionality has not been considered, and a steady-state wind condition is used for simplicity. A current profile is defined for normal current and a current profile is ensured at the crest of the highest wave by defining the current values at the crest of the highest wave, at the location of still water and the seabed. The software finds the intermediate values between the still water and the seabed by interpolation.

**Table 4-1: K-13 site environmental data**

| Parameter | Value |
|---|---|
| 50-year significant wave height | 9.4 m |
| 50-year max wave height | 17.48 m |
| 50-year max wave period | 10.87 s |
| Reference wind speed | 42.73 m/s |
| Marine growth (-2 to -40 m) | 100 mm |
| Marine growth density | 1100 kg/m$^3$ |
| Normal current at MSL | 0.6 m/s |
| Extreme current at MSL | 1.2 m/s |

### 4.1.3 Wind turbine model

The research focuses on the NREL 5 MW baseline offshore wind turbine, described by Jonkman et al. in [129]. The wind turbine was developed for research and conceptual studies to assess the effect of offshore wind energy in deep and shallow water. The model was developed by combining publicly available data from the Repower 5M prototype, the Multibird M5000, and projects

like WindPACT, RECOFF, and DOWEC. The model has widely been used by many projects (Upwind Design Basis [128], IEA Wind Annex OC3 [130], and OC4 projects [131]) for code comparison and to standardize baseline offshore wind turbines.

The NREL 5MW wind turbine is an upwind, three-bladed horizontal axis wind turbine. The hub height is 87.5 m. Moreover, the tower mass is centred along the tower centerline. The main dimensions and characteristics of the turbine are given in Table 4-2 [129].

**Table 4-2: NREL 5MW specifications**

| **Rotor** | | **Tower** | |
|---|---|---|---|
| Diameter | 126 m | Height | 87.6 m |
| Rotor orientation | Upwind | CM location | 38.234 m |
| Hub height (OC4) | 90.55 m | Diameter top | 3.87 m |
| Rated rotor speed | 12.1 | Diameter bottom | 6 m |
| Number of blades | 3 | Thickness top | 0.019 m |
| **Drivetrain** | | Thickness bottom | 0.027 m |
| Generator rotational speed | 1173.7 RPM | **Masses** | |
| Rated rotor speed | 12.1 | Tower | 347,460 kg |
| Gearbox ratio | 97:1 | RNA | 350,000 Kg |
| **Operational data** | | Hub mass | 56,780 kg |
| Cut-in speed | 3 m/s | Blade mass | 17,740 kg |
| Rated wind speed | 11.4 m/s | | |
| Cut-out wind speed | 25 m/s | | |
| Rated power | 5 MW | | |

## 4.2 FEA model

The FEA model of the jacket and soil was developed in the Genie module of Sesam software, which has widely been used in the industry for research and development purposes. The analysis is performed on the developed model based on the site-specific conditions, such as wind, wave, and current loads. The steps involved in developing the model and the definition of the foundation model are discussed in the following sections.

The meshing is based on a beam element theory, and the Framework module later used for the fatigue damage calculation suggests two-node beam members. In beam element meshing, the focus is not on a certain mesh size but on the interconnected framework of beams with certain cross-sectional properties connected at the nodes. These kinds of elements are mainly used to capture the overall non-linear dynamics of the multi-body system, such as an offshore wind turbine. The accuracy of using beam elements in a multi-body dynamic system has been discussed by Wang et al. [132] Moreover, beam elements are mostly used in structures that are mainly subjected to bending and axial loads but are not suitable to capture shear and torsional loads. Sesam default setting for meshing was used, which places the nodes at the end of the beam, and additional nodes are placed at the connection points and at the edges of cans and stubs.

### 4.2.1 Jacket support structure model

This chapter focuses on the jacket-type foundation, usually four-legged, connected with braces through welded joints. The wind turbine is attached to the jacket support structure used in phase-1 of the OC4 project. The four levels of X-braces are connected with the four-legged jacket, and piles have a penetration depth of 45 m. The jacket has a total height of 70.15 m, including the TP (transition piece), which is 4 m high. The main properties of the OC4 jacket support structure are given in Table 4-3; complete details can be found in [131]. The model was developed in Genie based on the provided information. The colour-coded Jacket support structure showing different cross-sections is given in Figure 4-1.

**Table 4-3: OC4 jacket support structure parameters**

| Component | Value |
|---|---|
| Steel density | 7850 kg/m$^3$ |
| Young's modulus | 2.1E11 N/m$^2$ |
| Poisson's ratio | 0.3 |
| Yield strength | 355 MPa |

| | |
|---|---|
| Number of legs | 4 |
| Water depth | 50 m |
| X and mud braces OD, thickness | 0.8 m, 20 mm |
| Lowest level leg OD, thickness | 1.2 m, 50 mm |
| 2nd to 4th level legs OD, thickness | 1.2 m, 35 mm |
| Leg connecting TP OD, thickness | 1.2 m, 40 mm |
| Pile OD, thickness | 2.082 m, 60 mm |
| Jacket height above mudline (including TP) | 70.15 m |

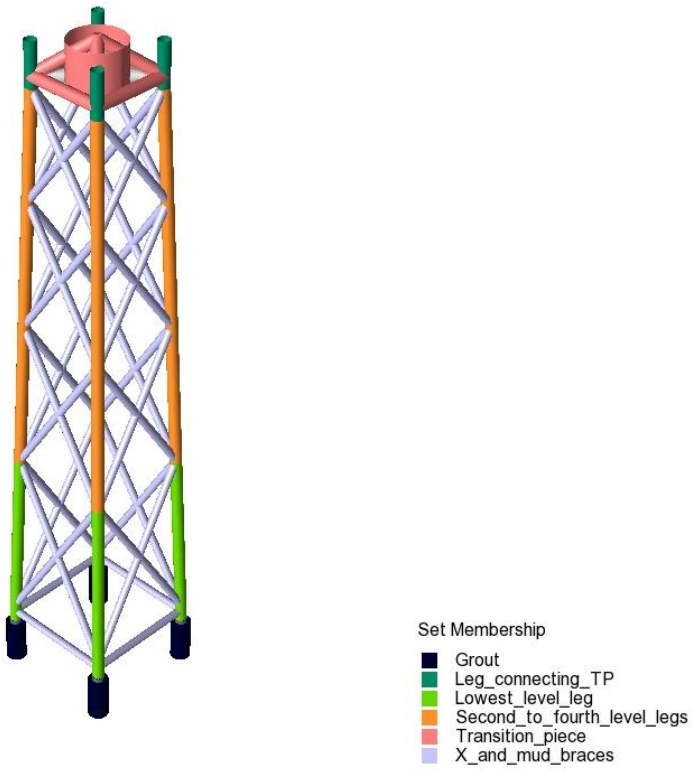



**Figure 4-1: Genie model of the jacket foundation**

### 4.2.2 Grouted connection

The base model in the OC4 project only considers the jacket above the mudline, and only the section of piles above the mudline is considered. This implies that all six degrees of movement are considered zero. The pile has a bigger diameter

and is connected with the leg by filling grout material between the surfaces. The grout material utilised in this research has a 2000 kg/m$^3$ density. The specific properties of the grouted connection employed in the research can be found in reference [131]. The grout connection volume from mean sea level -45 to -49.5 m is considered rigid in the model due to very high stiffness (see Figure 4-2). Moreover, the location of the grouted connection is visually shown in black colour in Figure 4-1. This rigid model was used to perform the linear analysis, while the non-linear analysis included the soil and pile model. Further explanation is provided in the subsequent sections.

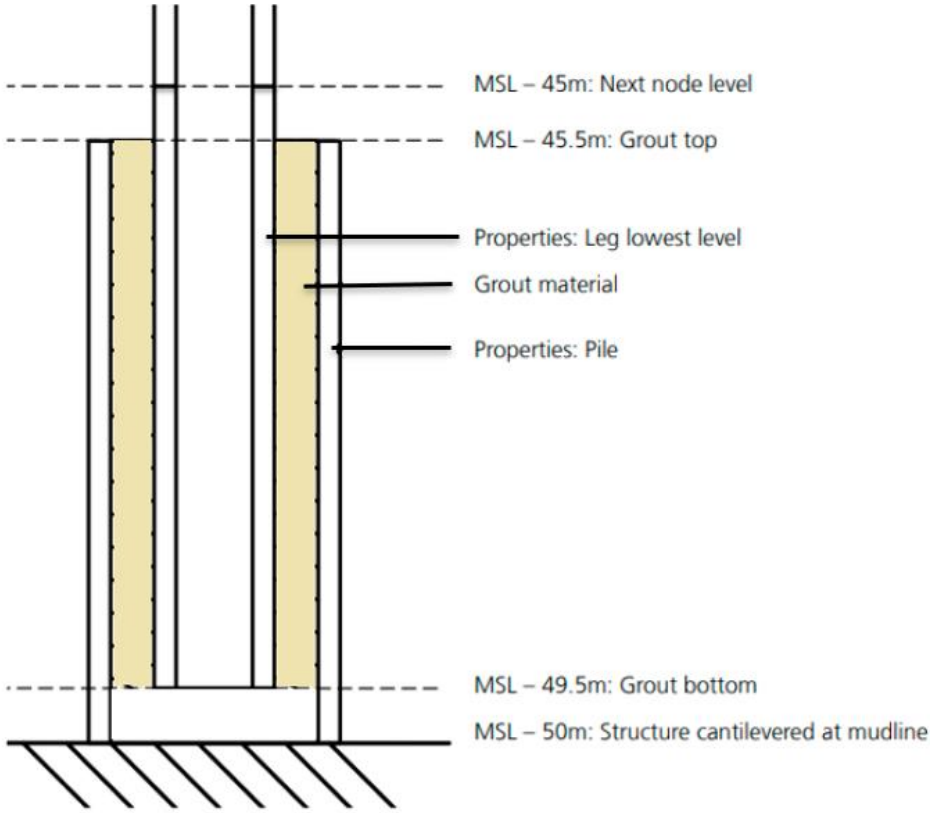



**Figure 4-2: A grouted connection between pile and leg**

### 4.2.3 Transition piece

The OC4 model considers the transition piece (TP) a rigid concrete block with a mass of 666 t. However, Genie lacks the ability to model a concrete block. The TP was, therefore, modelled as a beam with increased stiffness to simulate a

similar effect (see Figure 4-1 ). Moreover, point mass was included to obtain a total mass of 666 t.

### 4.2.4 Soil-structure interaction modelling

The laterally loaded piles are mostly modelled with a simplified method called Beam on Non-linear Winkler Foundation (BNWF) or a p-y method. The method provides simplicity and saves computational costs over the 3D FEA model. The hypothesis is that the soil reaction (p) exerted by the soil at the pile is proportional to the pile displacement (y). This method is widely used in the offshore oil & gas industry to find pile deformations and stiffness and is given in API and DNV industry standards. Although this approach has been widely used for the oil & gas industry design, its accuracy is questionable for offshore foundations having a large diameter (such as monopile). The study [63] has determined that the p-y method overestimates the displacement, stiffness, and bending moment compared to the FE methods for monopile. However, the same study suggests using the p-y method to model the soil for slender bodies (such as jacket foundations, because it is reasonably accurate and provides good computational efficiency. The importance of proper soil-structure interaction for jacket foundations is discussed in [133].

The analysis is performed in the K-13 deep-water site. The six-layered soil profile of the site given in [128] was modelled in Genie (see Table 4-4). The complete model showing the tower, jacket, piles, and six-layered soil is shown in Figure 4-3.

**Table 4-4: Soil profile of k-13 deep-water site**

| Soil depth (m) | Unit weight ($N/m^3$) | Friction angle ($^0$) | Young's modulus (MPa) |
|---|---|---|---|
| 0-3 | 10000 | 36 | 30 |
| 3-5 | 10000 | 33 | 30 |
| 5-7 | 10000 | 26 | 50 |
| 7-10 | 10000 | 37 | 50 |

| | | | |
|---|---|---|---|
| 10-15 | 10000 | 35 | 50 |
| 15-50 | 10000 | 37.5 | 80 |

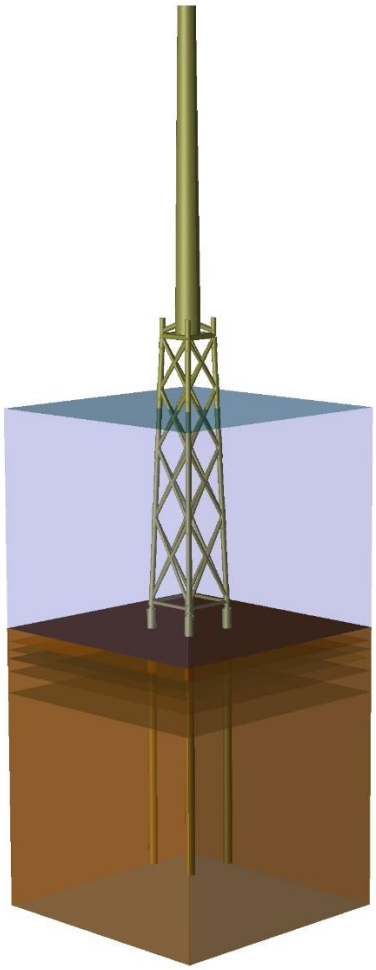


**Figure 4-3: Complete 3D model of the jacket and soil profile**

## 4.3 Model validation

### 4.3.1 Modal analysis

The modes of vibration were determined for a fixed foundation and non-linear pile-soil model. It is crucial to design a semi-rigid foundation (fixed at the base with some mobility like a jacket foundation in soil) so that the first natural frequency doesn't approach near the 1P and 3P region to avoid resonance. Figure 4-4 shows that the system's natural frequency with the NREL 5MW wind

turbine should be between 0.22 Hz and 0.35 Hz [134]. The modal frequencies of the model with a fixed base and the non-linear model with soil were computed and compared with the existing literature. The first four frequencies of the fixed foundation were compared with [135] and the frequencies for both non-linear pile-soil models were compared with [136]. The results are compared in Table 4-5, where the second side-to-side bending (-9.1%) depicts the maximum deviation. This confirms the validity of the model.

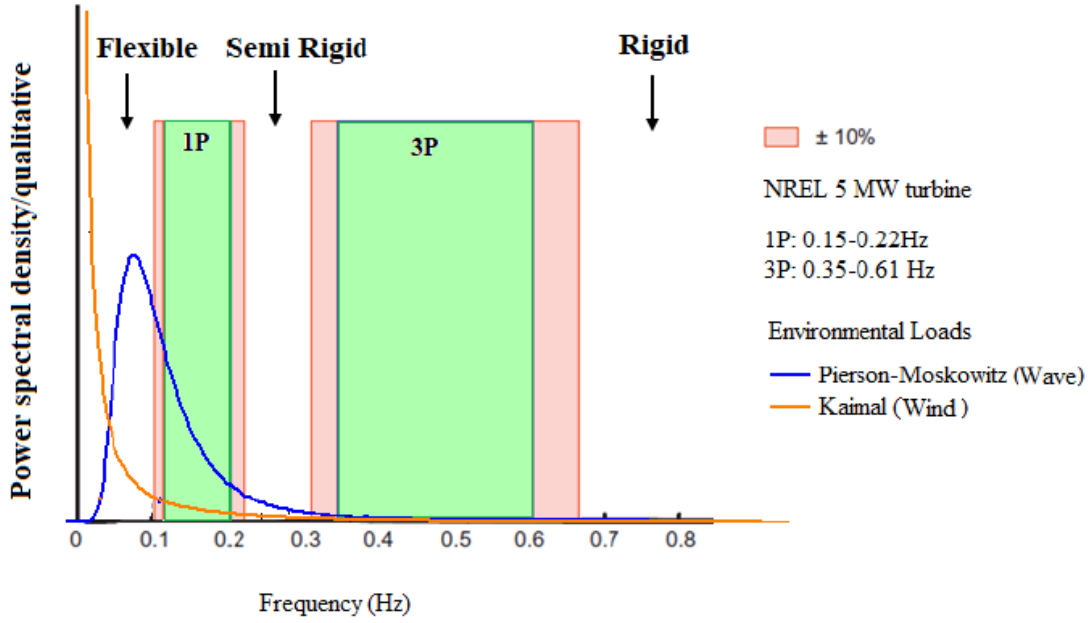



**Figure 4-4: Power density of NREL 5MW wind turbine [Adapted from** [26]**]**

**Table 4-5: Comparison of natural frequencies with the reference values**

| **Models** | **Natural frequencies (Hz)** | | | |
|---|---|---|---|---|
| | 1st Fore-aft | 1st Side-to-side | 2nd Fore-aft | 2nd Side-to-side |
| Fixed base [This study] | 0.3169 | 0.3169 | 1.1799 | 1.1799 |
| Fixed base [135] | 0.3189 | 0.3189 | 1.1936 | 1.1936 |
| Non-linear soil [This study] | 0.2935 | 0.2935 | 0.935 | 0.937 |
| Non-linear soil [136] | 0.2772 | 0.2795 | 0.8931 | 1.023 |

### 4.3.2 Static analysis

The deflection behaviour of the structure was assessed with static analysis and compared with the results given in [135]. The maximum displacement at the RNA was observed for comparison under the loaded conditions. Table 4-6 shows a good agreement with the literature, with a minor difference of -0.36%, further validating the model.

**Table 4-6: Static deformation of the baseline wind turbine model**

| Load case RNA mass/ Thrust | Displacement at RNA | | |
|---|---|---|---|
| | Present | Ref. [135] | % Difference |
| 350 Tonne/ 2 MN | 1.2045 m | 1.2089 | -0.36 % |

The contour plot of the deformation of the whole model and the graph of tower deflection along its length, with a fixed foundation, is shown in Figure 4-5.

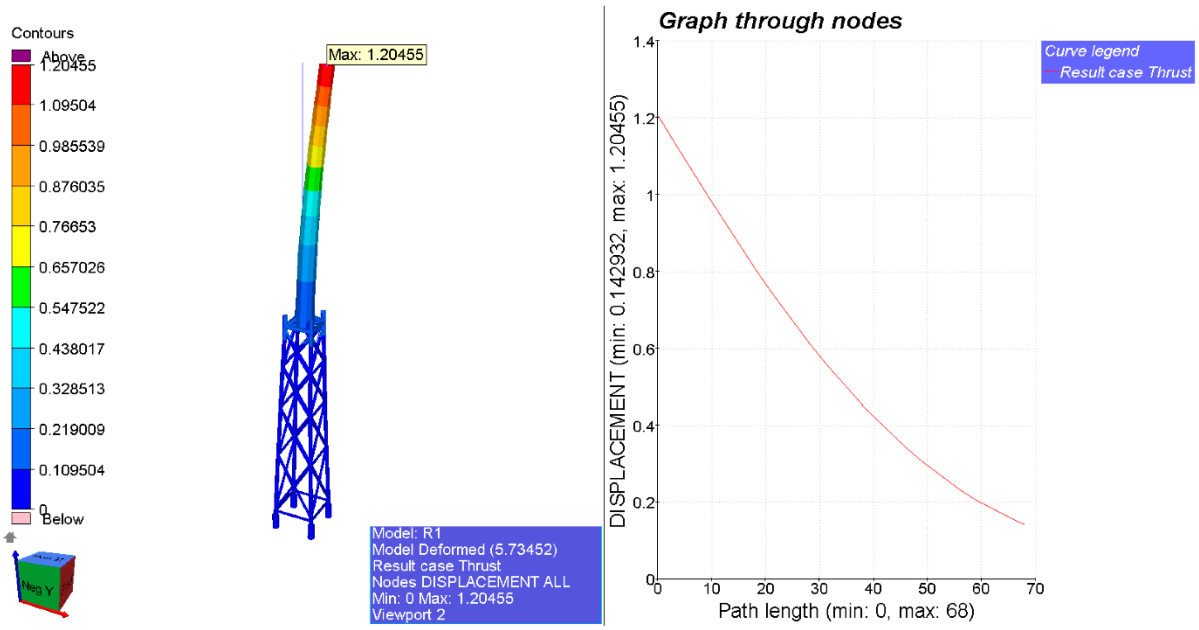



**Figure 4-5: Deflection with the fixed base**

## 4.4 Fatigue limit state (FLS) analysis

The fatigue design of OWT support structures is controlled by the dynamic response to combined aerodynamic and hydrodynamic loads [137]. The two most often used fatigue assessment techniques are the S-N curve and fracture mechanics approaches. As advocated by the standards [31] and [32], the S-N curve method is the focus of this research. The S-N curve, which is based on experimental data and is a plot of Stress S against the number of cycles N, is used to calculate the fatigue failure of an object. The experiments are repeated for many similar specimens under stress to obtain the design S-N curve. The stress range at a point is related to the number of cycles to failures with the help of Equation 2-18. Where N is the number of cycles to failure, m is the negative inverse slope of the S-N curve, σ is the stress, and C is the intercept of the S-N curve with the log of the number of cycles N. The analysis estimates tubular joint stress concentration factors (SCFs) based on geometry and butt welds. The fatigue life is based on the rainflow counting of stress time histories [138].

### 4.4.1 Methodological approach for FLS

The FLS analysis is performed based on the superelement approach discussed later. The FLS load calculation is based on the Design Load Cases (DLCs) recommended by [139]. FLS analyses are typically performed for DLC 1.2, DLC 6.4, and DLC 7.2. This study focuses on the DLCs given in Table 4-7, and DLC 7.2 (idling after fault) is omitted because most of the fatigue life is based on these DLCs only. The simulation length for FLS analysis should match the length of simulations in the Bladed because the fatigue damages are calculated based on the Bladed's interface load file. The simulation duration is selected as 200 seconds and the first 20 seconds are discarded to avoid any possible transients. Sesam recommends the simulation duration of 600 seconds but a simulation length of 200 seconds was selected because of the need to simulate more than 100 load cases. Moreover, Sesam support confirmed that a simulation length of 200 seconds can provide reasonable accuracy. Moreover, a reduced form of scatter diagram in the North-sea (in Table 4-8) is used to obtain the result due to the increased number of simulations to observe the effect of different parameters

on the time-series fatigue life. DNV-RP-C205 standard [33] recommends the site-specific use of the scatter diagram in the North Sea for the design under hostile conditions, such as for ships moving worldwide. DNV-RP-C205 have a list of scatter diagrams and Sesam has the scatter diagram of North-sea and world wide trade scatter diagrams for use in Postresp. The Sesam's Postresp is a geographical post processor for the statistical processing of the data in the time and frequency domain. The reduced scatter diagram used in this study is for the North sea and is used in many verification studies and tutorials by Sesam. Moreover, the site-specific data used in this study is also for the North sea. Compared to the full diagram, where a wind speed bin size in the method of bins is recommended to be 2 m/s, a reduced scatter diagram uses a larger bin size. This enables more wind speeds to be captured in one wind speed bin.

**Table 4-7: Design load cases**

| Design load case | Description | Type |
|---|---|---|
| DLC 1.2 | Power production | FLS |
| DLC 6.4 | Idling | FLS |

**Table 4-8: Scatter diagram**

| Wind speed (m/s) | Wave height (m) | Period (s) | Occurrences/yr (hrs) | DLC |
|---|---|---|---|---|
| 4 | 1.11 | 4.15 | 4365 | DLC 1.2 |
| 14 | 1.90 | 4.30 | 2185 | DLC 1.2 |
| 24 | 3.42 | 5.51 | 545 | DLC 1.2 |
| 2 | 1.08 | 4.25 | 1260 | DLC 6.4 |
| 30 | 4.46 | 6.25 | 410 | DLC 6.4 |

The analysis was conducted using multiple software modules, and Figure 4-6 presents a summarized flowchart illustrating the various software employed and their respective purposes. The jacket model was developed and validated in the Genie module of the Sesam software. The validated foundation model in section 4.1.1 was exported to the SWM, where the Wajac input file defined the hydrodynamic properties, and Sestra defined the type of analysis. Moreover, the

superelement files were generated based on the input data in the SWM. The superelement model is exported to Bladed where an NREL 5 MW wind turbine is defined and attached to the jacket's superelement model. The time-series loads are generated in the Bladed based on the scatter diagram and the output of this process is an interface load file. These loads are imported into the SWM, where FLS simulation is performed to calculate the SCFs on each joint/member based on the defined S-N curve. Eventually, fatigue damages are calculated at each joint for 20 years of service life with the help of Miner's rule.

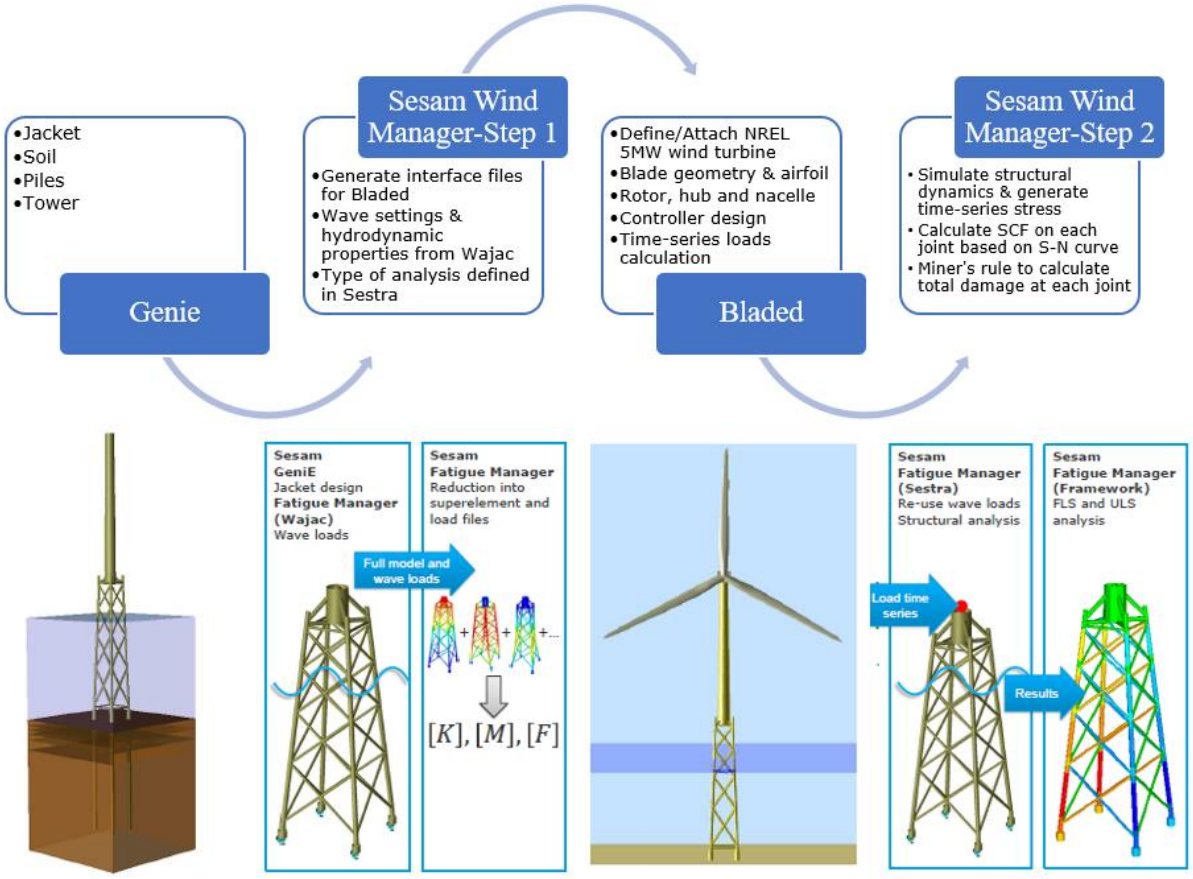



**Figure 4-6: Flowchart of software modules**

### 4.4.1.1 Superelement design method

Sesam offers time-series FLS analysis in integrated and superelement approaches. The entire structure (including the tower) is modelled in Genie and exported to Bladed to generate time-series loads in an integrated design approach. The study [140] uses an integrated design approach on a 10 MW

offshore wind turbine. However, in the superelement approach, only the jacket and the wave loads are exported to Bladed as a superelement.

The superelement method is implemented in this research because it is extensively used in the industry due to the lack of a requirement to share the jacket design and the ability to export complex designs [141]. The superelement model should behave similarly to the integrated model. DNV has published verification studies showing the accuracy of the superelement method in [142]. Moreover, integrated and superelement approaches are compared in [126]. Figure 4-7 shows the schematic of the superelement method.

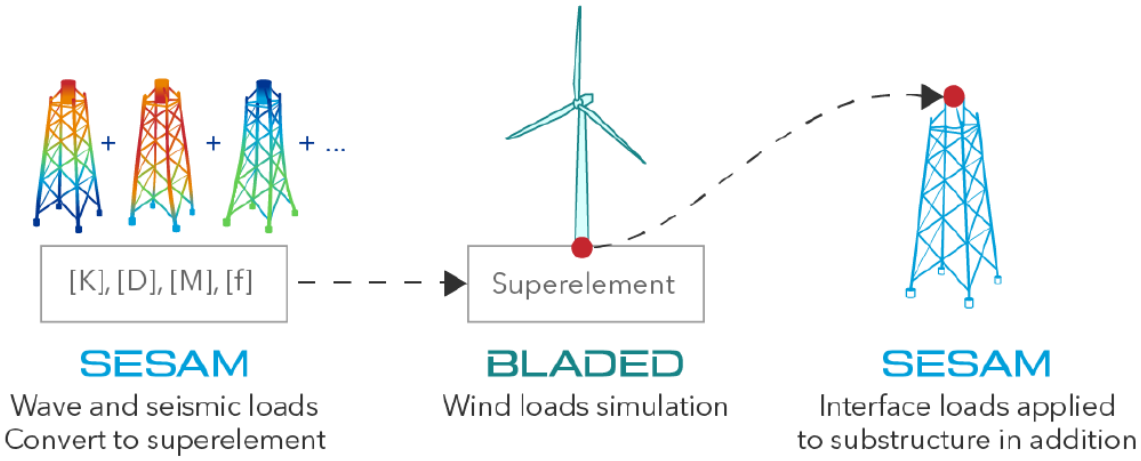



**Figure 4-7: Superelement method** [141]

The superelement files contain the model's mass matrix, gravity vector, and stiffness matrix information. The damping matrix was generated using the Rayleigh coefficients, stiffness, and mass matrices. The original model was verified with the literature, as discussed in section 4.3. However, the superelement data must also be converged (spectral and spatial) to replace the original model.

#### *4.4.1.1.1 Spectral convergence*

Spectral convergence involves comparing the free vibration modes of the superelement model and those of the original model. It thoroughly compares mode shapes and natural frequencies to ensure their alignment and similarity. By

analysing and verifying the spectral convergence, we can be sure of the superelement's accuracy in capturing the original model's dynamic response.

The boundary node is at the interface point and contains only 6 degrees of freedom (DOFs), which is insufficient. Hence, 40 additional DOFs were added to the superelement model to capture actual dynamic responses based on the original model. The number of modes was selected after the dynamic response converged and was similar to the modal shapes based on the standalone jacket model in Genie. The verification report suggests that using 40 or more modes may reduce the difference between the two models to a maximum of 0.5%. Genie is used to obtain the eigenvalue frequencies of the jacket (excluding RNA and tower), and SWM obtains the superelement model's frequencies. The model's modal frequencies are compared for the first 20 modes in Table 4-9, showing a maximum difference of only 0.16%. It shows that both models can be used interchangeably to produce similar responses.

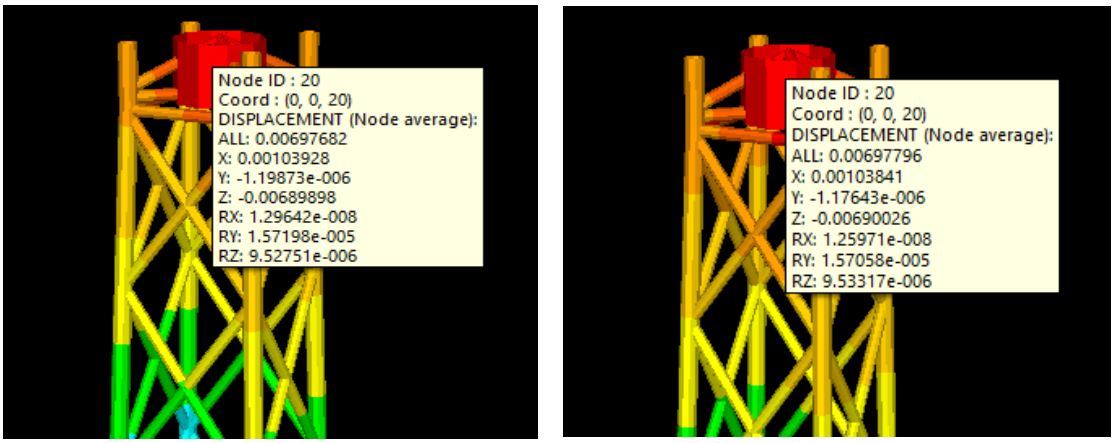
**Table 4-9: Comparison of modal frequencies of original and superelement model**

| Mode number | Original model freq. (Hz) | Superelement model freq. (Hz) | Difference (%) |
|---|---|---|---|
| 1 | 1.0885 | 1.0887 | -0.01837 |
| 2 | 1.0885 | 1.0887 | -0.01837 |
| 3 | 5.0687 | 5.07 | -0.02565 |
| 4 | 6.1037 | 6.106 | -0.03768 |
| 5 | 6.1038 | 6.106 | -0.03604 |
| 6 | 6.7875 | 6.8139 | -0.38895 |
| 7 | 7.4895 | 7.4896 | -0.00134 |
| 8 | 9.0797 | 9.0791 | 0.006608 |
| 9 | 9.4819 | 9.4845 | -0.02742 |
| 10 | 9.4821 | 9.4847 | -0.02742 |
| 11 | 9.7622 | 9.7631 | -0.00922 |
| 12 | 11.125 | 11.126 | -0.00899 |
| 13 | 11.816 | 11.835 | -0.1608 |
| 14 | 12.681 | 12.684 | -0.02366 |
| 15 | 12.695 | 12.7 | -0.03939 |
| 16 | 13.05 | 13.06 | -0.07663 |
| 17 | 13.215 | 13.223 | -0.06054 |
| 18 | 13.216 | 13.223 | -0.05297 |

| | | | |
|---|---|---|---|
| 19 | 14.121 | 14.122 | -0.00708 |
| 20 | 14.375 | 14.377 | -0.01391 |

#### *4.4.1.1.2 Spatial convergence*

To perform the superelement analysis, the superelement model should also show spatial convergence, i.e., similar behaviour under the same loading condition. A simulation is performed in SWM on the original model under a specific load, and displacement at the interface point is noted. Moreover, another simulation is performed on a superelement model to observe the displacement at the interface node under the same loading conditions. The results are compared in the Xtract module at t = 25s and show good accuracy, as shown in Figure 4-8.




(a) Displacements at the interface node of the original model

(b) Displacements at the interface node of the superelement model

**Figure 4-8: Comparison of nodal displacements for spatial convergence**

### 4.4.1.2 Aero-hydro-servo-elastic simulation

An aero-hydro-servo-elastic solver like Bladed is needed to simulate the coupled dynamic response of an offshore wind turbine. This complex simulation captures the interaction of a multi-physics system and simulates a holistic model in a coupled manner [143]. Although the superelement approach excludes hydro-servo interaction, the verification report [142] shows similar results by integrated and superelement approaches [144]. This superelement model was exported and attached to the NREL 5 MW wind turbine at the interface point. NREL 5 MW wind

turbine was fully defined in bladed, including blade geometry, airfoil sections, rotor, hub, nacelle, and tower.

The Bladed software can generate simple time-series loads with the built-in controller. However, the fatigue damages were relatively high because of the complex nature of FLS analysis. The light and dark blue lines (Figure 4-9) show the demanded generator speed and torque and are constant initially. However, the measured generator speed (orange) fluctuated around the demanded generator speed later in the simulation. The controller tries to correct this by pitching the blades (the green line fluctuates between $0^0$ and $20^0$), but it over-corrects and exacerbates the oscillation in generator speed. An external controller for the NREL 5MW wind turbine was implemented to improve the accuracy of fatigue results. Figure 4-10 shows the stabilized blade pitch angle for a demanded generator torque. It shows the need to design and implement an external controller to improve the accuracy of complex FLS simulations. It was also observed that the blade pitch angle increases at higher wind speeds but remains constant at a given wind speed.

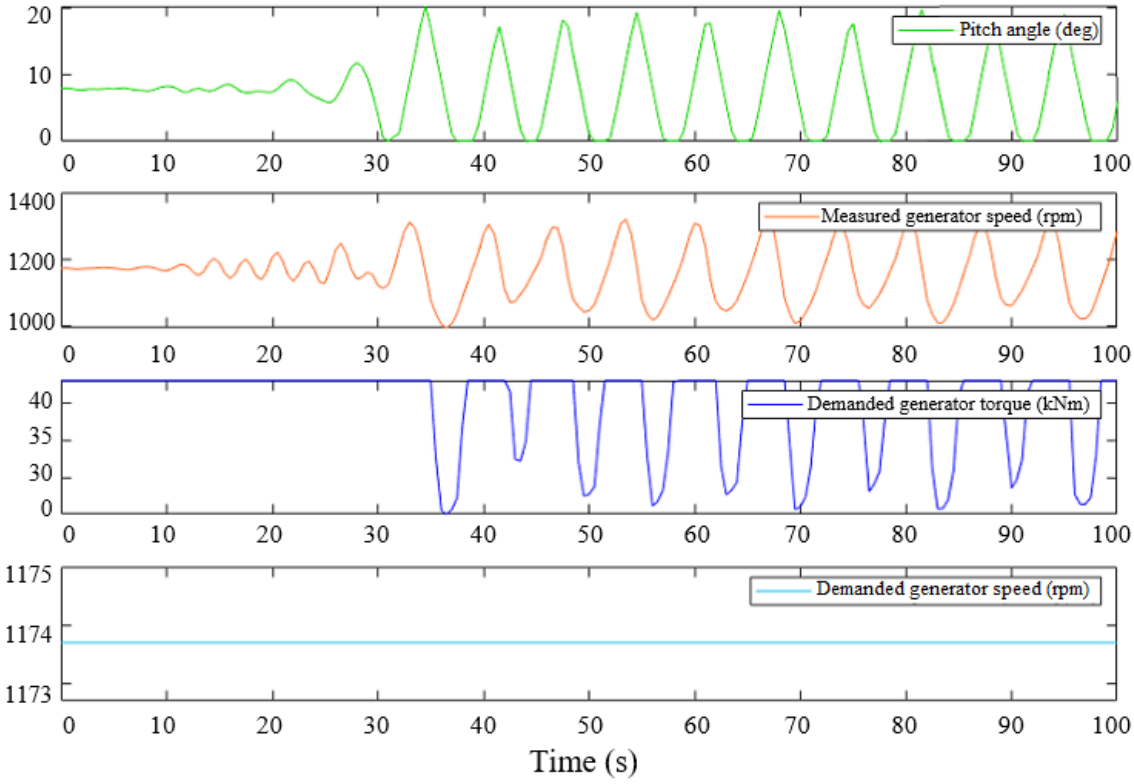



**Figure 4-9: Error in blade's pitch angle with built-in controller**

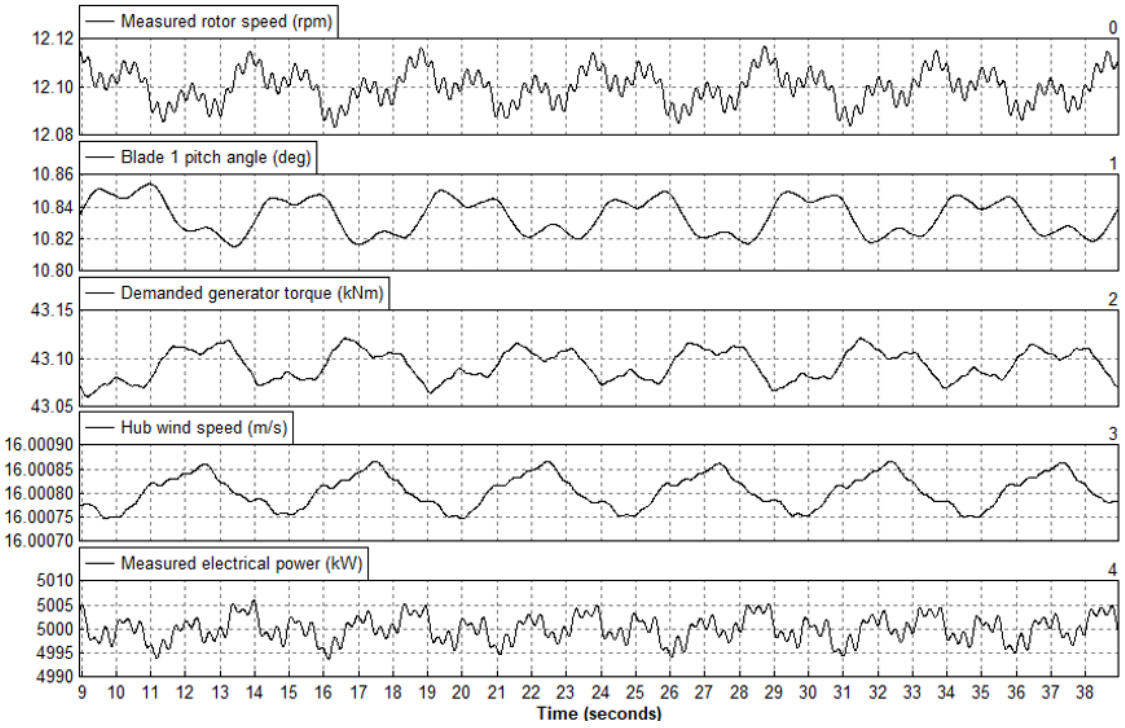



**Figure 4-10: Uniform blade pitch angle with designed controller**

#### 4.4.1.3 FLS simulation

The time-series load data from Bladed was then exported to SWM again to generate time-series stress. The stress concentration factors (SCF) were calculated based on the Efthymiou principle on each tubular joint. The calculation of SCFs considers the joint's geometry and the nature of applied loads. The software uses the method to calculate SCF as given in the standard DNVGL-RP-C203 [55]. Based on the SCFs and time-series of loads, stresses on the joints are calculated based on the hotspot stress approach. Figure 4-11 shows the location of hotspots on the brace. The highest value of the 8 locations on the circumference for each simulation was selected for the calculations [140]. Miner's rule was used to calculate the total damage at each joint after obtaining the time series of stress ranges. The calculation of damages is based on a user-selected S-N curve.

The fatigue damages are calculated in this research based on the hotspot stress approach suggested by the DNV standard. The stresses are calculated using a hotspot stress approach which is computationally less intensive because the focus is on the critical areas only. This approach is preferred for lifetime analysis studies where a structure may be facing a cyclic load. However, compared to the comprehensive FEA approach which considers the whole structure, the hotspot stress approach is not detailed and less accurate. The hotspot approach may provide the less detailed stress distribution but it is the recommended method for fatigue simulations in the design standards due to its reasonable accuracy and simplicity.

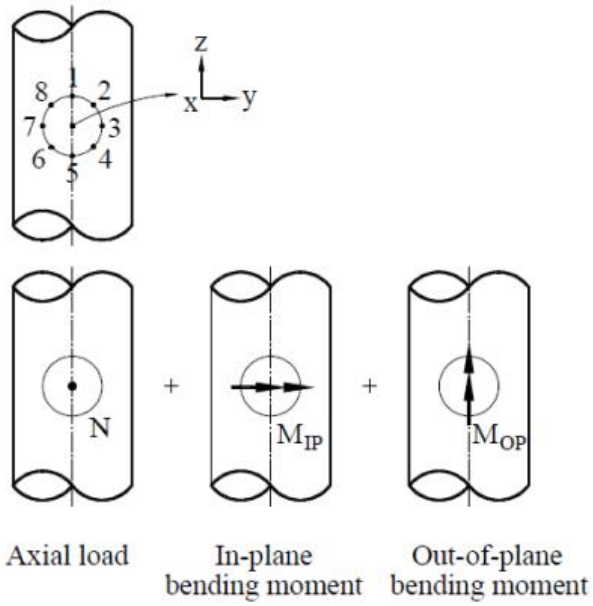



**Figure 4-11: Hotspot of K-joint** [55]

## 4.5 Results and discussion

The modelling parameters significantly affect the dynamic behaviour of the jacket, which also affects the fatigue life. Optimising the stiffness-to-mass ratio by varying design parameters to reach the perfect design is a typical feature of effective structural design. Identifying the parameters affecting the dynamic behaviour of the model is crucial for a better design. The effect of modelling parameters like marine growth, flooding, soil profile, the mass TP, the material of TP, scour development, and the length of grouted connection on the dynamic response was studied and discussed below.

The effect of these design parameters was also studied on the fatigue life of the jacket foundation. For this purpose, the fatigue life was compared for all the joints. Since the jacket design has a lot of redundancy, the fatigue life of the second worst-performing joint has been considered a failure. The location of the worst-performing joint is on the x-brace, as shown In Figure 4-12. The fatigue damage value of 1 represents when the jacket's crack initiates, which leads to failure. Moreover, the effect of different grouted connection configurations on the time-series fatigue life of the jacket has also been studied.

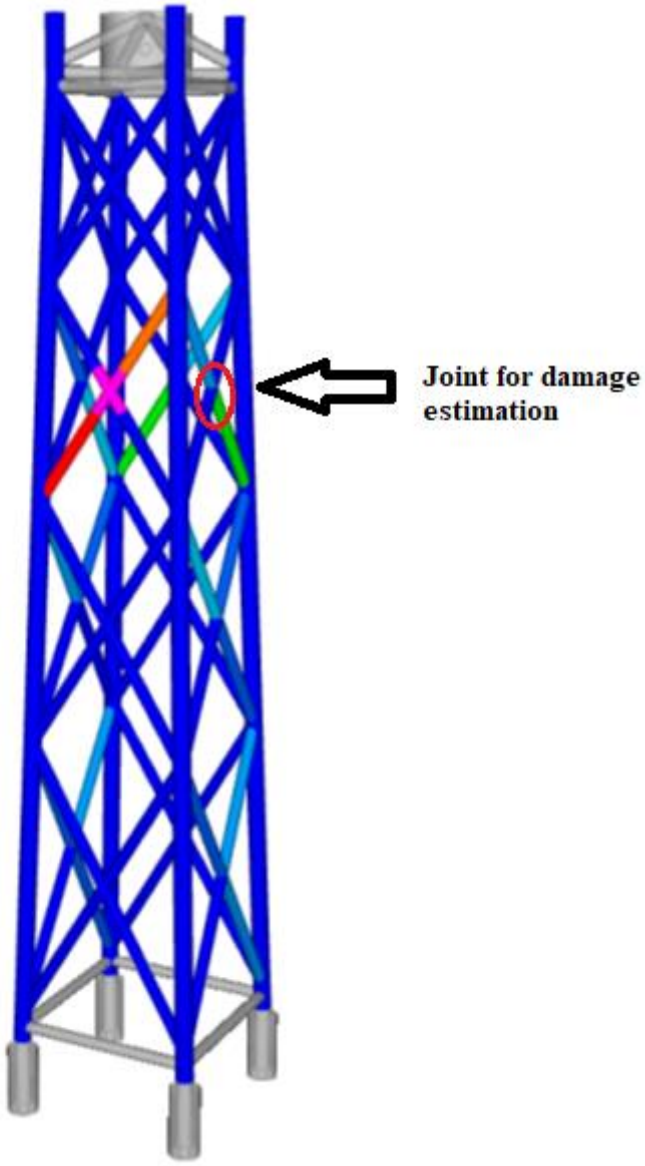



**Figure 4-12: Location of the worst-performing joint**

### 4.5.1 Soil

The Original OC4 jacket foundation is linear and clamped at the base without soil. The soil profile of the site selected in the North-sea was modelled in Genie and compared with the first four natural frequencies of the original model. Figure 4-12 shows that the natural frequency of all the modes is lower than that of the original model (similar behaviour is observed in Table 4-5). This phenomenon is because soil stiffness is lower, and the structural behaviour is more flexible; hence, the eigenvalue frequencies will be lower. The trend agrees with the findings of the study [145]. Figure 4-14 shows the damage of soil and non-soil models along with

the effect of marine growth (discussed later). The damage is higher when the soil nonlinearity is included in the model because of the lower stiffness and higher amplitude vibrations.

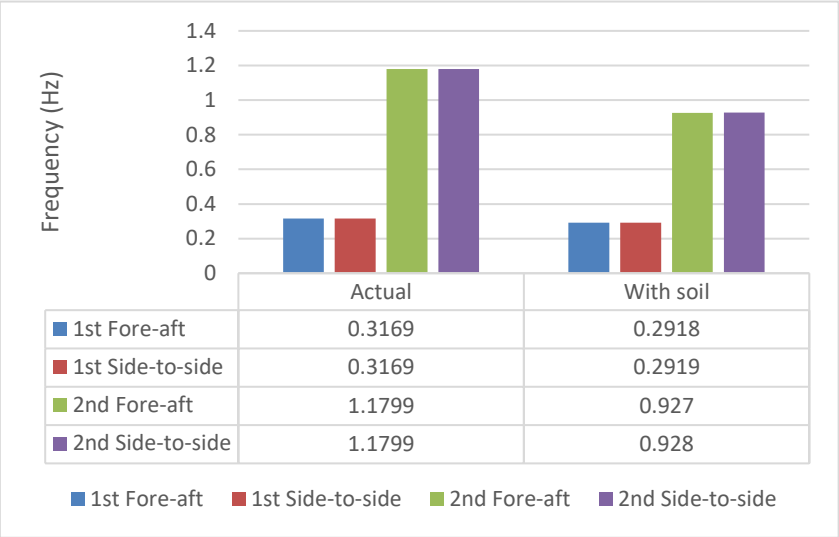



**Figure 4-13: Dynamic response with and without soil**

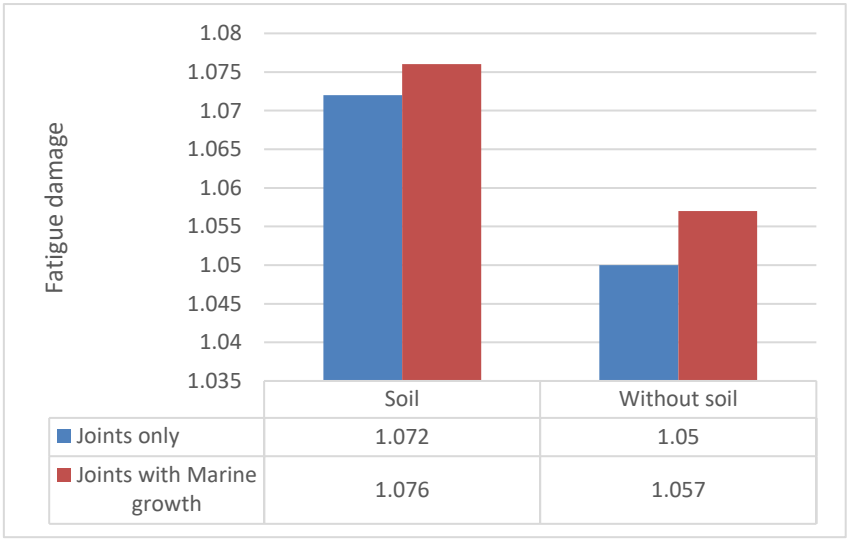
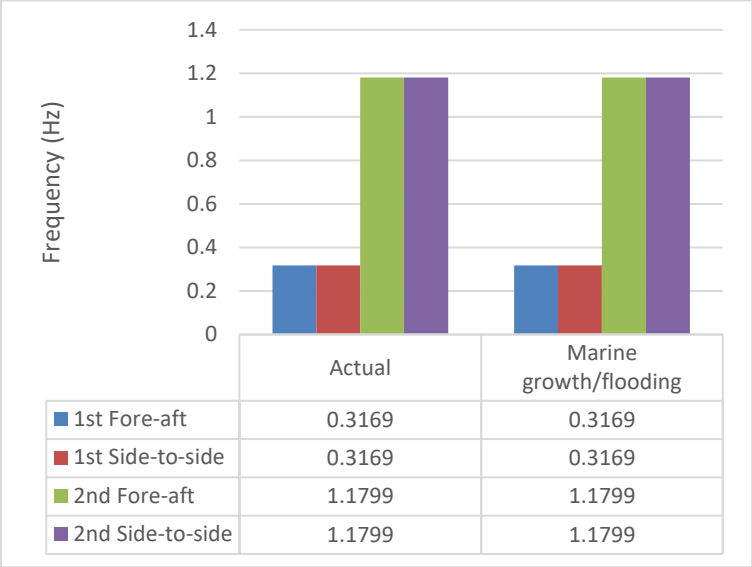



**Figure 4-14: Fatigue damage showing the effect of soil and marine growth**

### 4.5.2 Marine growth

Various marine growth mechanisms develop in the submerged jacket members, affecting the structural response because of the added structural area and the

change in surface roughness. The marine growth was introduced in the model from the water depth of 2 to 40 m, with an increased density of 1100 kg/m$^3$ and thickness of 100 mm as per the guidelines of the DNV standard. It is observed that adding the marine growth has not changed the stiffness (Figure 4-15), and the effect on fatigue life (Figure 4-14) is not significant either. The fatigue damage is greater possibly because the increased member diameter can generate higher drag loads..



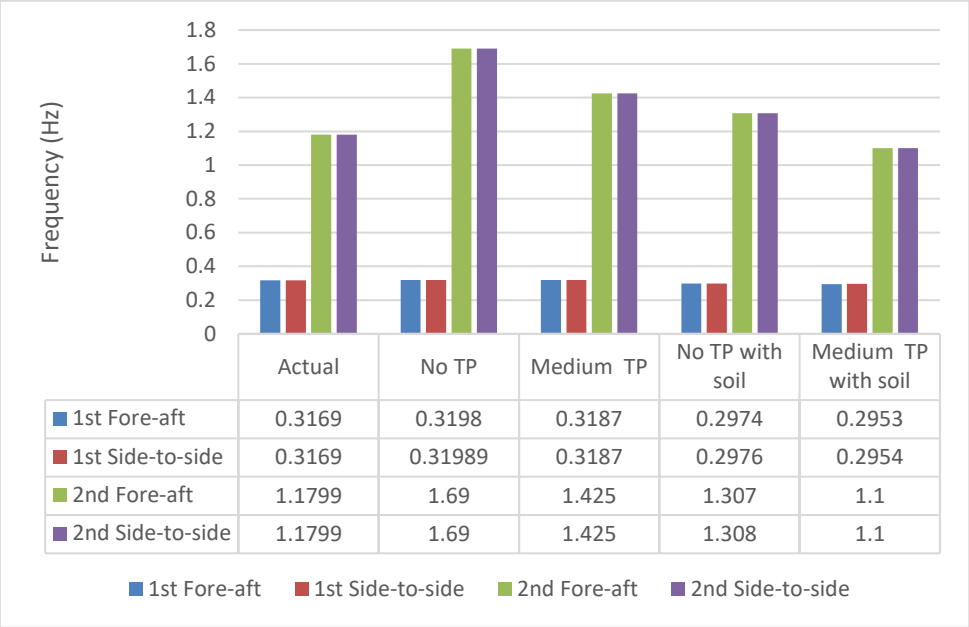

| | Actual | Marine growth/flooding |
|---|---|---|
| 1st Fore-aft | 0.3169 | 0.3169 |
| 1st Side-to-side | 0.3169 | 0.3169 |
| 2nd Fore-aft | 1.1799 | 1.1799 |
| 2nd Side-to-side | 1.1799 | 1.1799 |

**Figure 4-15: Dynamic response with/without marine growth**

### 4.5.3 Transition piece

A Transition Piece (TP) connects the jacket foundation with the tower, and its design significantly affects the dynamic response and fatigue life. Two primarily used configurations are a stiff concrete block and a light frame design. The OC4 jacket foundation has a concrete TP, but Genie can not model a concrete block. The TP was modelled as a beam with increased stiffness and an added mass of 628107 kg to simulate a similar effect. Moreover, the impact of TP on dynamic response and fatigue is studied based on three configurations. The medium configuration has a mass of 314203 Kg, and No TP configuration excludes the point mass. An additional configuration was also studied by including Steel TP (actual stiffness), and its effect on fatigue life is discussed below.

The 1st and 2nd natural frequencies are close to the 1P and 3P rotor frequencies and are not impacted much by the change in mass (see Figure 4-16). This trend follows the findings given in [146]. However, the effect is significant on the 3rd and 4th natural frequencies.




| | Actual | No TP | Medium TP | No TP with soil | Medium TP with soil |
|---|---|---|---|---|---|
| 1st Fore-aft | 0.3169 | 0.3198 | 0.3187 | 0.2974 | 0.2953 |
| 1st Side-to-side | 0.3169 | 0.31989 | 0.3187 | 0.2976 | 0.2954 |
| 2nd Fore-aft | 1.1799 | 1.69 | 1.425 | 1.307 | 1.1 |
| 2nd Side-to-side | 1.1799 | 1.69 | 1.425 | 1.308 | 1.1 |

**Figure 4-16: Effect of transition piece on the dynamic response**

The FLS check shows that the higher mass increases the axial force and moments on the joints, hence increasing fatigue damage (Figure 4-17). It is also observed that the fatigue damage decreases significantly when the whole TP is made of steel. The damage is lower due to the lighter TP and the absence of irregular material change in TP, which reduces the stress on joints.

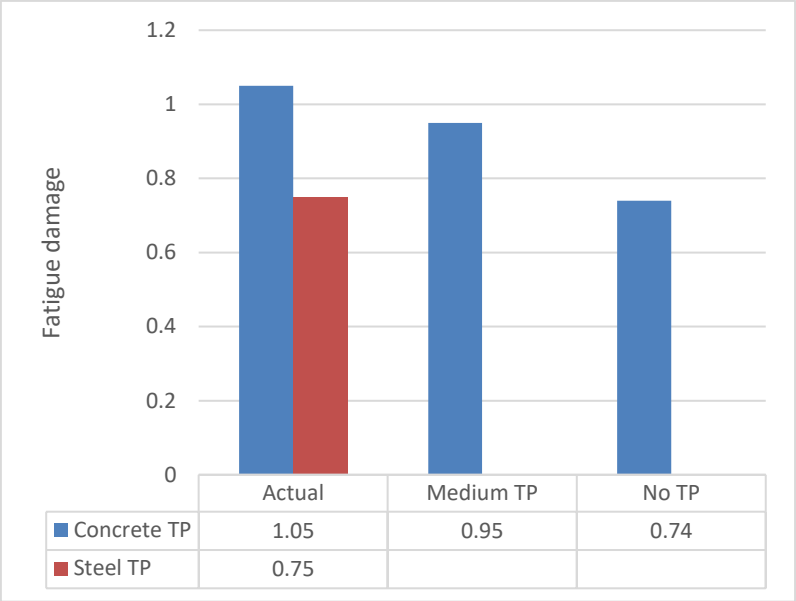



**Figure 4-17: Effect of transition piece on the fatigue damage**

### 4.5.4 Scour

Seabed scour occurs near the intersection of piles with the soil. The structural geometry, fluid flow, and seabed conditions govern Scour. The study assumes that the scour has already formed and does not investigate the phenomena of scour formation because it is outside the scope of this study. Three different configurations of scour are considered, which affect the values of spring stiffness showing the soil model.

Scour can affect the structural integrity because the jacket's embedded area is lower, resulting in lower support. This phenomenon results in lower stiffness and eigenvalue frequencies. Figure 4-18 shows that the effect is insignificant on the first fore-aft and side-to-side frequencies. However, there is a reduction in the third and fourth eigenvalue frequencies. There is a 0.70%, 1.32%, and 3.20% reduction for 0.5 m, 1 m, and 2 m scour, respectively.

As expected, the lower support produces greater damage to the structure. The damage increases with the scour size (see Figure 4-19) as the stress range increases. It is worth noting that the increase in the damage with the scour size is not steep. Few soil types (low cohesion) can produce significant damage if the

scour phenomenon is not mitigated. This asks for the need to perform frequent scour prevention and mitigation measures [146].

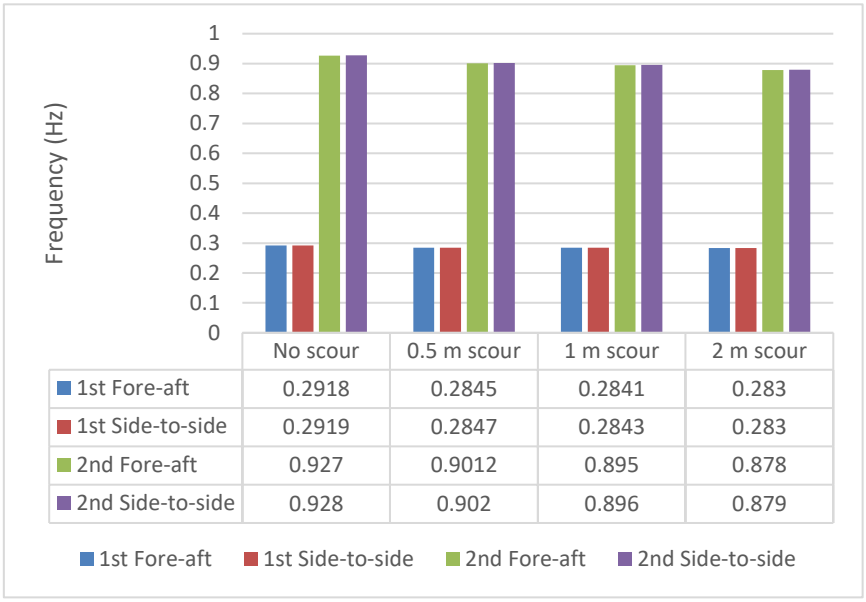
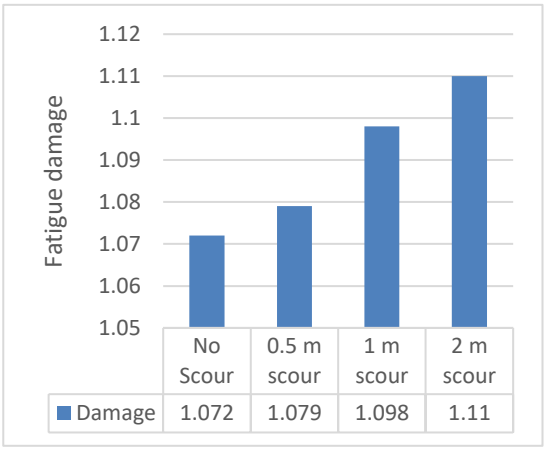
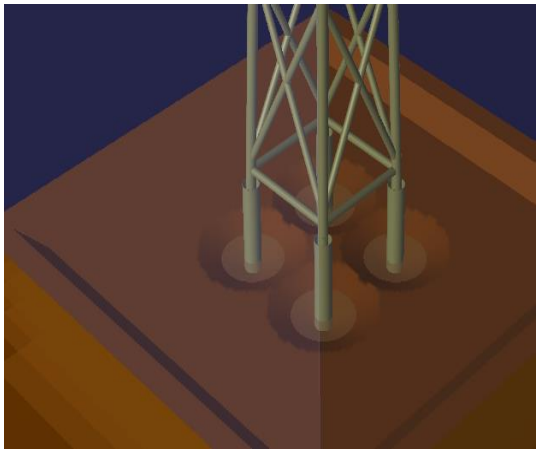



**Figure 4-18: Effect of scour size on the dynamic response**



(a) Effect of scour on fatigue (b) Scour visualization in Genie

**Figure 4-19: Visualization of scour and its effect on fatigue damage**

### 4.5.5 Grouted connection

The OC4 jacket foundation is cantilevered at the mudline with a grouted connection. The grouted connection consists of the pile, jacket leg, and the two tubular members, and these are connected with a grout material (density = 2000

kg/m$^3$) filled at each joint. The DNV standard DNVGL-RP-0419 [147] recommends two concepts for the grouted connection design, i.e., inclined pile in leg and leg in a pile (Figure 4-20). The inclined leg in the pile model has a pile diameter less than the leg, while the pile's diameter is greater than the leg in a pile model.

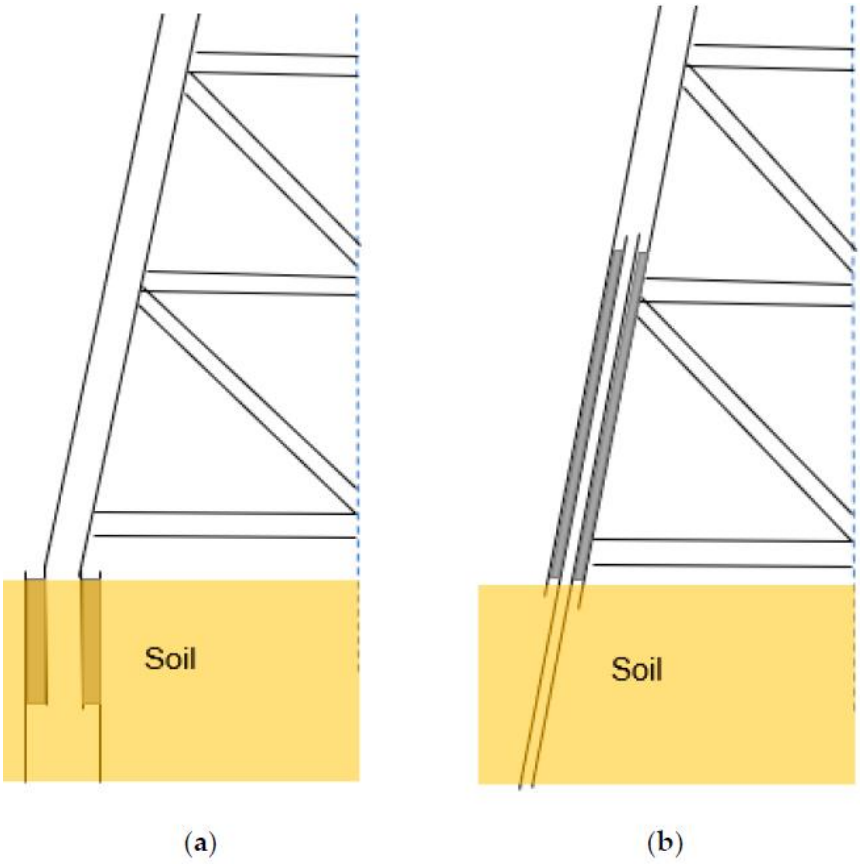



**Figure 4-20: Types of grouted connections. (a) Pile in leg. (b) Leg in pile**

The original design of the OC4 foundation has a leg in a pile configuration, and the length of the grouted connection is 4 m. Two modified configurations of grouted connections were simulated. In one model, the length of the grouted connection was increased to 6 m in the leg in a pile configuration, such that the hub height increased from 88.15 m to 90.15 m. The pile diameter was kept the same as in the original model (2.082 m). The second model has an inclined pile in leg configuration with a pile diameter of 0.9 m. The first two eigenvalue frequencies were not altered much in the leg in a pile model, but there was a decrease of 2.16% in the third and fourth natural frequencies (Figure 4-21).

However, there was a significant decrease in the eigenvalue frequencies in the inclined pile in a leg model. The first two natural frequencies were inside the 1P rotor frequency range, which is a soft structure, as discussed in [148] and [149].

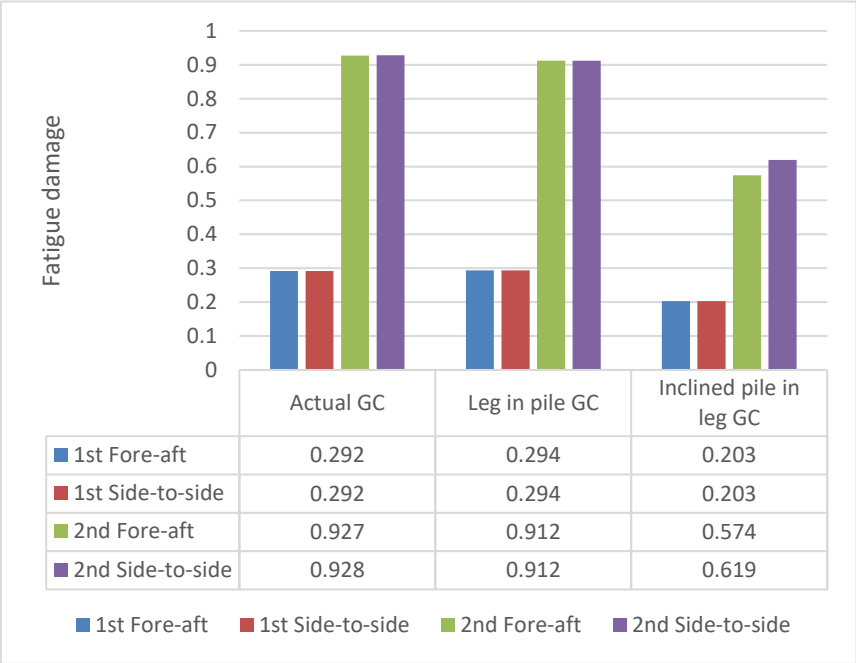



**Figure 4-21: Effect of grouted connection on the dynamic response**

The fatigue damage has considerably reduced for the leg in a pile configuration with an increased grouted connection size (Figure 4-22), which is expected because it has greater support at the bottom. However, the damage is considerably greater for the inclined pile in a leg configuration because the 1P frequency is closer to the natural frequency of the rotor. Moreover, the structure is also not stiff enough to provide good support. Another interesting observation was that the highest damage point was on an x-brace around the middle of the jacket (see Figure 4-12), which has moved to the braces at the bottom. Additionally, the damage at the previous point of reference has slightly increased to 1.08.

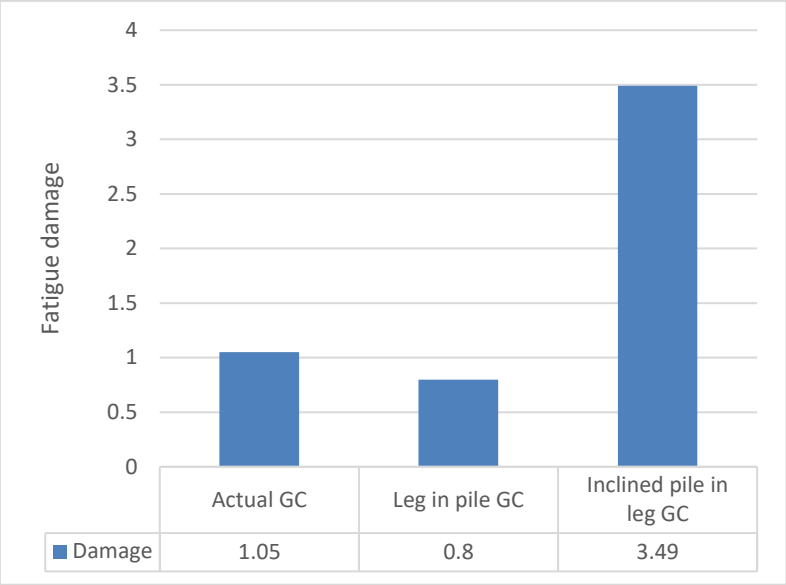



**Figure 4-22: Effect of grouted connection on fatigue damage**

## 4.6 Conclusions

In this chapter, the effect of different parameters on the structural response of the jacket foundation was observed in terms of dynamic response and fatigue life. The OC4 jacket foundation was developed in Sesam and validated with previous research. The validated model was converted to the superelement model and exported to Bladed, where it was attached to an NREL 5 MW wind turbine. The time-series wind and wave loads were simulated in Bladed to obtain the time-series loads. These time-series loads were exported to the SWM, where FLS analyses were performed. The steps were repeated by keeping identical wind/wave loads, and the effect of marine growth, nonlinearity of soil, transition piece's mass and material, scour size, and the length of grouted connection on the dynamic response and fatigue damage was observed by considering the life of 20 years. The fatigue damage of 1 implies a certain probability of fatigue cracking and there is no certainty of full crack development.

Marine growth was observed to have minimal impact on the structural dynamic response and fatigue damage. However, the nonlinearity of the soil had a significant effect on the dynamic response. The original OC4 jacket foundation had a fixed base, and the North Sea soil profile was incorporated into the model. The damage of the non-linear model was greater than the original model because

of the lower stiffness of the soil model, resulting in higher amplitude vibrations. The effect of nonlinearity was further extended to include the scour of different sizes (0.5 m, 1 m, and 2 m). Although the effect of scour size was insignificant on the first two natural frequencies, there was a reduction of 3.2% in the third and fourth natural frequencies for a scour of 2 m. The values were reduced by 0.7% and 1.32% for the scour sizes of 0.5 m and 1 m, respectively. The reduction in support due to scour caused an increase in damage. The effect of changing the design in the form of the transition piece and the grouted connection was also analysed. The TP with three mass configurations showed that the third and fourth eigenvalue frequencies change significantly, and an inverse relationship was observed between the mass and frequencies. However, the first two frequencies were not altered. The fatigue damage was greater for the heavier TP because of the higher axial force and moments on the joints, which resulted in higher stresses. The material selection between the concrete TP and steel TP showed the need to move to the lighter steel frames to extend the fatigue life.

A unique set of simulations was performed by increasing the length of the grouted connection from the original grouted connection size of 4–6 m for a leg in a pile configuration, which increased the hub height to 90.15 m. The overall effect was an increase in fatigue life because of the greater support. The design configuration was also changed to an inclined pile in a leg, reducing the first two eigenvalue frequencies near the 1P range. This resulted in a steep rise in fatigue damage near the lower part of the jacket. Marine growth has a minimum effect and can be ignored in terms of fatigue damage. However, the introduction of nonlinearity along with scour should be included to increase the accuracy of the results. Additionally, the study suggests that steel TP be adopted instead of concrete. The length of the grouted connection for a leg in a pile configuration can be increased to increase the fatigue life.

In conclusion, this chapter aimed to reduce the oversimplification often found in designs due to simulations' high cost and complexity. This research contributes to existing knowledge by analysing how a specific combination of design changes, transition piece material, and grouted connection impacts dynamic

response and fatigue life. Moreover, a detailed explanation of the advanced FLS analysis design was given, which uses the superelement approach. This technique is primarily used in industrial environments. The FLS analysis helps identify the weaker joints, and the damage parameter of 1 is considered a failure (in reality damage parameter of 1 shows the probability that a fatigue crack has developed). However, in reality, it shows that the crack has been initiated, and the structure has not failed. Future work may include crack propagation and fracture mechanics principles to study the actual failure of the joint.

The current chapter does not consider how changes in the diameter and thickness of the members and joints affect the jacket’s dynamic response and fatigue life. However, the next chapter will introduce a new approach to designing jackets using topology optimisation (TO) methodology. This methodology will generate a TO-optimised design based on the actual time series of environmental loads. The chapter will also discuss the impact of thickness and diameter on the TO-optimised jacket's dynamic response and fatigue life.

# 5 Fatigue Design of Offshore Jacket Foundation: Topology Optimisation Approach

Offshore wind turbines are frequently regarded as a pricey source of electricity, and efforts are being made to lower costs by developing novel and lighter offshore foundation designs. This chapter presents a topology optimisation method to obtain a novel jacket foundation design by finding the optimum load path on the structure to produce a lighter and cost-effective design. The OC4 jacket model was computationally simulated considering the Aero-Hydro-Servo-Elastic loads, and the topology optimisation method was used to obtain a series of new designs. The structural optimisation is performed based on the dynamic response of the jacket whilst restrained by relevant international design standards. In particular, time-domain fatigue simulations were performed to assess the structural integrity of the topology-optimised jacket for the first time. As a result, a range of optimised models with various thickness and diameter options are presented, which are rational and verify the optimisation procedure. The structural performance of the optimised geometry demonstrates the original jacket foundation is conservative, and the selection of optimised geometry achieved a mass reduction of 35.2% and simultaneously realized a 37.2% better fatigue life compared to the reference model. The overall optimisation procedure and results provide useful practicalities for designing offshore wind turbine foundations and potentially facilitate the relevant industry's structural integrity and cost reduction.

A version of this chapter has been accepted for publication in the Ocean Engineering journal

### 5.1.1 Topology optimisation workflow

ANSYS provides dedicated tools for SIMP optimisation based on finite element analysis models. This study uses the ANSYS Structural Optimisation module for the TO of the jacket foundation. The workflow (see Figure 5-1) for setting up and executing a SIMP topology optimisation study in ANSYS is discussed in the following sections.

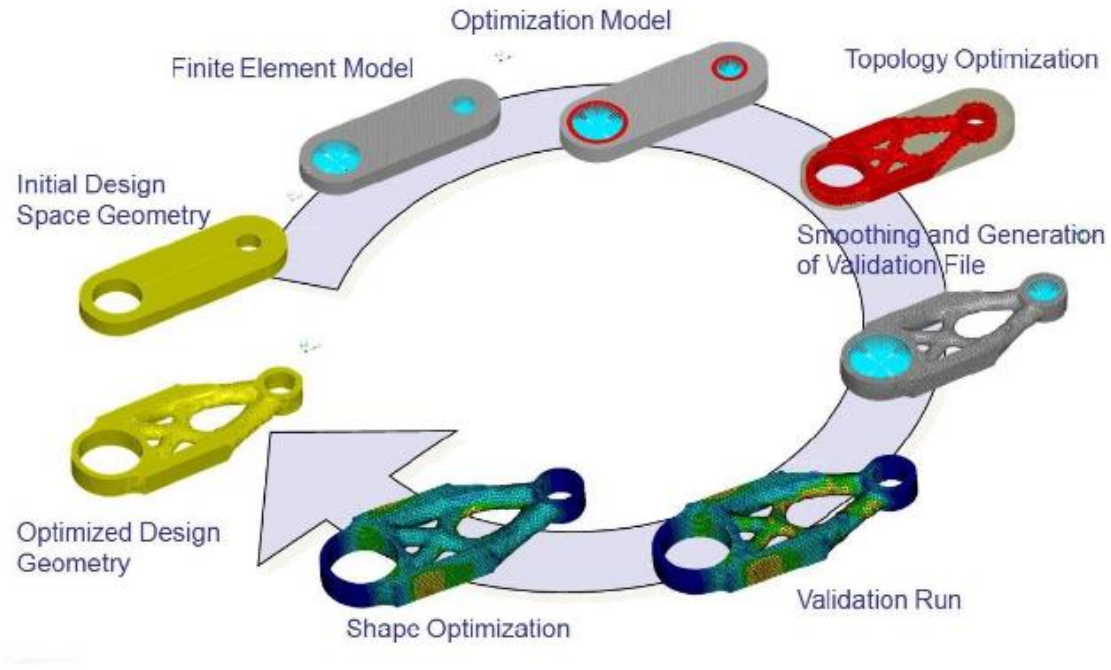



**Figure 5-1: Topology optimisation workflow (Adapted from** [150]**)**

#### 5.1.1.1 Model setup

A finite element model of the target structure needs to be created to initiate the topology optimisation process using the SIMP method in ANSYS. This model should include all the necessary geometric features, such as solid parts, void regions, and boundary conditions. In addition, during the model setup stage, certain design constraints are considered. These may include restrictions on maximum stress and displacement and considerations of the forces and pressures on the structure. Boundary conditions such as fixed supports and symmetries are also factored in, as well as any manufacturing constraints that may be relevant. Moreover, a design and a non-design region are also defined to

instruct the solver of the regions where material can not be removed. Figure 5-2 shows the design and non-design regions of a TO study performed on an aircraft's lever and shows that material is only being removed from the design region.

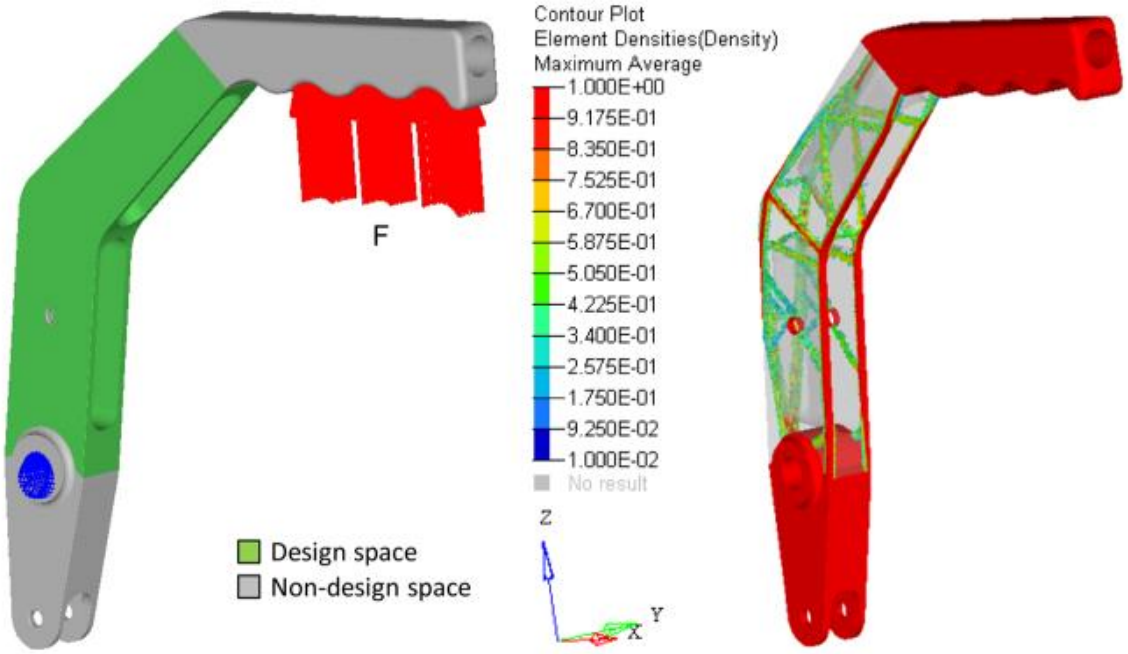



**Figure 5-2: Design and Non-design space of an aircraft's lever (Adapted from** [151]**)**

### 5.1.1.2 Objective function and constraints

The subsequent step involves formulating the objective function that requires optimisation. This function can involve minimizing compliance (maximizing stiffness), maximizing natural frequency, minimizing weight or residual stress, etc. In addition, there are design constraints that need to be considered. These constraints can include stress limits, displacement constraints, frequency constraints, or manufacturing constraints. These constraints are important to ensure the design meets the necessary engineering requirements.

### 5.1.1.3 Solver settings

The software is then configured with the necessary topology optimisation solver settings, such as the maximum number of iterations, the convergence criteria,

and the optimisation algorithm. ANSYS offers various optimisation options, such as density-based, level-set-based, lattice optimisation, and shape optimisation.

#### 5.1.1.4 Optimisation process

The optimisation process begins with a preliminary distribution of material density values and then continuously updates these values based on sensitivity information. At each iteration step, the software adjusts the density values to improve the objective function within the limits of the design constraints.

#### 5.1.1.5 Post-processing

Once optimisation is complete, the ANSYS software offers various tools for post-processing and visualizing results. It is worth noting that the TO simulation does not provide the final dimensions of the structure but instead gives the ideal flow path of the force. Post-processing takes the raw optimised geometry and transforms it into a CAD design that can be used for structural analysis through FEA to verify its performance. The optimisation process is iterative, and the user may need to adjust the penalty factor, convergence criteria, or other optimisation settings to achieve the desired results.

## 5.2 Methodology

A novel computational approach is established with a series of steps to optimise the existing model through TO and enhance fatigue life and material utilisation amount. The framework of the process and the use of different software modules are summarized in Figure 5-3.

The base model generated in Genie is exported to the Bladed as a superelement model where it is attached to the NREL 5 MW wind turbine. The output of this process is a time series of loads in the interface load file. The maximum value of the loads from the interface load file and the hydrodynamic loads obtained from the Genie are later used in ANSYS for TO.

A design and a non-design region are modelled in ANSYS, and the material is only removed from the design region (blue colour) shown in Figure 5-7. The mesh is generated and the loads calculated in the previous step are applied. After the definition of constraints and objective functions, the simulation is performed to obtain a topology-optimised jacket. The model is reconstructed in Sesam and later attached to an NREL 5 MW wind turbine to obtain time-series loads. These loads are then simulated in the SWM to obtain the fatigue damages for the optimised jacket.

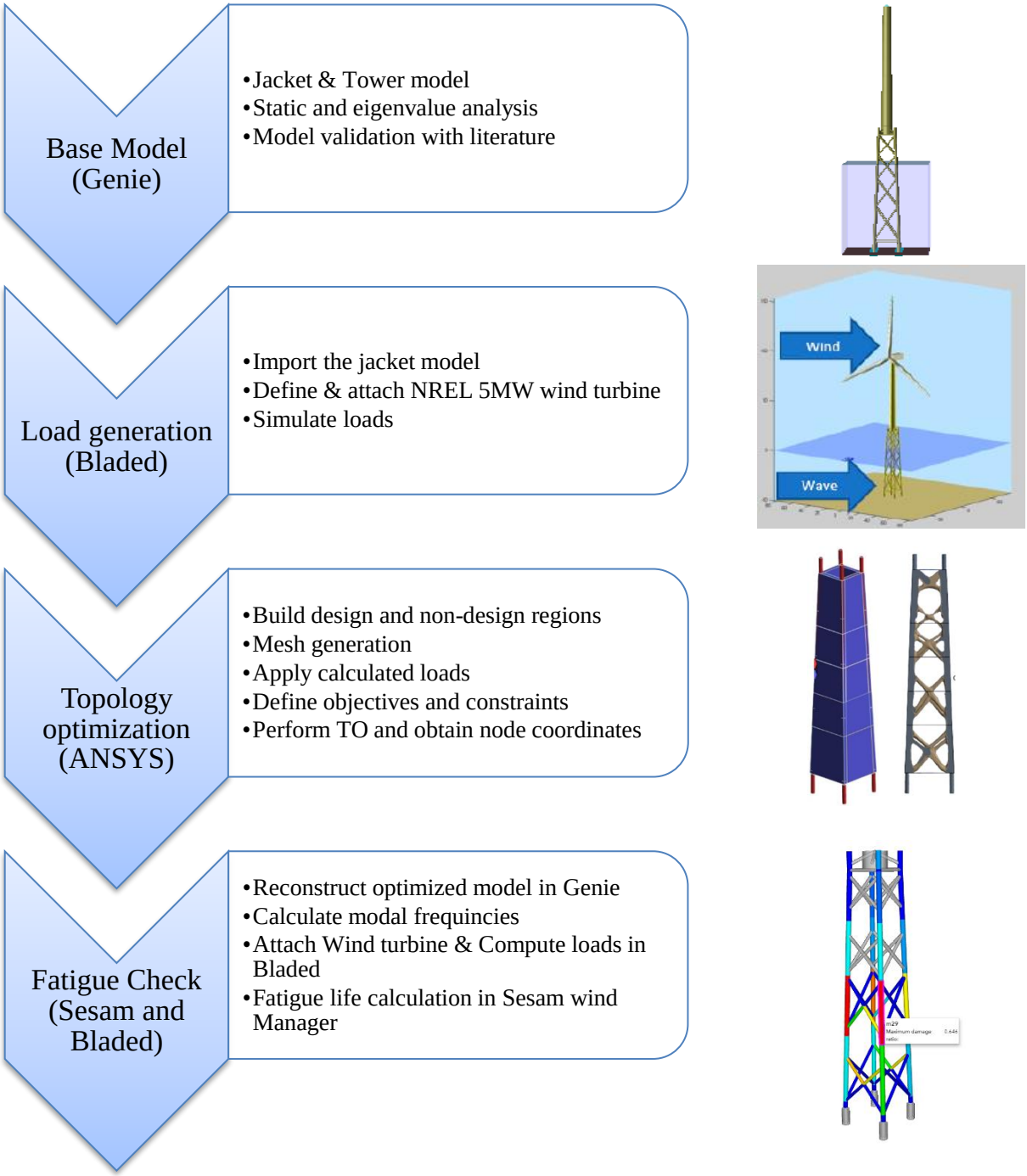



**Figure 5-3: Flowchart of computational approach**

### 5.2.1 Base model

The NREL 5 MW wind turbine and an OC4 jacket foundation were selected for the analysis due to their widespread usage and the availability of publicly accessible data. The details about the model and model validation were

discussed in section 4.2. Additionally, Table 4-2 and Table 4-3 provide information on the NREL 5 MW wind turbine and OC4 jacket foundation models, respectively. The analysis was performed using the environmental data of the K-13 deep water site in the North Sea given in Upwind Design Basis [128]. The environmental data is discussed in the previous section and is given in Table 4-1.

### 5.2.2 Load calculation

TO is particularly useful when the loading conditions are complex, as in the case of OWT, where the structure is affected by the aerodynamic loads and thrust loads on the rotor, aerodynamic loads from the tower, aerodynamic and hydrodynamic loads faced by the foundation, complex transition of loads from the TP and non-linear soil-pile interaction. The wind loads encountered by the tower are calculated using Equation 5-1, and hydrodynamic loads can be calculated using Morison's equation (see Equation 2-15). The equation helps calculate loads per unit length of the structure and combines drag and inertia forces

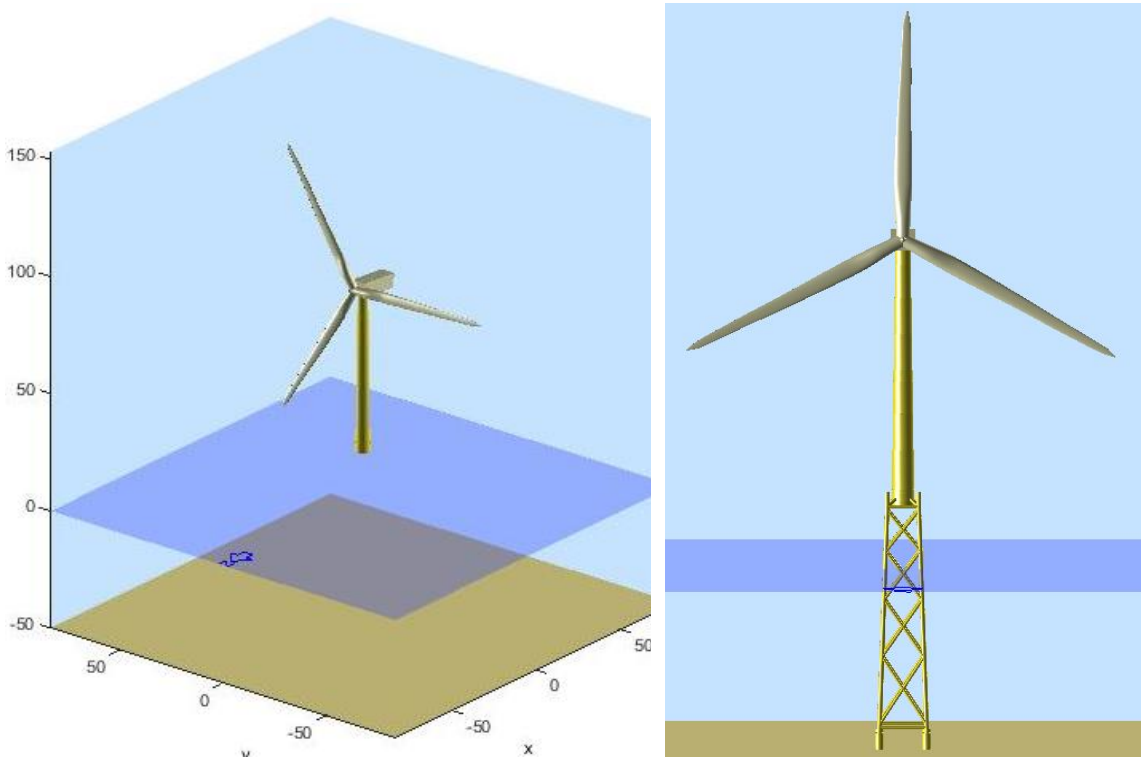
$$\boldsymbol{F_{twr}(z) = {}^{1}/_{2}\,\rho_a C_{D,T} V_i^2(z) D(z)} \qquad \textbf{5-1}$$

Where $C_{D,T}$ shows the tower's drag coefficient, D(z) represents the tapered diameter of the tower at any height z, $V_i$ represents the wind speed at hub height, and $\rho_a$ indicates the density of the water.

Aero-Hydro-Servo-Elastic simulations are complex and capture the complex dynamic behaviours of different components of the OWTs. These simulations provide a dynamic response of the structure under the complex combination of structural, aerodynamic, and hydrodynamic loads. The simulations include the aerodynamic loads experienced by the rotor resulting from airflow, the hydrodynamic forces exerted on the offshore foundation, and the Servo-Elastic component, which involves the control system responsible for adjusting the wind turbine's operation within varying wind speeds and shutting it down beyond a specified cut-off wind speed. Furthermore, the simulation involves the structural response of the system, including vibrations, deflections, loads, and moments of the structure. In the previous studies related to TO, the loads are calculated analytically, and the integrated dynamic behaviour of the system has been

ignored. The wind loads in this study are calculated using the DNV Bladed software, which is a wind turbine design tool offering aero-hydro-servo-elastic simulations for the OWTs. Moreover, it also helps in modelling a real wind turbine with accurate mass, location of the components, and blade profile. The complex Bladed simulation helps capture the model's multi-physics and holistically simulate the model [143].

The jacket foundation model was generated in the Genie module of Sesam. The software allows the simulation to be performed using an integrated or superelement approach. In an integrated approach (used by [127], [142]), the tower model is also modelled along the jacket and exported to the DNV Bladed software to calculate the aerodynamic loads. However, only the jacket model is exported to the Bladed software along with the wave data to calculate the aerodynamic loads. The aero-hydro-servo-elastic simulation and the controller design methodology were discussed in detail in Section 4.4.1.2. Figure 5-4 shows the visual differences between Bladed's superelement and integrated models.




(a) Superelement model (b) Integrated model

**Figure 5-4: Comparison of integrated and superelement models in Bladed**

The extreme loading conditions with the 50-year return period given in Table 4-1 are used to generate a design that can handle extreme conditions. The output of Bladed simulations is the time series of forces and moments in the x,y, and z directions. The maximum value of these loads in each direction is listed in Table 5-1.

**Table 5-1: Aerodynamic loads (50 years return period)**

| $F_x$ (kN) | $F_y$ (kN) | $F_z$ (kN) | $M_x$ (kNm) | $M_y$ (kNm) | $M_z$ (kNm) |
|---|---|---|---|---|---|
| 488 | -132 | -5480 | 9118 | 33739 | -1668 |

The hydrodynamic loads and the wind loads on the jacket were calculated in Genie by applying the environmental conditions with a 50-year return period. The designers select the 50-year return period to ensure that the OWTs can withstand the extreme loading conditions that may occur once in 50 years to achieve better structural integrity. Only the maximum load was calculated since the hydrodynamic load varies at a given wave period. The output is a line load that varies with the water depth and is given in Figure 5-5. Moreover, the wind load on the jacket is 3800 N/m.

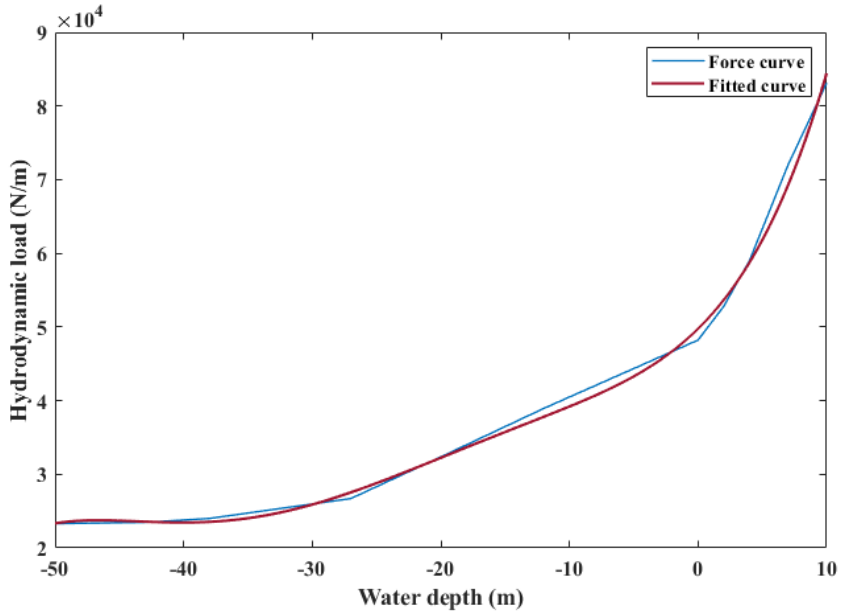



**Figure 5-5: Extreme hydrodynamic loading curve in a 50-year return period**

### 5.2.3 Topology optimisation process

TO of the jacket foundation was performed using ANSYS software. It has been decided that the jacket will have four legs, and the brace design will be improved. Figure 5-7 compares the original model with the TO design space in ANSYS. The structure was modelled as a continuum design space, and the legs' geometry was taken from the original model. Only the continuum design space will participate in the TO (Blue region), while the legs will only contribute to the overall structural stability (red region). The internal area of the jacket was also removed to ensure that the design was consistent with the original model. The tower, RNA, and TP masses are combined and act as a point mass on the jacket's interface node. Aerodynamic forces and moments are also applied at the top of the jacket. Moreover, sufficient mesh quality was ensured because it can greatly impact the accuracy of the optimised structure. The jacket legs are thin, and a mid surface was extracted to achieve a better mesh.

A TO approach mainly aims to save cost by reducing mass without compromising structural integrity. The maximum displacement constraint is introduced at the interface node of the jacket to achieve maximum stiffness, as given in Equation 5-2.

$$\boldsymbol{d_{max} = d} \qquad \textbf{5-2}$$



**Figure 5-6: 3D display of the meshed model**

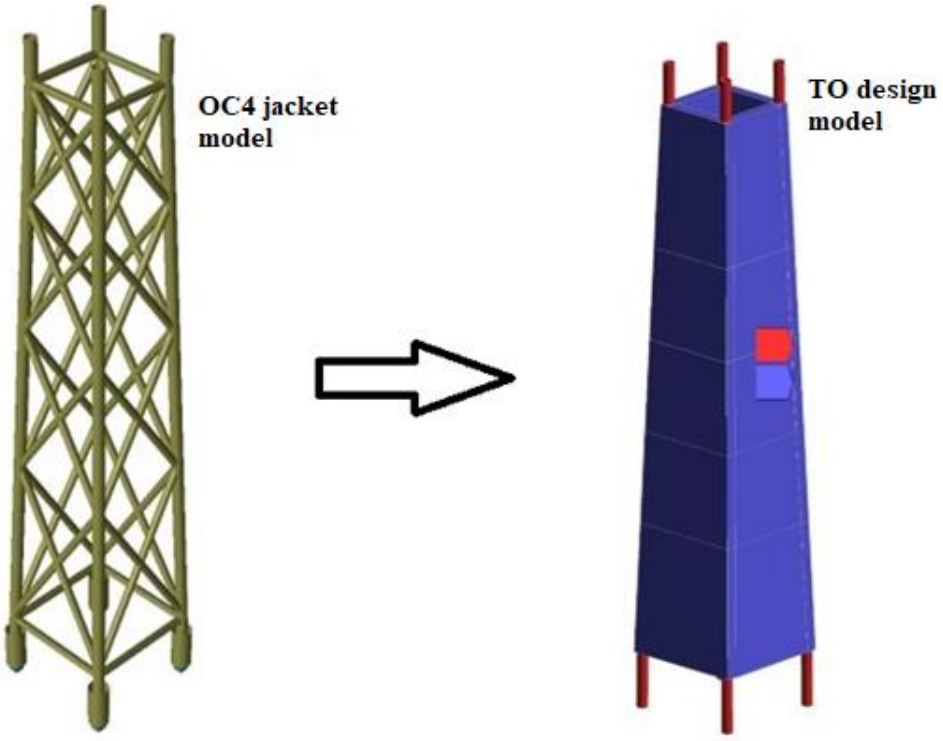



**Figure 5-7: Representation of OC4 jacket model and TO design space**

Where d is the allowable displacement of the jacket's interface node, and $d_{max}$ is the maximum displacement of the interface node. The stiffness increases because the structure is not allowed to displace as it normally would in the absence of constraint under a specific loading condition. Typically, the maximum displacement of the jacket is kept under 1/200 of the jacket height [92]. The maximum allowable displacement in this study is constrained at 0.15 m. In addition, the stress is limited by a design constraint, and the upper limit is the yield strength of the jacket (see Table 4-3).

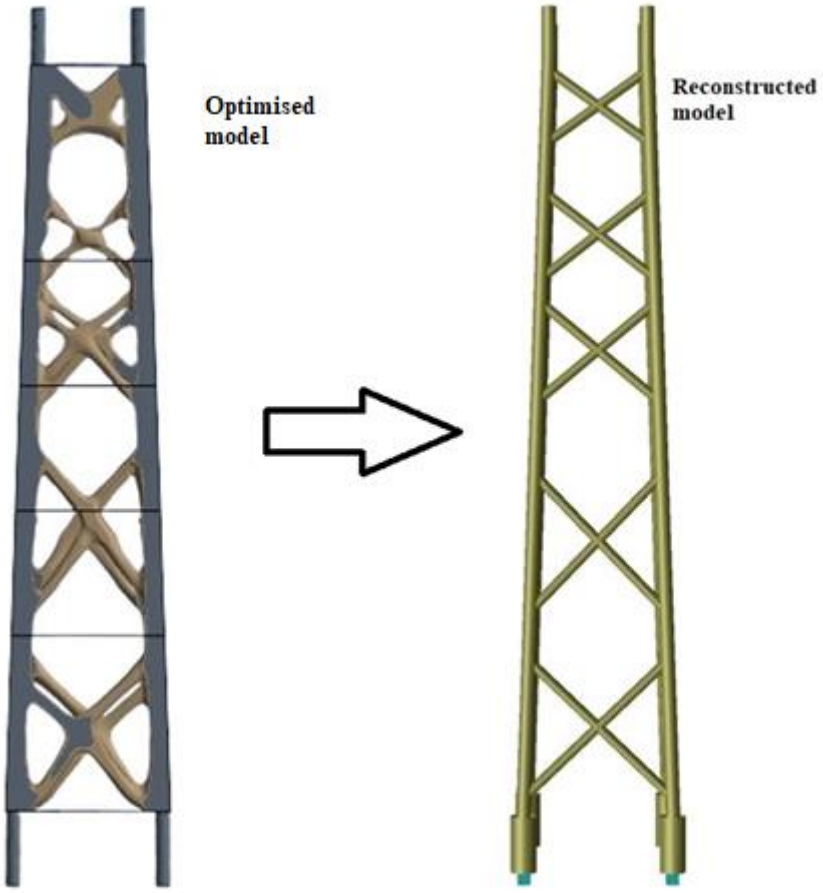



**Figure 5-8: Reconstructed model in Genie**

The TO algorithm may develop designs with small non-manufacturable components, so a manufacturing constraint of minimum member size (1.4 m) was introduced, which also helps achieve a truss-like structure. The objective function is to minimize compliance (increase stiffness) with a displacement formulation type. A response constraint is also introduced to achieve 35% of the original mass

of the optimisation region. Finally, a design constraint with cyclic repetition having four sectors was introduced to achieve a uniform design on all sides.

In FEA, 2D elements can be used for thin structures whose thickness dimension is considerably smaller than the other 2 dimensions. Such a thin structure can be meshed using a midsurface with a thickness property assigned to it. The legs in the jacket are quite thin and are meshed using a midsurface. The side walls of the model (design region) are modelled using 3D elements. The number of elements on the sides and four legs is 201920 and 36146 respectively, with an element size of 0.25 m. The mesh generated for the FEA model is shown in Figure 5-6

After 174 computationally intensive iterations, the solution converged, yielding a 5-tier x-brace jacket instead of a 4-tier OC4 jacket. It is worth noting that the final shape of the TO is not the final product; it just gives the optimum load path for the jacket. The term optimum load path in the TO refers to the path that forces may take within a structure that the structure can withstand while simultaneously minimising the material usage. The final shape needs to be reconstructed in Genie as seen in Figure 5-8. Furthermore, the final shape is not constrained by equal distance and angle between the braces, as is the case for the original model that follows DNV and API standards [54], [152]. Figure 5-9 demonstrates that the retained region of the optimisation domain increases after each iteration until the defined objective criteria are met. Table 5-2 compares the height coordinates of each brace to the original model.

**Table 5-2: Location of braces in OC4 and optimised model**

| Variable | OC4 locations (m) | Optimised model locations (m) |
|---|---|---|
| Z1 | 15.6 | 15 |
| Z2 | 4.3 | 9 |
| Z3 | 4.4 | 5 |
| Z4 | -8.8 | -2 |

| | | |
|---|---|---|
| Z5 | -8.9 | -4 |
| Z6 | -24.5 | -12 |
| Z7 | -24.6 | -18 |
| Z8 | -43.1 | -29 |
| Z9 | - | -33 |
| Z10 | - | -44 |

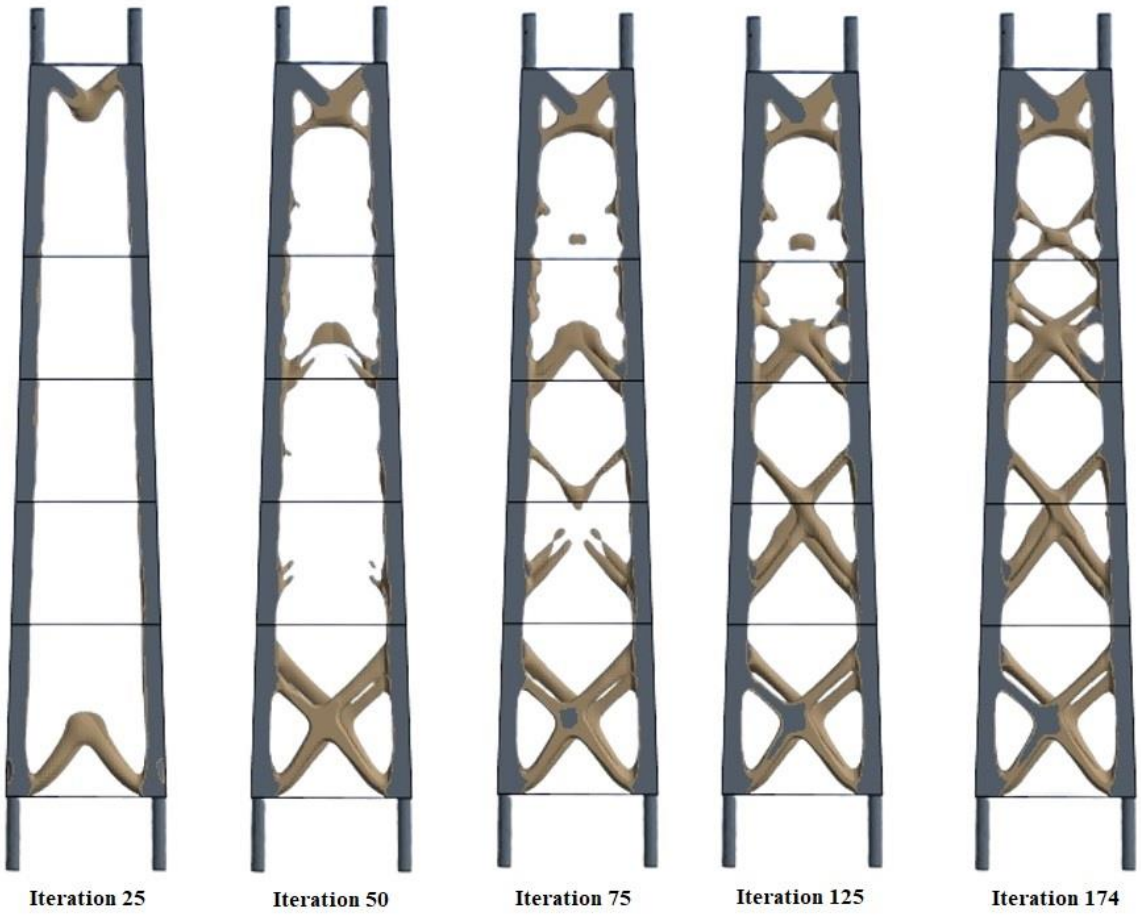



**Figure 5-9: Topology optimisation iterative process**

### 5.2.4 Superelement convergence

Before generating the superelement files, it is important to perform comprehensive checks for both spectral and spatial convergence to ensure that

the superelement closely resembles the original model's dynamic response. By confirming convergence in both domains, we can be certain that the superelement accurately reflects the behaviour of the original model during dynamic simulations and analyses. The process has been explained thoroughly in 4.4.1.1, while the following section will present the results for the optimised model.

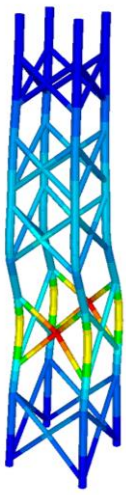
#### 5.2.4.1 Spectral convergence of the optimised model

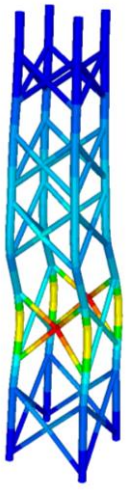
The boundary node of the model is located at the interface node, which contains 6 DOFs; hence, 40 DOFs are added to capture the dynamic response similar to the original model (see Section 4.4.1.1.1). Table 5-3 compares eigenvalue frequencies of the 40 vibration modes of the original and superelement models. The results demonstrate a high level of agreement between the two models, with the maximum difference observed in Mode 25 at just 1.11%, which indicates that the superelement accurately captures the dynamic behaviour of the original model. Figure 5-10 visually compares the Mode 10 and Mode 25 of the original and superelement models, reaffirming the reliability of the superelement model for fatigue life simulations.

**Table 5-3: Superelement convergence of the optimised model**

| Mode number | Original model freq. (Hz) | Superelement model freq. (Hz) | Difference (%) |
|---|---|---|---|
| 1 | 0.8015 | 0.8015 | 0.00 |
| 2 | 0.8015 | 0.8015 | 0.00 |
| 3 | 3.3098 | 3.3152 | -0.16 |
| 4 | 5.7971 | 5.8374 | -0.70 |
| 5 | 5.9062 | 5.9069 | -0.01 |
| 6 | 5.9062 | 5.9069 | -0.01 |
| 7 | 8.7487 | 8.7487 | 0.00 |
| 8 | 9.6703 | 9.7165 | -0.48 |
| 9 | 9.7761 | 9.7776 | -0.02 |
| 10 | 9.7761 | 9.7776 | -0.02 |
| 11 | 12.8652 | 12.8652 | 0.00 |
| 12 | 13.3253 | 13.4428 | -0.88 |
| 13 | 13.7593 | 13.7593 | 0.00 |
| 14 | 14.2288 | 14.2288 | 0.00 |

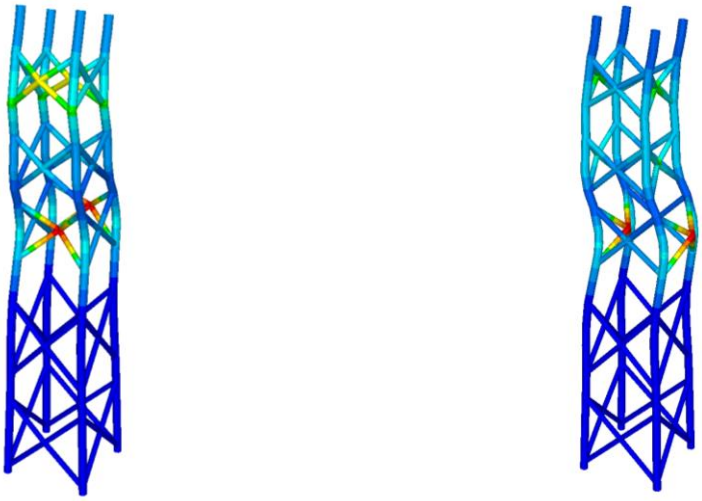
| | | | |
|---|---|---|---|
| 15 | 14.2289 | 14.2289 | 0.00 |
| 16 | 16.5040 | 16.5040 | 0.00 |
| 17 | 17.9899 | 17.9910 | -0.01 |
| 18 | 18.2714 | 18.2714 | 0.00 |
| 19 | 18.3897 | 18.3898 | 0.00 |
| 20 | 18.9131 | 18.9175 | -0.02 |
| 21 | 19.6353 | 19.6367 | -0.01 |
| 22 | 19.6363 | 19.6377 | -0.01 |
| 23 | 20.0086 | 20.0086 | 0.00 |
| 24 | 20.3120 | 20.3813 | -0.34 |
| 25 | 20.3120 | 20.5376 | -1.11 |
| 26 | 20.3797 | 20.5376 | -0.77 |
| 27 | 20.7263 | 20.7263 | 0.00 |
| 28 | 21.2117 | 21.3901 | -0.84 |
| 29 | 21.2117 | 21.3901 | -0.84 |
| 30 | 21.5177 | 21.6140 | -0.45 |
| 31 | 21.5177 | 21.6141 | -0.45 |
| 32 | 23.4945 | 23.4945 | 0.00 |
| 33 | 23.4989 | 23.4989 | 0.00 |
| 34 | 25.4356 | 25.4356 | 0.00 |
| 35 | 26.3531 | 26.3531 | 0.00 |
| 36 | 28.0933 | 28.1081 | -0.05 |
| 37 | 28.8527 | 29.1087 | -0.89 |
| 38 | 29.1217 | 29.1281 | -0.02 |
| 39 | 29.1275 | 29.4448 | -1.09 |
| 40 | 29.1765 | 29.4460 | -0.92 |





(a) Mode 10 (9.7761 Hz)-Original model

(b) Mode 10 (9.7776 Hz)-Superelement model with 46 DOF



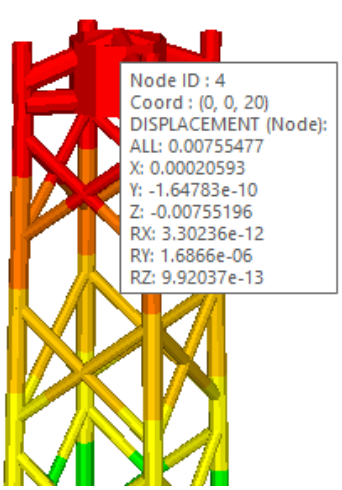
(c) Mode 25 (20.312 Hz)-Original model

(d) Mode 25 (20.5376 Hz)-Superelement model with 46 DOF

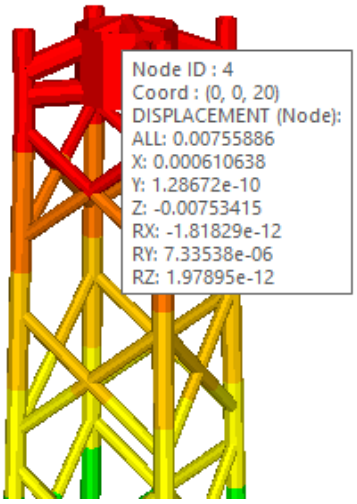
**Figure 5-10: Spectral convergence of Mode 10 and Mode 25**

#### 5.2.4.2 Spatial convergence of the optimised model

In addition to showing similar natural frequencies, the superelement model must show comparable structural responses when subjected to equivalent loading conditions. Figure 5-11 compares displacement at the optimised model's interface node between the original and superelement models at t = 25s of the simulation. The results demonstrate a strong similarity in their displacement characteristics, with both models exhibiting closely matched behaviour. In conclusion, the superelement of the topology-optimised model has achieved both spectral and spatial convergence.




(a) Displacement at interface load of the original model




(b) Displacement at interface node of the superelement model

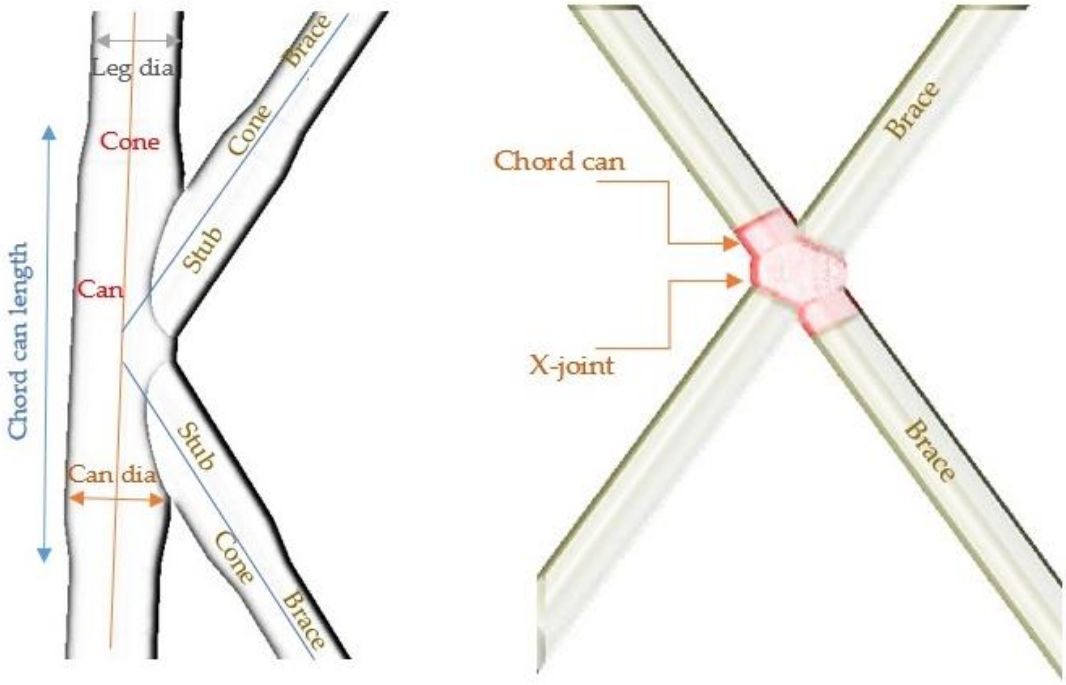
**Figure 5-11: Spatial convergence of the optimised model**

### 5.2.5 Fatigue damage calculation

Properly defining joints is critical in fatigue calculation based on the hotspot stress approach. A joint is a sophisticated concept encompassing information about the structural joint and details of reinforcement data in cans and stubs. For a typical joint, an increase in the yield strength or wall thickness/diameter is increased for the chord as reinforcement. When the members have equal diameters, the thickness of one member is augmented to function as a toughness member, while the other members are considered minor members [153]. Moreover, when two or more members possess similar wall thicknesses, the member with the larger diameter is designated as the toughness member.

The joint concept is mostly introduced as a can and stub for a welded tubular joint, where a can normally has a larger diameter and acts as a toughness member, and a stub is a smaller diameter section that acts as a secondary member. API [56] and NORSOK [154] standards have outlined some rules for the joint design, which are followed in the offshore wind, and oil and gas industries. The standards suggest that the minimum can length should be a minimum of one-fourth of a chord diameter, or 0.3 m. Similarly, stub length can be the same as stub diameter and should not exceed 0.6 m. This study has

followed the rules suggested by the standards, and all the requirements for can/stub lengths, minimum gap, and cone dimensions were followed. Moreover, the toughness member was introduced on the x-joints as an increase in thickness, while a combination of an increase in thickness and diameter has been used for other joints. Figure 5-12 visually represents the joint concept for a K joint and an X joint.




(a) K-joint (b) X-joint

**Figure 5-12: Visual representation of joints and locations of cans/stubs**

The locations of each x-brace were found from the topology-optimised model, and the model was reconstructed in Sesam's Genie module (See Figure 5-8). The modified model's modal frequencies and static deflections were computed to compare with the original model and to see if the resonance zone was avoided. Sesam Wind Manager (SWM) generated the superelement model, which was then exported to Bladed. The aero-hydro-servo-elastic loads were calculated in Bladed by attaching an NREL 5 MW wind turbine, and these loads were imported into the SWM to calculate fatigue damages. The damages were calculated using

the Framework module of the SWM using the S-N curve method. The estimation of member damages was based on the DNV2010_D S-N curve, while the computation of damages on the tubular joints utilised the DNV2010_T curve. These S-N curves are given in the DNV-RP-C203 standard [55], which provides recommendations for the fatigue design of offshore structures and helps choose the right S-N curve for different conditions and materials (see Figure B-1, Figure B-2, and Figure B-3).

Moreover, a splash zone was also defined, which serves a specific purpose. SWM ensures that the S-N curve without cathodic protection is applied above the splash zone. To accurately capture the effects of corrosion and protect the structure, two different S-N curves are applied based on the presence or absence of cathodic protection.

Above the splash zone, where the structure is exposed to atmospheric conditions without cathodic protection, the software applies the appropriate S-N curve for this scenario. This accounts for the accelerated fatigue damage caused by corrosion and other environmental factors in this zone. Underwater, where cathodic protection is active, a different S-N curve that considers the protective effects of cathodic protection is used. This indicates the reduced impact of corrosion on the structure in the submerged region. By incorporating the splash zone and distinguishing between different S-N curves based on cathodic protection, this analysis provides a comprehensive and realistic assessment of fatigue life for the offshore structure.

Furthermore, fatigue damages are cumulatively accrued over 20 years. The software continuously calculates the accumulated damage for each member or joint based on applied loading and stress conditions. Once a specific member or joint reaches a critical threshold of one, it is considered to have reached failure.

## 5.3 Results and discussion

### 5.3.1 Parametric models

To enable precise fatigue life calculations and comparisons, the initial OC4 jacket model was modified by defining the joints with the addition of cans and stubs. The original OC4 jacket mass, excluding the joints, was 674 tonnes. By increasing the thickness of the joint components (cans/stubs) by 5 mm, the total mass increased to 718 tonnes. This adjusted model was first verified through eigenfrequency analysis. The inclusion of detailed joint specifications allowed for a more accurate assessment of fatigue damages across both the original and topology-optimised designs.

As the TO generates an idealized load path without specifying member dimensions, a series of models with varying section thicknesses and diameters were developed to refine the optimised design. There are no specific instructions in the standards regarding the values of diameter or thickness. However, to ensure adequate strength, the offshore standards enforce limitations on the diameter-to-thickness (D/t) ratio. Norsok N-004 [154] and ISO19902 [42] suggest that D/t should be less than 120. Iterative model variations were created by modifying member thickness, diameter, and joint dimensions, keeping the D/t value below 120. The structural integrity of various models was evaluated by systematically reducing the jacket's dimensions, resulting in a gradual decrease in mass. The relative influence of thickness adjustments and combined thickness-diameter variation on fatigue life was examined by incrementally reducing member sizes to the point of failure.

Figure 5-13 visually represents the position of various jacket sections, while the location of cans/stubs was shown earlier in Figure 5-12. The dimensions of various sections used to examine the influence of thickness variation on fatigue damage are given in Table 5-4, and Table 5-5 presents the section properties used to examine the combined effect of thickness and diameter variation on fatigue life. The model name denoted by T indicates the models with thickness variation, and TD represents the models with thickness and diameter variation.

Additionally, the joint parameters are listed as the dimensions of joint cans and stubs (see Figure 5-12).

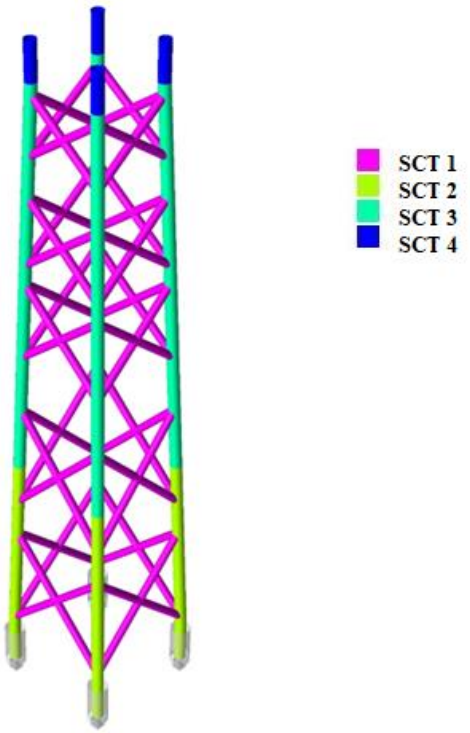



**Figure 5-13: Visual representation of the location of sections**

**Table 5-4: Section with thickness variation**

| Model name | Brace D, T (mm) | Leg Sct-2 D, T (mm) | Leg Sct-3 D, T (mm) | Leg Sct-3 D, T (mm) | Leg_Can D, T (mm) | Leg_Stub D, T (mm) | Brace_Can D, T (mm) | Mass (Tonne) |
|---|---|---|---|---|---|---|---|---|
| Original | 800,20 | 1200,50 | 1200,35 | 1200,40 | 1200,55 | 800,25 | 800,25 | 718 |
| T-1 | 800,25 | 1200,50 | 1200,35 | 1200,40 | 1200,50 | 800,25 | 800,25 | 705 |
| T-2 | 800,20 | 1200,40 | 1200,30 | 1200,30 | 1200,50 | 800,25 | 800,25 | 639 |
| T-3 | 800,18 | 1200,35 | 1200,25 | 1200,25 | 1200,50 | 800,25 | 800,25 | 573 |
| T-4 | 800,16 | 1200,30 | 1200,22 | 1200,22 | 1200,40 | 800,20 | 800,20 | 487 |
| T-5 | 800,16 | 1200,32 | 1200,23 | 1200,23 | 1200,42 | 800,22 | 800,22 | 515 |

| | | | | | | | | |
|---|---|---|---|---|---|---|---|---|
| T-6 | 800,15 | 1200,28 | 1200,21 | 1200,21 | 1200,38 | 800,18 | 800,18 | 465 |
| T-7 | 800,16 | 1200,24 | 1200,20 | 1200,20 | 1200,36 | 800,20 | 800,20 | 458 |

**Table 5-5: Sections with thickness and diameter variation**

| Model name | Brace D, T (mm) | Leg Sct-2 D, T (mm) | Leg Sct-3 D, T (mm) | Leg Sct-3 D, T (mm) | Leg_Can D, T (mm) | Leg_Stub D, T (mm) | Brace_Can D, T (mm) | Mass (Tonne) |
|---|---|---|---|---|---|---|---|---|
| TD-1 | 600,20 | 1000,40 | 1000,30 | 1000,30 | 1200,40 | 800,25 | 600,25 | 514 |
| TD-2 | 600,18 | 900,35 | 900,25 | 900,25 | 1250,40 | 850,25 | 600,25 | 495 |
| TD-3 | 550,16 | 800,32 | 800,25 | 800,25 | 1100,40 | 850,25 | 600,25 | 421 |
| TD-4 | 570,17 | 850,32 | 800,25 | 800,25 | 1100,40 | 750,25 | 600,25 | 430 |
| TD-5 | 570,17 | 850,32 | 820,25 | 820,30 | 1150,40 | 770,25 | 600,25 | 451 |
| TD-6 | 600,18 | 900,35 | 900,30 | 900,30 | 1200,38 | 800,23 | 600,23 | 469 |
| TD-7 | 600,17 | 850,32 | 850,30 | 850,30 | 1200,40 | 800,25 | 600,25 | 465 |

### 5.3.2 Dynamic behaviour

A typical characteristic of successful structural design is to modify the design parameters to optimise the stiffness-to-mass ratio to obtain an ideal design. As discussed in the previous section, different models were generated by varying the thickness, diameter, and joint design to study the effect on dynamic behaviour. A major requirement for a successful design is that the natural frequency of the optimised jacket should avoid the 1P and 3P frequency zones. The recommended practice is that the first two eigenvalue frequencies should be between 0.22 and 0.35 Hz, while higher-order eigenvalue frequencies should be greater than 0.605. The fore-aft and side-to-side frequencies refer to the natural frequencies in the longitudinal and transverse directions, respectively. Their values are mainly affected by structural stiffness and mass distribution. Table 5-6

shows the effect of the thickness of members and joints (cans/stubs) on the first four eigenfrequencies, while Table 5-7 summarizes the impact of the thickness and diameter of the members and joints on the dynamic response.

The optimised models had lower mass than the original OC4 jacket. Despite significant mass reductions, the first two natural frequencies were similar to the OC4 model. However, higher-order frequencies decreased substantially compared to OC4. This indicates the optimised models have slightly lower stiffness and may experience greater displacements from dynamic loads, consistent with prior jacket topology optimisation research [92]. Furthermore, reducing both thickness and diameter led to even lower natural frequencies due to decreased stiffness and mass.

It was observed that the TO successfully produced models with adequate stiffness by maintaining first and second natural frequencies within acceptable ranges. The reductions in higher-order frequencies are expected with lighter designs. The dynamic response analysis provides confidence that resonance issues are avoided in the optimised jackets.

**Table 5-6: Effect of thickness on the dynamic response**

| Model name | 1st fore-aft (Hz) | 1st side-to-side (Hz) | 2nd fore-aft (Hz) | 2nd side-to-side (Hz) |
|---|---|---|---|---|
| Original | 0.316 | 0.316 | 1.179 | 1.179 |
| T-1 | 0.318 | 0.318 | 1.05 | 1.06 |
| T-2 | 0.312 | 0.312 | 1.027 | 1.029 |
| T-3 | 0.302 | 0.302 | 0.996 | 0.999 |
| T-4 | 0.291 | 0.291 | 0.958 | 0.960 |
| T-5 | 0.294 | 0.294 | 0.969 | 0.971 |
| T-6 | 0.287 | 0.287 | 0.949 | 0.952 |
| T-7 | 0.283 | 0.283 | 0.941 | 0.943 |

**Table 5-7: Effect of thickness and diameter on the dynamic response**

| Model name | 1st fore-aft (Hz) | 1st side-to-side (Hz) | 2nd fore-aft (Hz) | 2nd side-to-side (Hz) |
|---|---|---|---|---|
| Original | 0.316 | 0.316 | 1.179 | 1.179 |
| TD-1 | 0.297 | 0.297 | 0.961 | 0.963 |
| TD-2 | 0.281 | 0.281 | 0.911 | 0.913 |
| TD-3 | 0.261 | 0.261 | 0.822 | 0.825 |
| TD-4 | 0.272 | 0.272 | 0.864 | 0.866 |
| TD-5 | 0.279 | 0.279 | 0.882 | 0.885 |
| TD-6 | 0.286 | 0.286 | 0.895 | 0.897 |
| TD-7 | 0.282 | 0.282 | 0.881 | 0.883 |

### 5.3.3 Fatigue damages

Performing fatigue analysis is a vital component in the design and operation of offshore wind turbine jacket support structures. The purpose is to evaluate the impacts of cyclic loading on the structure over its intended 20-year service life. For this research, comprehensive fatigue life calculations were conducted on the topology-optimised jacket models subjected to coupled dynamic wind and wave loading conditions.

The time-domain simulation results produced stress ranges that were processed using rainflow counting methods. Using Miner's rule, each joint and member's fatigue damage was quantified by cumulatively analysing S-N curves. A value of 1 indicates the initiation and failure of cracks but in reality, it only shows a probability that a fatigue crack has developed. The DNV2010_D curve was used to compute damages in the members, while the DNV2010_T curve was applied for tubular joints (see Figure B-1 and Figure B-3).

Varying certain jacket design parameters provided insights into their relative influence on fatigue performance. The first analysis focused exclusively on modifying the thickness of the members and tubular joints. Table 5-8 summarizes the fatigue damages and mass changes associated with different thickness adjustments. Model T-1 exhibits the lowest damage, indicating an estimated fatigue life of over 100 years. This suggests that the design of T-1 is excessively conservative compared to the original model, which has a fatigue life of approximately 36 years. While T-2 and T-3 achieved mass reductions of 11% and 20.19%, respectively, their fatigue lives indicated there was room for substantial mass reductions. By further reducing the thickness of the brace and legs, the T-4 model achieves a fatigue damage level comparable to the original model while achieving a significant mass reduction of 32.17%. In the T-6 model, the thickness of the brace reaches a point where it cannot be further reduced without compromising its fatigue life. Similarly, in the T-7 model, reducing the thickness of the legs further would result in a decrease in the fatigue life below the desired 20-year lifespan. Of all the thickness-based models, T-5 provided the most favourable balance between mass reduction (28.27%) and retaining adequate fatigue life after 20 years.

**Table 5-8: Effect of thickness variation on the fatigue damages**

| Model name | Fatigue damage | Failure location | Mass reduction (%) |
|---|---|---|---|
| Original | 0.51 | Brace-Joint | -- |
| T-1 | 0.098 | Leg-Joint | 1.81 |
| T-2 | 0.1 | Leg-Joint | 11 |
| T-3 | 0.15 | Leg-Joint | 20.19 |
| T-4 | 0.54 | Brace-Joint | 32.17 |
| T-5 | 0.31 | Brace-Joint | 28.27 |
| T-6 | 1.3 | Brace-Joint | 35.24 |
| T-7 | 1.03 | Leg-Joint | 36.21 |

The second set of analyses examined the combined effects of varying member thickness and diameter. As summarized in Table 5-9, the two-parameter optimisation enabled more significant mass reductions without sacrificing integrity. This approach permits an optimal balance between the required strength, stability, and mass reduction. Although the TD-1 model had comparable mass to T-5, its higher fatigue damage demonstrated the benefits of reducing member diameter in addition to thickness. The TD-2 model exemplified the advantages of this approach, achieving 31.05% mass reduction while also lowering fatigue damage due to damage due to its strengthened joints, enhancing both strength and durability.

In the models TD-3 and TD-4, leg members fail before the joints, showing that further mass cannot be reduced from the members, and the structure is failing sooner than 20 years. By increasing the diameter and thickness in the TD-5 model, the fatigue life has been extended; however, failure still originated in members rather than joints. Additional increases in cans/stubs and member diameters enabled TD-5 to meet the desired 20-year life. Further analysis suggested that mass reductions of around 35% were attainable if member diameters decreased while retaining near-original can/stub dimensions, as demonstrated by the TD-6 and TD-7 models.

Figure 5-14 shows the contour of the fatigue damages of the TD-7 jacket model. It is evident that the brace exhibits the most severe damage, with other braces also experiencing greater damage compared to the legs. Figure 5-15 provides a detailed view of the most critically damaged brace, revealing that the failure occurs at the x-joint of the brace. The fatigue damage on the chord of the x-joint measures 0.322, while the chord of the leg joint has a fatigue damage of 0.276. Additionally, the fatigue damage consistently shows higher values on the chord side than on the brace side.

The mass reduction could be obtained through the simplified process of thickness reduction only, but there is a scope for additional mass reduction if the diameter of the members is reduced with reinforced joints. Moreover, the accurate modelling of the joint plays a critical role in the extended design fatigue life of the

jacket foundation. Based on the analysis performed in this study, TD-7 was the best model as it offered 37.2% lower fatigue damage and around 35% mass reduction. Moreover, Model TD-7 achieves a considerably lower mass than the T-5 model, even though the fatigue damage levels are similar.

**Table 5-9: Effect of diameter and thickness variation on the fatigue damages**

| Model name | Fatigue damage | Failure location | Mass change (%) |
|---|---|---|---|
| Original | 0.51 | Brace-Joint | -- |
| TD-1 | 0.35 | Brace-Joint | 28.4 |
| TD-2 | 0.19 | Brace-Joint | 31.05 |
| TD-3 | 1.44 | Sct3 | 41.36 |
| TD-4 | 1.23 | Sct3 | 40.11 |
| TD-5 | 0.55 | Sct3 | 37.18 |
| TD-6 | 0.38 | Brace-Joint | 34.67 |
| TD-7 | 0.32 | Brace-Joint | 35.24 |

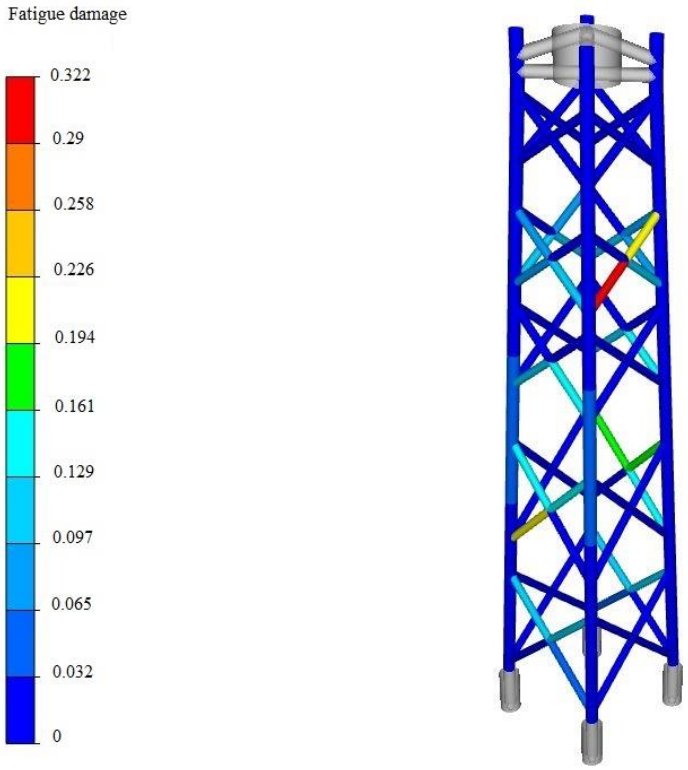



**Figure 5-14: Contour of fatigue damages of the TD-7 model**

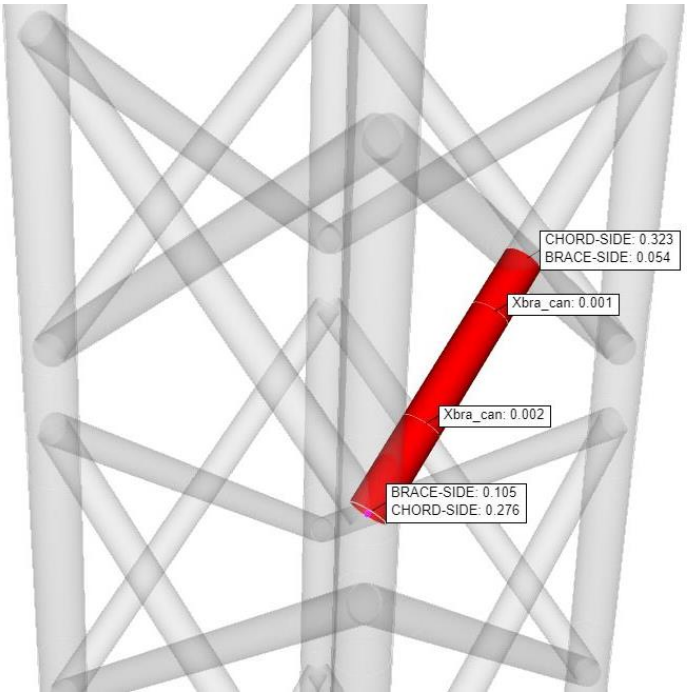



**Figure 5-15: Fatigue damage of the most critically damaged brace**

## 5.4 Conclusions

This chapter presents a comprehensive computational approach integrating topology optimisation and fatigue assessment to improve the OWT jacket foundation design. The goal is to determine the ideal load path that minimizes compliance under defined displacement constraints and loads. The time series of environmental loads is calculated in Bladed based on the 50-year return period. The same approach has been used in the published literature. Moreover, the jacket was optimised using extreme loads based on a 50-year return period but the optimised structure was not simulated under Ultimate Limit State (ULS) conditions. The optimisation in ANSYS produces a lighter 5-tier X-braced design with the optimal topology. This new geometry is recreated in Sesam, and its dynamic response is verified to avoid resonance.

Moreover, parametric models are generated by varying member thickness and diameter to assess fatigue life. The research finds that the fatigue life can be extended by strengthening joint cans and stubs while decreasing member thickness and diameter. This study pioneers OWT jacket design optimisation through detailed dynamic modelling and structural integrity evaluation. It establishes workflows integrating industry tools for optimisation and fatigue calculations. Moreover, the research quantifies the conservatism in the non-optimised baseline jacket foundation for a particular loading condition, and showcases cost reduction potential relative to the baseline model.

# 6 Concluding remarks

The cost of offshore wind energy is significantly higher than the other forms of renewable energy. The foundations of OWTs are responsible for around 30% of the capital cost of offshore energy projects. The initial projects used monopile foundations in shallow waters, but moving to deeper waters to access higher wind resources required jacket and floating foundations that can work in depths greater than 40 m. The offshore wind industry follows design standards from the oil and gas sector, but they generate overly conservative designs. Optimising these designs is essential to reduce the cost of offshore wind energy.

Existing research often simplifies the dynamic time-series fatigue analysis due to its computational demands, compromising accuracy. Moreover, the dynamic coupling between the RNA, tower, and foundation is frequently overlooked or oversimplified. Furthermore, fatigue calculations are frequently conducted in the frequency domain, disregarding the higher accuracy of the time domain approach. The ongoing efforts to enhance jacket design through optimisation algorithms show promise. However, the use of optimisation algorithms in research lacks integration with FEA, neglecting the complex dynamics of component interactions. Consequently, the potential of applying TO in offshore jacket foundation design remains largely unexplored, presenting untapped opportunities for future research.

This research is the first to propose a framework that integrates TO with fatigue life analysis and provides computed results for the fatigue life of the innovative design. The published research on TO through FEA is quite recent and suggests that future studies may focus on fatigue life calculations in this context. As a pioneer in this domain, this research significantly advances offshore wind turbine technology, providing novel insights for optimising jacket foundations and potentially contributing to the reduced cost of the offshore wind industry.

The first part showed the method to estimate the long-term environmental loads used to compute the fatigue life of offshore wind foundations. The second part

developed a detailed finite element model of the OC4 jacket foundation in 50 m water depth. The model is verified through modal analysis by comparing natural frequencies. Static deflection is also matched with published data. The model is converted into a super-element containing mass, stiffness, and gravity data. This super-element model is integrated with the NREL 5MW wind turbine in Bladed software to simulate aero-hydro-servo-elastic loads. The time-series loads are exported back to Sesam for fatigue calculations using the hot-spot stress method and Miner's rule. Moreover, the study finds the factors that impact the structure's dynamic response and fatigue life of the baseline model. The final part presents a complete framework for jacket optimisation using coupled aero-hydro-servo-elastic simulations. A continuum model with legs from the original OC4 model was built in ANSYS, and TO analysis was performed. The goal of the TO is to obtain an ideal flow path for the structure without much information about the dimensions. The outcome of the TO process, subject to the defined constraints and loads, resulted in a five x-brace jacket structure. The model was rebuilt in the Sesam and exported again to Bladed for the load calculation using the method discussed in the second part. Furthermore, various models were developed to investigate the influence of the thickness and diameter of the members and cans/stubs on the fatigue life of the jacket. Eventually, the Sesam Wind Manager estimated the fatigue damage on the members and joints based on the defined S-N curves.

The marine growth had minimal influence on the jacket's dynamics and fatigue damage. However, incorporating nonlinear soil behaviour has substantially impacted the dynamic response. The nonlinear soil model caused higher damage than the original fixed-base model, attributed to increased vibration amplitudes due to lower soil stiffness. The effect of nonlinearity was further extended to include the scour of different sizes (0.5 m, 1 m, and 2 m). Though scour depth did not alter the first two natural frequencies, it reduced the third and fourth frequencies by 0.7-3.2%—the reduction in the support due to scour caused the damage to increase. The study also evaluated the modifications to the transition piece (TP) and grouted connection designs. Varying the TP mass revealed higher mass inversely affected higher-order frequencies. However, the first two

frequencies were not altered. Moreover, the fatigue damage was greater for the heavier TP because of the higher axial force and moments on the joints, which resulted in higher stresses. The material selection between the concrete TP and steel TP showed the need to move to the lighter steel frames to extend the fatigue life. Increasing the length of the grouted connection from 4m to 6m resulted in improved support and reduced damage. However, adopting an inclined pile-in-leg connection led to lower first natural frequencies near the problematic 1P rotor frequency, significantly increasing fatigue damage.

The final part of the research reveals that the TO successfully produced a distinct truss-like structure. The optimised structure enables optimum load distribution and increases structural integrity overall. Furthermore, when evaluating the dynamic behaviour of the models, the first two eigenfrequencies were found to fall within a safe range of 0.22-0.35 Hz. In addition, it was noted that the higher-order natural frequencies of the models were also higher than the recommended threshold of 0.605 Hz. These frequencies falling inside the defined safe range indicate that the models have a good amount of stiffness and don't experience resonance.

It is worth noting that the baseline model may not have been optimised for the fatigue life. The baseline model was used because of the availability of the data and the presence of comparative studies in the literature. The mass reduction and fatigue damages result in the research are relative to the baseline model only and refer to certain environmental conditions. The fatigue calculations of the reconstructed optimised structure suggested that the design of the baseline model is quite conservative. Additionally, reducing the members' thickness and diameter could result in a substantial mass reduction of up to 35% compared to the original structure while maintaining a significant fatigue life. It was observed that the failure in the TD-3 and TD-4 models occurred at the members instead of the joints. This finding suggested that the failure of the structure would occur sooner than the desired operational lifespan of 20 years if additional reductions in member mass were attempted. The TD-5 model was built with the increased diameter and thickness; although the failure was still at the member, the fatigue

life had almost doubled. Moreover, for similar fatigue damage, it is possible to achieve the additional mass reduction by decreasing the diameter and thickness of the members while simultaneously strengthening the joints, as opposed to when only the thickness of the members was varied.

A significant mass reduction could be achieved using the TO approach, and the mass reduction is greater when the redundant diameter is also reduced along with the thickness of the members. To achieve this reduction, accurate modelling of joints plays a vital role, and it is essential to reinforce the joints with cans and stubs. This research successfully achieved a reduction in mass of approximately 35% while simultaneously reducing fatigue damages by 37.2% compared to the original OC4 jacket foundation.

The main contributions of this research are summarised below:

- It establishes an integrated framework for integrating industry-standard tools like Sesam, ANSYS, and Bladed to optimise OWT jacket design and evaluate fatigue life.
- It performs comprehensive fatigue life calculations on the topology-optimised designs using time-domain stress analysis for the first time.
- The research quantifies the conservatism in existing offshore wind turbine jacket designs through rigorous dynamic and structural analyses.
- Unlike previous simplified analytical models, it implements detailed aero-hydro-servo-elastic load simulations with a precise control system using Bladed to capture complex dynamics for TO application.
- The research includes a detailed iterative joint design for a topology-optimised structure for the first time.
- It demonstrates the significant potential to reduce the mass and costs of OWT jackets while enhancing their structural performance and fatigue life. However, the results in this study are relative to the baseline model only.
- It provides practical recommendations for jacket design aspects like soil modelling, transition piece configurations, grouted connections, etc., based on their impact on fatigue life.

- The comprehensive approach suggested by the research can help address the design challenges of cost-effective offshore jackets and tripod foundations in the industry.

The main limitations of this research are as follows:

- The use of TO has a major disadvantage in terms of computational cost, and when combined with time-domain fatigue calculations, the computational cost was relatively high.
- Simulation time during this research was 200 seconds due to the higher number of design cases. Sesam recommends using 600 seconds of simulation time. Moreover, the study does not consider the turbulence effect in Bladed for the generation of aerodynamic time series loads.
- The final TO output can vary significantly if the constraints are changed or are modelled incorrectly, hence requiring the expertise of the designers.
- The research is only focused on the jacket foundation. Not covering other types of foundations limits the application of this research.
- The TO only gives the optimum load path, and the information about the exact dimension of the structural member is not included.
- The fatigue life estimations only consider the probability of crack initiation. The crack propagation until failure is not modelled using fracture mechanics principles.
- The cost savings from the optimised designs are not quantified. Economic analyses need to be performed to estimate benefits and payback periods.

The recommendations for future work are as follows:

- Expand the topology optimisation approach to include the transition piece and optimise the full load path.
- TO design only provides the ideal load path for the jacket. Future work can include size and shape optimisation algorithms to better quantify the parametric models.
- Future work can expand to compare the topology optimisation results with other optimisation algorithms like genetic and particle swarm algorithms.

- Future work may involve analysing crack propagation and residual fatigue life using fracture mechanics to determine the actual failure of the jacket.
- The current research utilises a reduced form of a scatter diagram of environmental data due to the iterative nature of the study. Future research can enhance the analysis by incorporating the scatter diagram's full form, allowing for more data points to be included.
- Incorporate cost models to estimate potential cost savings for the optimised jacket designs.
- Assess the viability of the proposed approach for optimising other offshore structures, such as floating offshore wind foundations and oil/gas platforms.

# REFERENCES


[1] A. Zervos, “Pure Power, A report by the European Wind Energy Association’.,” 2011.

[2] W. Musial and B. Ram, “Large-Scale Offshore Wind Power in the United States: Assessment of Opportunities and Barriers,” Golden, CO (United States), Sep. 2010. doi: 10.2172/990101.

[3] B. Yeter, Y. Garbatov, and C. G. Soares, “Fatigue damage assessment of fixed offshore wind turbine tripod support structures,” *Eng Struct*, vol. 101, pp. 518–528, 2015, doi: 10.1016/j.engstruct.2015.07.038.

[4] Subhamoy Bhattacharya, *Design of Foundations for OffshoreWind Turbines*, vol. 79, no. 15. 2019.

[5] J. A. Schneider and M. Senders, “Foundation design: A comparison of oil and gas platforms with offshore wind turbines,” *Mar Technol Soc J*, vol. 44, no. 1, pp. 32–51, 2010, doi: 10.4031/MTSJ.44.1.5.

[6] NREL, “Overview of Floating Offshore Wind.” [Online]. Available: https://www.nrel.gov/news/video/overview-of-floating-offshore-wind-text.html

[7] National Renewable Energy Laboratory, “Large-scale offshore wind power in the United States: Assessment of opportunities and barriers,” 2010.

[8] World Forum Offshore Wind, “Global Offshore Wind Report,” 2023.

[9] GWEC, “Global Offshore Wind Report 2022,” 2022.

[10] WindEurope, “Wind energy in Europe,” 2023.

[11] A. Nghiem and I. Pineda, “Wind energy in Europe: Scenarios for 2030,” 2018.

[12] Z. Da, Z. Xiliang, H. Jiankun, and C. Qimin, “Offshore wind energy development in China: Current status and future perspective,” *Renewable*

*and Sustainable Energy Reviews*, vol. 15, no. 9, pp. 4673–4684, Dec. 2011, doi: 10.1016/J.RSER.2011.07.084.

[13] GWEC, “Global Offshore Wind Report 2020,” 2020.

[14] US Department of Energy, “Offshore Wind Market Report: 2021 Edition,” 2021.

[15] IRENA, “Future of wind: Deployment, investment, technology, grid integration and socio-economic aspects,” 2019.

[16] The Crown Estate, “Offshore wind report,” 2022.

[17] US Department of Energy, “Offshore wind market report,” 2022.

[18] US Department of Energy, “A Driving FORCE for Projecting Offshore Wind Energy Costs,” 2023.

[19] “Offshore Turbine Database 2016.” [Online]. Available: https://www.4coffshore.com/windfarms/turbines.aspx

[20] Fraunhofer Institute for Solar Energy Systems ISE, “Levelized Cost of Energy Renewable Energy Technologies,” 2018.

[21] P. Erik Morthorst, “THE ECONOMICS OF WIND POWER,” Copenhagen, 2009.

[22] WindEurope, “The European offshore wind industry: Key trends and statistics,” Brussels, 2016.

[23] R. Damiani, K. Dykes, and G. Scott, “A comparison study of offshore wind support structures with monopiles and jackets for U.S. waters,” *J Phys Conf Ser*, vol. 753, no. 9, 2016, doi: 10.1088/1742-6596/753/9/092003.

[24] V. Igwemezie, A. Mehmanparast, and A. Kolios, “Current trend in offshore wind energy sector and material requirements for fatigue resistance improvement in large wind turbine support structures – A review,” *Renewable and Sustainable Energy Reviews*, vol. 101, pp. 181–196, Mar. 2019, doi: 10.1016/J.RSER.2018.11.002.

[25] W. E. de Vries, D. Matha, and B. Freiwald, “Support Structure Concepts for Deep Water Sites,” 2011.

[26] S. Rae, K. T. Raaberg, and J. Das, “Offshore Wind Foundations: A European Overview,” 2017.

[27] DNV GL, “DNVGL-RP-C301-Design, fabrication, operation and qualification of bonded repair of steel structures,” 2015.

[28] A. Mathern, C. von der Haar, and S. Marx, “Concrete support structures for offshore wind turbines: Current status, challenges, and future trends,” *Energies (Basel)*, vol. 14, no. 7, 2021, doi: 10.3390/en14071995.

[29] M. D. Esteban, J. S. López-Gutiérrez, and V. Negro, “Gravity-based foundations in the offshore wind sector,” *J Mar Sci Eng*, vol. 7, no. 3, 2019, doi: 10.3390/jmse7030064.

[30] D. Roddier, C. Cermelli, A. Aubault, and A. Weinstein, “WindFloat: A floating foundation for offshore wind turbines,” *Journal of Renewable and Sustainable Energy*, vol. 2, no. 3, May 2010, doi: 10.1063/1.3435339/284734.

[31] DNV, “DNV-OS-J101 Design of offshore wind turbine structures,” 2014.

[32] IEC, “IEC 61400-3-1-Design requirements for fixed offshore wind turbines,” 2019.

[33] DNV, “DNV-RP-C205-Environmental conditions and environmental loads,” 2019.

[34] A. A. Shittu, A. Mehmanparast, L. Wang, K. Salonitis, and A. Kolios, “Comparative Study of Structural Reliability Assessment Methods for Offshore Wind Turbine Jacket Support Structures,” *Applied Sciences*, vol. 10, no. 3, p. 860, Jan. 2020, doi: 10.3390/app10030860.

[35] A. S. Ahmed, “Wind resource assessment and economics of electric generation at four locations in Sinai Peninsula, Egypt,” *J Clean Prod*, vol. 183, pp. 1170–1183, May 2018, doi: 10.1016/j.jclepro.2018.02.182.

[36] K. S. Khan and M. Tariq, “Wind resource assessment using SODAR and meteorological mast – A case study of Pakistan,” *Renewable and Sustainable Energy Reviews*, 2017, doi: 10.1016/j.rser.2017.06.050.

[37] D. A. Smith *et al.*, “Wind lidar evaluation at the Danish wind test site in Høvsøre,” *Wind Energy*, vol. 9, no. 1–2, pp. 87–93, Jan. 2006, doi: 10.1002/we.193.

[38] M. D. Mifsud, T. Sant, and R. N. Farrugia, “A comparison of Measure-Correlate-Predict Methodologies using LiDAR as a candidate site measurement device for the Mediterranean Island of Malta,” *Renew Energy*, vol. 127, pp. 947–959, Nov. 2018, doi: 10.1016/j.renene.2018.05.023.

[39] F. Fazelpour, E. Markarian, and N. Soltani, “Wind energy potential and economic assessment of four locations in Sistan and Balouchestan province in Iran,” *Renew Energy*, vol. 109, pp. 646–667, Aug. 2017, doi: 10.1016/j.renene.2017.03.072.

[40] R. Rezaei, “Fatigue Sensitivity of Monopile-supported Offshore Wind Turbines,” pp. 1–173, 2017.

[41] M. H. Patel, *Dynamics of offshore structures*, vol. 7, no. 3. 1985. doi: 10.1016/0141-0296(85)90054-9.

[42] ISO, “ISO 19902:2020 - Petroleum and natural gas industries — Fixed steel offshore structures,” 2020.

[43] B. Le Méhauté, *An Introduction to Hydrodynamics and Water Waves*. 1969. doi: https://doi.org/10.1007/978-3-642-85567-2.

[44] M. A. Hanif, F. Nadeem, R. Tariq, and U. Rashid, “Power generation by ocean energy,” *Renewable and Alternative Energy Resources*, pp. 359–430, Jan. 2022, doi: 10.1016/B978-0-12-818150-8.00002-2.

[45] J. Falnes, “A review of wave-energy extraction,” *Marine Structures*, vol. 20, no. 4, pp. 185–201, Oct. 2007, doi: 10.1016/J.MARSTRUC.2007.09.001.

[46] J. Van Der Tempel, *Design of Support Structures for Offshore Wind Turbines*, no. april. 2006.

[47] “UK Offshore Operators Association (UKOOA).” [Online]. Available: https://oeuk.org.uk/

[48] R. P. Patel, G. Nagababu, S. V. Arun Kumar, and S. Singh Kachhwaha, “Wave resource assessment and wave energy exploitation along the Indian coast,” 2020, doi: 10.1016/j.oceaneng.2020.107834.

[49] T. Liu, J. Yu, Y. Yu, X. Zhang, B. Zhou, and L. Yin, “Characterization of Wave Power Resources off the Coast of Guangdong,” *Processes 2023, Vol. 11, Page 2221*, vol. 11, no. 7, p. 2221, Jul. 2023, doi: 10.3390/PR11072221.

[50] E. Gonzalez, L. Valldecabres, H. Seyr, and J. J. Melero, “On the effects of environmental conditions on wind turbine performance: An offshore case study,” *J Phys Conf Ser*, vol. 1356, no. 1, Oct. 2019, doi: 10.1088/1742-6596/1356/1/012043.

[51] T. Gentils, L. Wang, and A. Kolios, “Integrated structural optimisation of offshore wind turbine support structures based on finite element analysis and genetic algorithm,” *Appl Energy*, vol. 199, no. August, pp. 187–204, 2017, doi: 10.1016/j.apenergy.2017.05.009.

[52] IEC, “IEC 61400-1-Wind energy generation systems - Part 1: Design requirements,” 2019.

[53] IEC, “IEC 61400-12-1 Wind turbines – Part 12-1: Power performance measurements of electricity producing wind turbines,” 2017. [Online]. Available: https://webstore.iec.ch/publication/26603

[54] DNV GL, “DNV-ST-0126-Support structures for wind turbines,” 2021.

[55] DNVGL, “DNV-RP-C203-Fatigue design of offshore steel structures,” 2019.

[56] API, “Geotechnical and Foundation Design Considerations,” 2014.

[57] E. C. F. Standardization, “EN 1993-1-3: Eurocode 3: Design of steel structures,” 1993.

[58] BSI, “BS EN 61400-3 - Wind turbines. Design requirements for offshore wind turbines,” 2019.

[59] L. Arany, S. Bhattacharya, J. Macdonald, and S. J. Hogan, “Design of monopiles for offshore wind turbines in 10 steps,” *Soil Dynamics and Earthquake Engineering*, vol. 92, pp. 126–152, 2017, doi: 10.1016/j.soildyn.2016.09.024.

[60] Christina Koukoura, “Validated Loads Prediction Models for Offshore Wind Turbines for Enhanced Component Reliability DTU Wind Energy PhD Thesis,” 2014.

[61] H. O. F. Ralph I. Stephens, Ali Fatemi, Robert R. Stephens, *Metal Fatigue in Engineering*, 2nd ed. Wiley, 2000. [Online]. Available: https://www.wiley.com/en-gb/Metal+Fatigue+in+Engineering%2C+2nd+Edition-p-9780471510598

[62] E. L. Minguez and F. Brennan, “FATIGUE & FRACTURE MECHANICS OF OFFSHORE WIND TURBINE SUPPORT STRUCTURES. PhD-Thesis,” Cranfield University, 2015.

[63] S. Aasen, A. Page, K. Skjolden Skau, and T. A. Nygaard, “Effect of the Foundation Modelling on the Fatigue Lifetime of a Monopile-based Offshore Wind Turbine,” *Wind Energy Science Discussions*, no. 2007, pp. 1–27, 2016, doi: 10.5194/wes-2016-37.

[64] Steffen Aasen, “Soil-structure interaction modelling for an offshore wind turbine with monopile foundation,” 2016.

[65] B. Byrne, R. Mcadam, B. Harvey, and G. Houlsby, “PISA: New design methods for offshore wind turbine monopiles,” in *Proceedings of the 8th International Conference OFFSHORE SITE INVESTIGATION AND GEOTECHNICS*, 2017.

[66] A. A. Shittu, A. Mehmanparast, M. Shafiee, A. Kolios, P. Hart, and K. Pilario, “Structural reliability assessment of offshore wind turbine support structures subjected to pitting corrosion-fatigue: A damage tolerance modelling approach,” *Wind Energy*, no. December 2019, pp. 1–23, 2020, doi: 10.1002/we.2542.

[67] R. Saadian and A. Taheri, “Fatigue damage analysis of an existing fixed offshore platform using spectral method for life extension,” *Journal of Marine Science and Technology (Japan)*, vol. 23, no. 4, pp. 877–887, 2018, doi: 10.1007/s00773-017-0517-z.

[68] Y. W. Wu, “TIME DOMAIN FATIGUE LIFE ANALYSIS OF OFFSHORE JACKET STRUCTURE,” 2019. Accessed: Mar. 08, 2021. [Online]. Available: http://asmedigitalcollection.asme.org/OMAE/proceedings-pdf/IOWTC2019/59353/V001T01A043/6464358/v001t01a043-iowtc2019-7591.pdf

[69] M. Kovarbašić, F. Vorpahl, and P. Schaumann, “Influence of structural redundancy on fatigue life of offshore wind turbine jacket structures,” *Proceedings of the International Offshore and Polar Engineering Conference*, pp. 274–281, 2017.

[70] T. T. Tran, E. Kim, and D. Lee, “Development of a 3-legged jacket substructure for installation in the southwest offshore wind farm in South Korea,” *Ocean Engineering*, vol. 246, p. 110643, Feb. 2022, doi: 10.1016/J.OCEANENG.2022.110643.

[71] W. Shi, J. Han, C. Kim, D. Lee, H. Shin, and H. Park, “Feasibility study of offshore wind turbine substructures for southwest offshore wind farm project in Korea,” *Renew Energy*, vol. 74, pp. 406–413, Feb. 2015, doi: 10.1016/J.RENENE.2014.08.039.

[72] T. L. Anderson, *Fracture mechanics - Fundamentals and Applications*, 3rd ed. CRC Press, Taylor & Francis Group, Boca Raton, 2005.

[73] H. A. Richard and M. Sander, *Fatigue Crack Growth: Detect—Assess—Avoid*, vol. 227. 2016.

[74] DNV, “Support structures for wind turbines,” no. July, 2018.

[75] S. Aasen, A. M. Page, K. Skjolden Skau, and T. Anders Nygaard, “Effect of foundation modelling on the fatigue lifetime of a monopile-based offshore wind turbine,” *Wind Energy Science*, vol. 2, no. 2, pp. 361–376, 2017, doi: 10.5194/wes-2-361-2017.

[76] Y. Kim and S. Jeong, “Analysis of soil resistance on laterally loaded piles based on 3D soil-pile interaction,” *Comput Geotech*, vol. 38, no. 2, pp. 248–257, 2011, doi: 10.1016/j.compgeo.2010.12.001.

[77] J. Velarde and E. E. Bachynski, “Design and fatigue analysis of monopile foundations to support the DTU 10 MW offshore wind turbine,” in *Energy Procedia*, Elsevier Ltd, 2017, pp. 3–13. doi: 10.1016/j.egypro.2017.10.330.

[78] O. M. Querin, G. P. Steven, and Y. M. Xie, “Evolutionary structural optimisation (ESO) using a bidirectional algorithm,” *Engineering Computations (Swansea, Wales)*, vol. 15, no. 8, pp. 1031–1048, 1998, doi: 10.1108/02644409810244129/FULL/XML.

[79] M. Zhou and G. I. N. Rozvany, “On the validity of ESO type methods in topology optimization,” *Structural and Multidisciplinary Optimization*, vol. 21, no. 1, pp. 80–83, Mar. 2001, doi: 10.1007/S001580050170/METRICS.

[80] G. I. N. Rozvany, “Stress ratio and compliance based methods in topology optimization - A critical review,” *Structural and Multidisciplinary Optimization*, vol. 21, no. 2, pp. 109–119, Apr. 2001, doi: 10.1007/S001580050175/METRICS.

[81] G. I. N. Rozvany, “A critical review of established methods of structural topology optimization,” *Structural and Multidisciplinary Optimization*, vol. 37, no. 3, pp. 217–237, Jan. 2009, doi: 10.1007/S00158-007-0217-0/METRICS.

[82] A. Kaveh and S. Sabeti, “Optimal Design of Jacket Supporting Structures for Offshore Wind Turbines Using Enhanced Colliding Bodies Optimization Optimal Design of Jacket Supporting Structures for Offshore Wind Turbines Using Enhanced,” *Periodica Polytechnica Civil Engineering*, 2017.

[83] J. Häfele and R. Rolfes, “Approaching the ideal design of jacket substructures for offshore wind turbines with a Particle Swarm Optimization algorithm,” in *Proceedings of the Twenty-sixth (2016) International Ocean and Polar Engineering Conference*, ISOPE, 2016. [Online]. Available: www.isope.org

[84] L. B. Pasamontes, F. G. Torres, D. Zwick, S. Schafhirt, and M. Muskulus, “Support Structure Optimization for Offshore Wind Turbines With a Genetic Algorithm-OMAE,” in *Proceedings of the ASME 2014 33rd International Conference on Ocean, Offshore and Arctic Engineering*, ASME, 2014. doi: 10.1115/OMAE2014-24252.

[85] V. Savsani, P. Dave, B. D. Raja, and V. Patel, “Topology optimization of an offshore jacket structure considering aerodynamic, hydrodynamic and structural forces,” *Eng Comput*, vol. 37, no. 4, pp. 2911–2930, 2021, doi: 10.1007/s00366-020-00983-3.

[86] A. A. Motlagh, N. Shabakhty, and A. Kaveh, “Design optimization of jacket offshore platform considering fatigue damage using Genetic Algorithm,” *Ocean Engineering*, vol. 227, no. March, p. 108869, 2021, doi: 10.1016/j.oceaneng.2021.108869.

[87] E. Y. Kling, B. Ferri, B. Bjørhovd, F. Strand, and S. M. Hope, “Automated jacket design,” *Proceedings of the International Offshore and Polar Engineering Conference*, vol. 1, pp. 1062–1068, 2019.

[88] K. Hon Chew, M. Muskulus, D. Zwick, E. Ng, and K. Tai, “Structural Optimization and Parametric Study of Offshore Wind Turbine Jacket Substructure,” in *Proceedings of the Twenty-third (2013) International Offshore and Polar Engineering Anchorage*, ISOPE, 2013.

[89] W. Deng, X. Tian, X. Han, G. Liu, Y. Xie, and Z. Li, “Topology optimization of jack-up offshore platform leg structure:,” *https://doi.org/10.1177/1475090220928736*, vol. 235, no. 1, pp. 165–175, Jun. 2020, doi: 10.1177/1475090220928736.

[90] X. Tian, Q. Wang, G. Liu, Y. Liu, Y. Xie, and W. Deng, “Topology optimization design for offshore platform jacket structure,” *Applied Ocean Research*, vol. 84, pp. 38–50, Mar. 2019, doi: 10.1016/J.APOR.2019.01.003.

[91] Y. S. Lee, J. A. González, J. H. Lee, Y. Il Kim, K. C. Park, and S. Han, “Structural topology optimization of the transition piece for an offshore wind turbine with jacket foundation,” *Renew Energy*, vol. 85, pp. 1214–1225, 2016, doi: 10.1016/j.renene.2015.07.052.

[92] X. Tian *et al.*, “Optimization design of the jacket support structure for offshore wind turbine using topology optimization method,” *Ocean Engineering*, vol. 243, p. 110084, Jan. 2022, doi: 10.1016/J.OCEANENG.2021.110084.

[93] C. Zhang, K. Long, J. Zhang, F. Lu, X. Bai, and J. Jia, “A topology optimization methodology for the offshore wind turbine jacket structure in the concept phase,” *Ocean Engineering*, vol. 266, Dec. 2022, doi: 10.1016/J.OCEANENG.2022.112974.

[94] F. Lu, K. Long, C. Zhang, J. Zhang, and T. Tao, “A novel design of the offshore wind turbine tripod structure using topology optimization methodology,” *Ocean Engineering*, vol. 280, no. April 2022, p. 114607, 2023, doi: 10.1016/j.oceaneng.2023.114607.

[95] O. YUKSEL, “AN OVERVIEW ON TOPOLOGY OPTIMIZATION METHODS EMPLOYED IN STRUCTURAL ENGINEERING,” *Kirklareli University Journal of Engineering and Science*, vol. 5, no. 2, pp. 159–175, Dec. 2019, doi: 10.34186/KLUJES.606666.

[96] B. Zhu *et al.*, “Design of compliant mechanisms using continuum topology optimization: A review,” *Mech Mach Theory*, vol. 143, p. 103622, Jan. 2020, doi: 10.1016/J.MECHMACHTHEORY.2019.103622.

[97] L. Meng *et al.*, “From Topology Optimization Design to Additive Manufacturing: Today’s Success and Tomorrow’s Roadmap,” *Archives of Computational Methods in Engineering*, vol. 27, no. 3, pp. 805–830, Jul. 2020, doi: 10.1007/S11831-019-09331-1.

[98] J. Liu and Y. Ma, “A survey of manufacturing oriented topology optimization methods,” *Advances in Engineering Software*, vol. 100, pp. 161–175, 2016, doi: 10.1016/j.advengsoft.2016.07.017.

[99] L. Meng *et al.*, “From Topology Optimization Design to Additive Manufacturing: Today’s Success and Tomorrow’s Roadmap,” *Archives of Computational Methods in Engineering*, vol. 27, no. 3, pp. 805–830, 2020, doi: 10.1007/s11831-019-09331-1.

[100] S. Satya Hanush and M. Manjaiah, “Topology optimization of aerospace part to enhance the performance by additive manufacturing process,” *Mater Today Proc*, vol. 62, no. P14, pp. 7373–7378, Jan. 2022, doi: 10.1016/J.MATPR.2022.02.074.

[101] J. H. Zhu, W. H. Zhang, and L. Xia, “Topology Optimization in Aircraft and Aerospace Structures Design,” *Archives of Computational Methods in Engineering 2015 23:4*, vol. 23, no. 4, pp. 595–622, Apr. 2015, doi: 10.1007/S11831-015-9151-2.

[102] D. Jankovics and A. Barari, “Customization of Automotive Structural Components using Additive Manufacturing and Topology Optimization,” *IFAC-PapersOnLine*, vol. 52, no. 10, pp. 212–217, Jan. 2019, doi: 10.1016/J.IFACOL.2019.10.066.

[103] D. Jankovics and A. Barari, “Customization of Automotive Structural Components using Additive Manufacturing and Topology Optimization,”

*IFAC-PapersOnLine*, vol. 52, no. 10, pp. 212–217, 2019, doi: 10.1016/j.ifacol.2019.10.066.

[104] Y. M. Xie, “Generalized topology optimization for architectural design,” *Architectural Intelligence 2022 1:1*, vol. 1, no. 1, pp. 1–11, Jun. 2022, doi: 10.1007/S44223-022-00003-Y.

[105] N. Tan and R. J. van Arkel, “Topology Optimisation for Compliant Hip Implant Design and Reduced Strain Shielding,” *Materials*, vol. 14, no. 23, Dec. 2021, doi: 10.3390/MA14237184.

[106] M. Kapsali and J. K. Kaldellis, “Offshore Wind Power Basics,” *Comprehensive Renewable Energy*, pp. 431–468, Jan. 2012, doi: 10.1016/B978-0-08-087872-0.00217-1.

[107] G. I. N. Rozvany, M. Zhou, and T. Birker, “Generalized shape optimization without homogenization,” *Structural optimization 1992 4:3*, vol. 4, no. 3, pp. 250–252, Sep. 1992, doi: 10.1007/BF01742754.

[108] M. P. Bendsøe, “Optimal shape design as a material distribution problem,” *Structural Optimization*, vol. 1, no. 4, pp. 193–202, Dec. 1989, doi: 10.1007/BF01650949/METRICS.

[109] W. J. Stroud, “Optimization of Composite Structures, a Shape and Topology Sensitivity Analysis,” *Mechanics of Composite Materials*, no. June 2014, pp. 307–321, 2014, [Online]. Available: http://linkinghub.elsevier.com/retrieve/pii/B9780080293844500262

[110] O. Sigmund and K. Maute, “Topology optimization approaches: A comparative review,” *Structural and Multidisciplinary Optimization*, vol. 48, no. 6, pp. 1031–1055, Dec. 2013, doi: 10.1007/S00158-013-0978-6/FIGURES/2.

[111] J. D. Deaton and R. V. Grandhi, “A survey of structural and multidisciplinary continuum topology optimization,” *Structural and Multidisciplinary Optimization*, vol. 49, no. 1, pp. 1–38, Jan. 2014, doi: 10.1007/S00158-013-0956-Z.

[112] J. F. Manwell, J. G. McGowan, and A. L. Rogers, *Wind energy explained : theory, design and application*. Wiley, 2009.

[113] L. Morten Bardal, L. R. Saetran, and E. Wangsness, “Performance test of a 3MW wind turbine-effects of shear and turbulence,” in *12th Deep Sea Offshore Wind R&D Conference*, 2015, pp. 83–91.

[114] M. Petersen, “Wind turbine test Vestas V27-225 kW,” 1990. [Online]. Available: http://orbit.dtu.dk/files/51244107/ris_m_2861.pdf

[115] J. F. Manwell, J. G. McGowan, and A. L. Rogers, *Wind Energy Explained*. Chichester, UK: John Wiley & Sons, Ltd, 2002. doi: 10.1002/0470846127.

[116] National Renewable Energy Laboratory, “Wind Energy Resource Atlas of the United States,” 2007. [Online]. Available: https://www.nrc.gov/docs/ML0720/ML072040340.pdf

[117] UL, “Windographer: Wind Data Analytics and Visualization Solution.” New York. [Online]. Available: https://www.windographer.com/

[118] I. S. Øistad, “Site analysis of the Titran Met-masts,” Norwegian University of Science and Technology, 2014.

[119] NIST, “e-Handbook of Statistical Methods.” [Online]. Available: http://www.itl.nist.gov/div898/handbook/.

[120] M. M. Mukaka, “Statistics corner: A guide to appropriate use of correlation coefficient in medical research.,” *Malawi medical journal* , vol. 24, no. 3, pp. 69–71, Sep. 2012, [Online]. Available: http://www.ncbi.nlm.nih.gov/pubmed/23638278

[121] N. Boccard, “Capacity factor of wind power realized values vs. estimates,” *Energy Policy*, vol. 37, no. 7, pp. 2679–2688, Jul. 2009, doi: 10.1016/J.ENPOL.2009.02.046.

[122] B. Breitschopf, “Electricity costs of energy-intensive industries in Norway-a comparison with energy-intensive industries in selected countries,” 2016. [Online]. Available:

https://www.energinorge.no/contentassets/525e77b1feff4203a94ef6d1f94cfd03/electricity-costs-of-energy-intensive-industries-in-norway.pdf

[123] IEA, “Norway - IEA Wind TCP.” Accessed: Jun. 06, 2019. [Online]. Available: https://community.ieawind.org/about/member-activities/norway

[124] Palaside, “@Risk.” New York. [Online]. Available: http://www.palisade.com/

[125] I. – International Renewable Energy Agency, “FUTURE OF WIND Deployment, investment, technology, grid integration and socio-economic aspects A Global Energy Transformation paper Citation About IRENA,” 2019, Accessed: Apr. 27, 2022. [Online]. Available: www.irena.org/publications.

[126] A. Glisic, N. Do Nguyen, and P. Schaumann, “Comparison of integrated and sequential design approaches for fatigue analysis of a jacket offshore wind turbine structure,” *Proceedings of the International Offshore and Polar Engineering Conference*, vol. 2018-June, pp. 440–447, 2018.

[127] A. Glisic, N.-D. Nguyen, and P. Schaumann, “FATIGUE ANALYSIS ON INNOVATIVE 10 MW OFFSHORE JACKET STRUCTURE USING INTEGRATED DESIGN APPROACH,” in *THE INTERNATIONAL CONFERENCE ON WIND ENERGY HARVESTING*, 2018, p. 269.

[128] B. S. T. Fischer, W. de Vries, “Upwind Design Basis,” *North*, 2010.

[129] J. Jonkman, S. Butterfield, W. Musial, and G. Scott, “Definition of a 5-MW Reference Wind Turbine for Offshore System Development,” Golden, CO (United States), 2009. [Online]. Available: http://www.osti.gov/bridge

[130] J. Jonkman and W. Musial, “Offshore Code Comparison Collaboration (OC3) for IEA Task 23 Offshore Wind Technology and Deployment,” 2010.

[131] F. Vorphal and D. Kaufer, “Technical Report Description of a basic model of the ` UpWind reference jacket ’ for code comparison in the OC4 project under IEA Wind Annex 30,” Bremerhaven, Germany, 2013.

[132] Z. Wang, C. Xiang, H. Liu, and M. Liu, “Accuracy and Efficiency Analysis of the Beam Elements for Nonlinear Large Deformation,” *Journal of Vibration Engineering and Technologies*, vol. 11, no. 1, pp. 319–328, 2023, doi: 10.1007/s42417-022-00581-1.

[133] K. A. Abhinav and N. Saha, “Stochastic response of jacket supported offshore wind turbines for varying soil parameters,” *Renew Energy*, vol. 101, pp. 550–564, 2017, doi: 10.1016/j.renene.2016.09.019.

[134] E. M. de Mendonca, G. B. Ellwanger, and J. R. M. de Sousa, “A COMPARATIVE STUDY OF JACKET FOUNDATIONS FOR OFFSHORE WIND TURBINES”.

[135] R. R. Damiani, A. N. Robertson, and J. M. Jonkman, “Assessing the Importance of Nonlinearities in the Development of,” in *Proceedings of the International Conference on Offshore Mechanics and Arctic Engineering American Society of Mechanical Engineers*, Nantes, France, 2013, pp. 1–16.

[136] W. Shi *et al.*, “Soil-Structure Interaction on the Response of Jacket-Type Offshore Wind Turbine,” *INTERNATIONAL JOURNAL OF PRECISION ENGINEERING AND MANUFACTURING-GREEN TECHNOLOGY*, vol. 2, no. 2, p. 139, 2015, doi: 10.1007/s40684-015-0018-7.

[137] P. Passon, “Damage equivalent wind-wave correlations on basis of damage contour lines for the fatigue design of offshore wind turbines,” *Renew Energy*, vol. 81, pp. 723–736, Sep. 2015, doi: 10.1016/J.RENENE.2015.03.070.

[138] DNV GL, “White paper on ‘FIXED OFFSHORE WIND What Sesam can do for fixed offshore wind turbine.’”

[139] IEC, “Internation standard IEC 61400-3 - Design requirements for offshore wind turbines,” 2009.

[140] A. Glisic, N. Nguyen, P. Schaumann, and L. U. Hannover, “FATIGUE ANALYSIS ON INNOVATIVE 10 MW OFFSHORE JACKET,” vol. 2015, no. March, pp. 269–276, 2018.

[141] DNV, “USING SESAM ™ AND BLADED IN ONE WORKFLOW,” 2021.

[142] DNV, “Verification report of Sesam ’ s Bladed interface_IMPLEMENTING AN INTERFACE BETWEEN BLADED AND SESAM Verification,” 2019.

[143] D. I. Manolas, V. A. Riziotis, G. P. Papadakis, and S. G. Voutsinas, “Hydro-Servo-Aero-Elastic Analysis of Floating Offshore Wind Turbines,” *Fluids 2020, Vol. 5, Page 200*, vol. 5, no. 4, p. 200, Nov. 2020, doi: 10.3390/FLUIDS5040200.

[144] DNV, “BLADED, Engineering feature summary,” 2020.

[145] Y. C. Hung, Y. Y. Chang, and S. Y. Chen, “Natural frequency and vibration analysis of jacket type foundation for offshore wind power,” *IOP Conf Ser Mater Sci Eng*, vol. 276, no. 1, 2017, doi: 10.1088/1757-899X/276/1/012035.

[146] M. Martinez-Luengo, A. Kolios, and L. Wang, “Parametric FEA modelling of offshore wind turbine support structures: Towards scaling-up and CAPEX reduction,” *International Journal of Marine Energy*, vol. 19, pp. 16–31, Sep. 2017, doi: 10.1016/j.ijome.2017.05.005.

[147] DNV, “DNV GL Analysis of grouted connections using the finite element method,” no. September, 2016, [Online]. Available: http://www.dnvgl.com

[148] L. Arany, S. Bhattacharya, J. H. G. Macdonald, and S. J. Hogan, “Closed form solution of Eigen frequency of monopile supported offshore wind turbines in deeper waters incorporating stiffness of substructure and SSI,” *Soil Dynamics and Earthquake Engineering*, vol. 83, no. February, pp. 18–32, 2016, doi: 10.1016/j.soildyn.2015.12.011.

[149] F. Miceli, “Wind farms construction.” [Online]. Available: https://www.windfarmbop.com/type-of-towers-stiff-soft-or-soft-soft/

[150] ESRA, “Topology Optimization.” [Online]. Available: https://esraenergy.com.my/topology-optimization.html

[151] L. Berrocal *et al.*, “Topology optimization and additive manufacturing for aerospace components,” *Progress in Additive Manufacturing*, vol. 4, no. 2, pp. 83–95, 2019, doi: 10.1007/s40964-018-0061-3.

[152] API, “API RP 2A - Recommended Practice for Planning, Designing, and Constructing Fixed Offshore Platforms—Working Stress Design,” 2000.

[153] F. M. B. Miranda, “Finite Element Analysis of Tubular Offshore X-Joint Under Static Loading,” 2017.

[154] Norsk Sokkels Konkuranseposisjon, “Design of Steel Structures,” 2014. doi: 10.1002/9783433604229.

# Appendix A Electricity prices and TGC prices

## A.1 Electricity prices in Norway

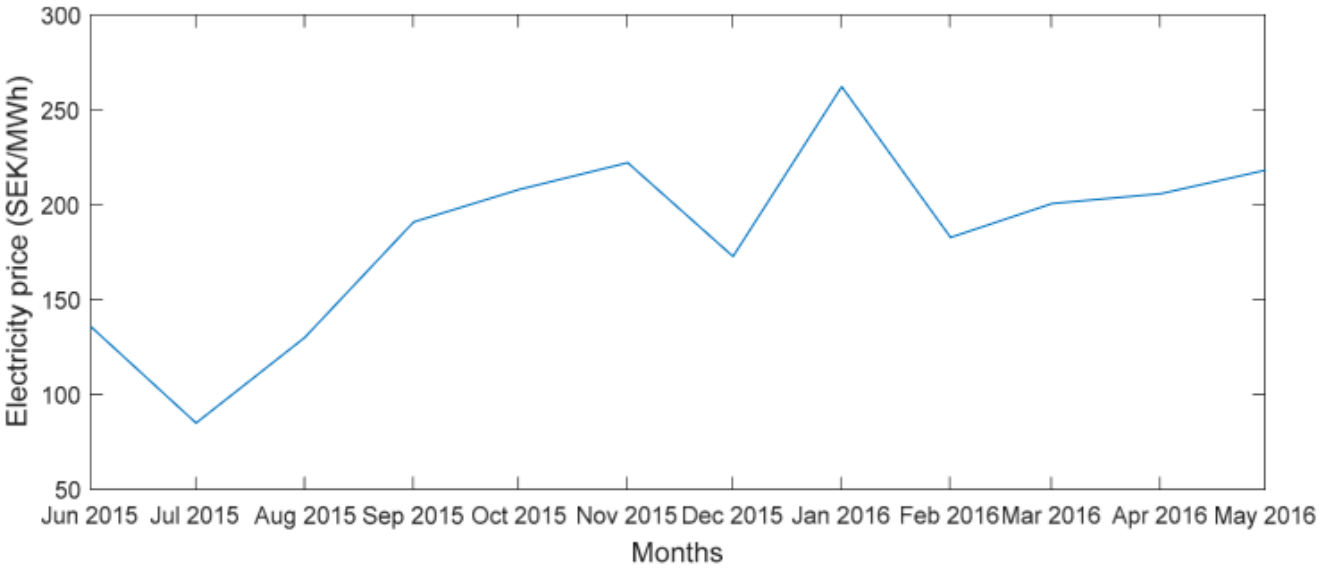



**Figure A-1: Monthly average electricity prices**

## A.2 TGC prices in Norway

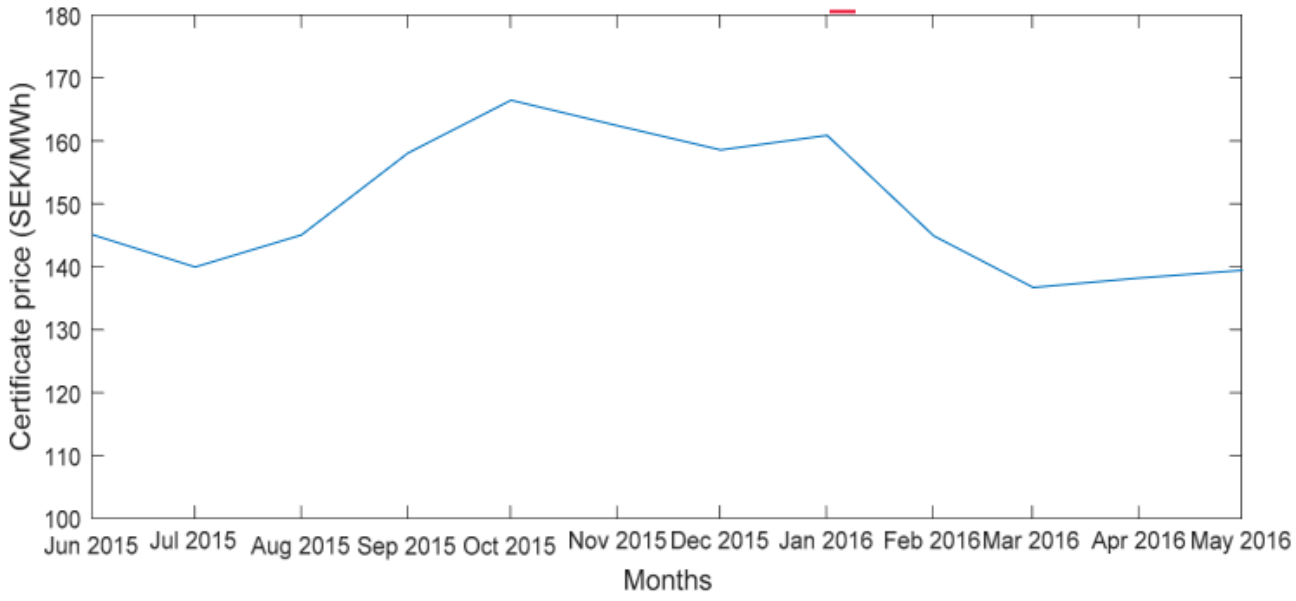



**Figure A-2: Monthly average TGC spot prices**

# Appendix B S-N curves

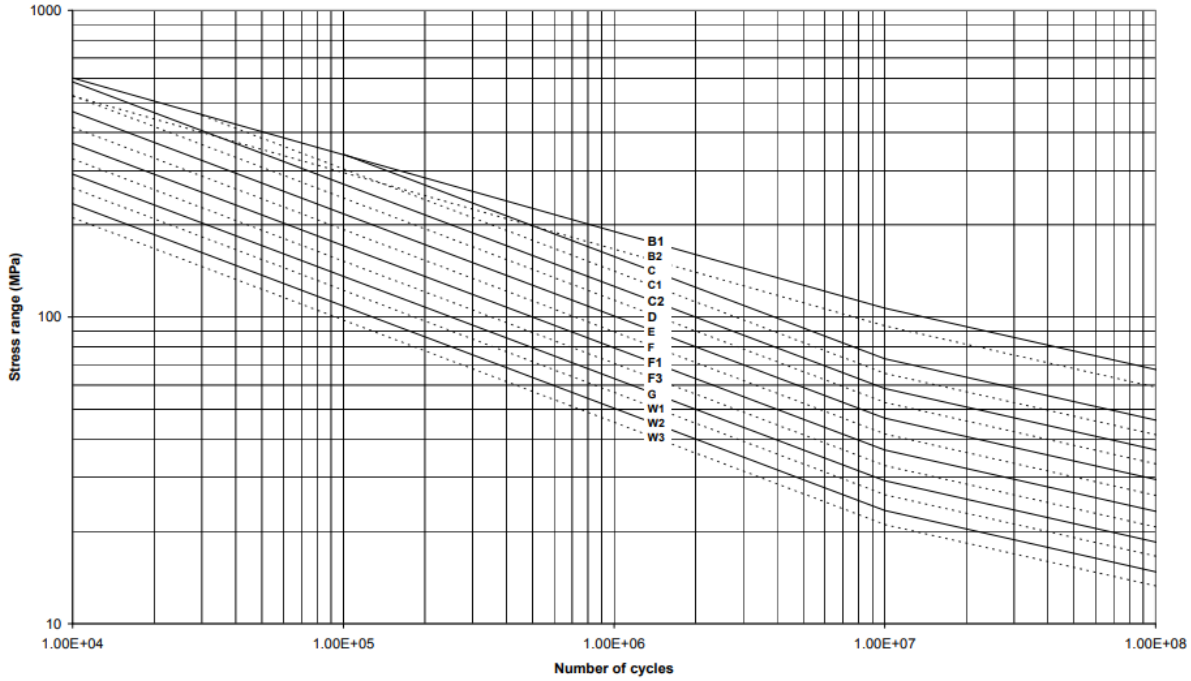



**Figure B-1: S-N curve for steel members in air**

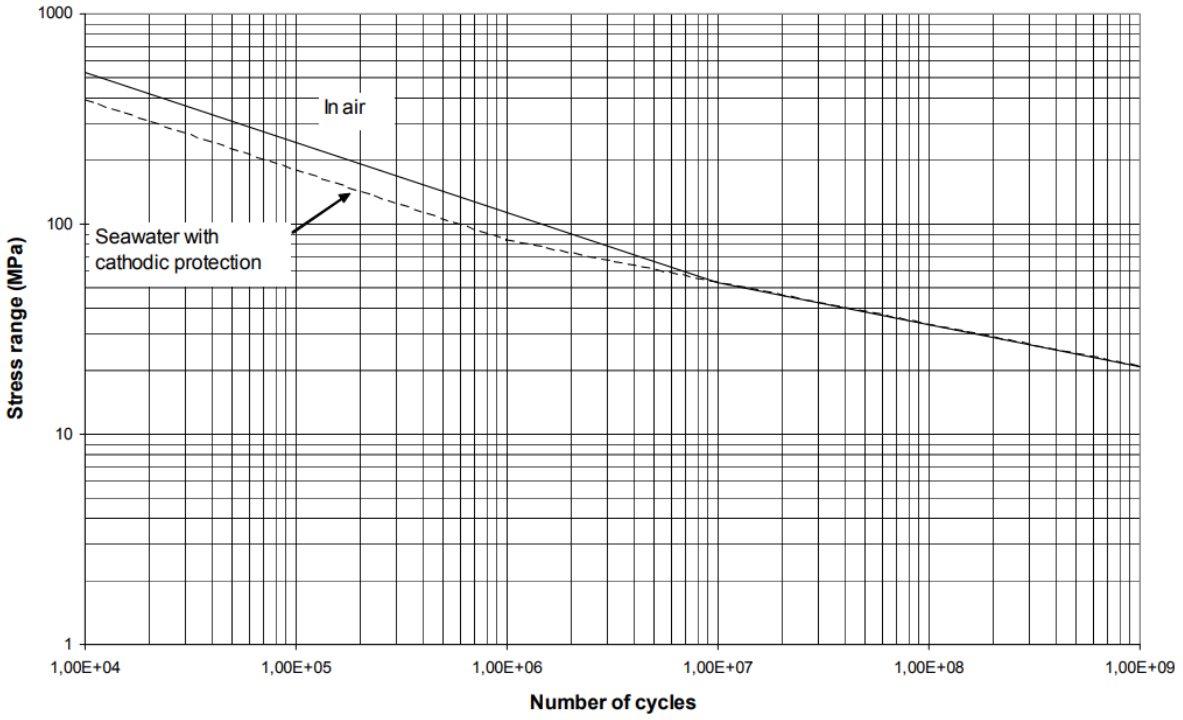



**Figure B-2: S-N curve for steel tubular joints in air and seawater with cathodic protection**

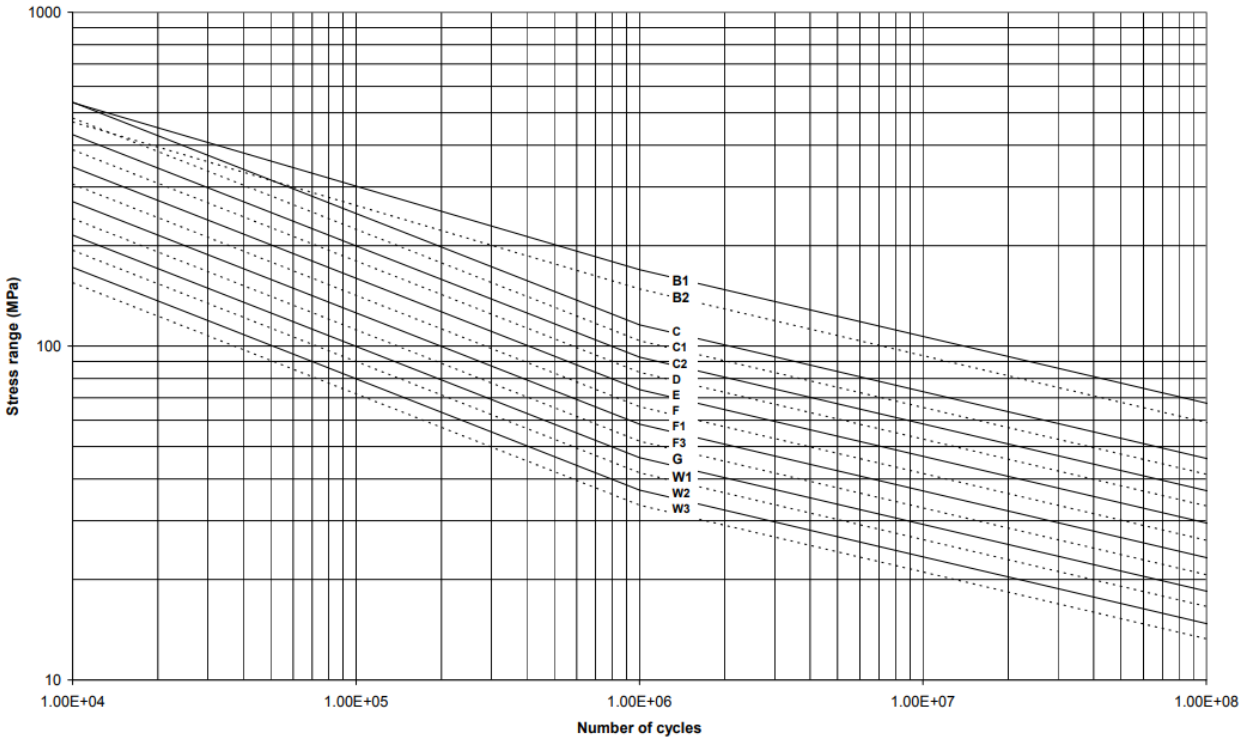



**Figure B-3: S-N curve for steel in seawater with cathodic protection** [31]